INNOVATIVE STRUCTURAL HEALTH MONITORING

USING SMART SENSORS

A Dissertation

Presented to

the Faculty of the Department of Mechanical Engineering

University of Houston

In Partial Fulfillment

of the Requirements for the Degree

Doctor of Philosophy

in

Mechanical Engineering

by

Weijie Li

May 2017

INNOVATIVE STRUCTURAL HEALTH MONITORING

USING SMART SENSORS

____

Weijie Li

Approved:

____

Chair of the Committee
Gangbing Song, Professor
Mechanical Engineering

Committee Members:

____

Matthew Franchek, Professor
Mechanical Engineering

____

Yi-Lung Mo, Professor
Civil and Environmental Engineering

____

Karolos Grigoriadis, Professor
Mechanical Engineering

____

Li Sun, Professor
Mechanical Engineering

____

Suresh K. Khator, Associate Dean
Cullen College of Engineering

____

Pradeep Sharma, Professor and Chair
Mechanical Engineering

Acknowledgements

First and foremost, I would like to express my deepest gratitude to my advisor, Professor Gangbing Song. Thank you for the valuable advice, support, and encouragement. The academic life at the University of Houston under your guidance was a tremendous asset to my career and life.

I sincerely appreciate the efforts of the committee members, Professor Matthew Franchek, Professor Yi-Lung Mo, Professor Karolos Grigoriadis, and Professor Li Sun for reading the dissertation and providing many valuable comments that improved this dissertation greatly.

I would like thank all of the colleagues from Smart Materials and Structures Lab for their unwavering friendship and moral support. In particular, Dr. Michael Ho for his valuable guidance, insightful advices, encouragement and support throughout my study; Dr. Changhang Xu for his help on how to use the AE system; Dr. Qingzhao Kong for his assistance on how to use smart aggregates; Dr. Devendra Patil for his expertise in mechanical design; Ms. Ing Lim for her assistance on using the testing machines; Mr. Jiajia Zheng, Mr. Yabin Liang, and Mr. Jiaochao Wu for their assistance in preparing the experiments.

The research reported in this dissertation has been partially supported by the China Scholarship Council (No. 201306060086). The support is gratefully appreciated.

Finally and most importantly, I am forever indebted to my family for their endless love, understanding, patience, support and encouragement.

INNOVATIVE STRUCTURAL HEALTH MONITORING

USING SMART SENSORS

An Abstract

of

A Dissertation

Presented to

the Faculty of the Department of Mechanical Engineering

University of Houston

In Partial Fulfillment

of the Requirements for the Degree

Doctor of Philosophy

in

Mechanical Engineering

by

Weijie Li

May 2017

Abstract

Civil, mechanical, and aerospace engineering structures, which serve as the foundation for modern society, undergo continuous strength deterioration due to loading and environmental impacts, and may suffer from the associated potential of damage accumulation. Structural health monitoring (SHM) is a process in which damage identification strategies are implemented for determining the presence, location, and severity of damages, and the remaining life of the structure after the occurrence of damage.

There are numerous smart sensors available targeted at various SHM applications, and among which the fiber optic sensors and piezoelectric sensors are two of the most widely adopted smart sensors. Fiber optic sensors are passive, which have the advantages of small size, remote sensing, corrosion resistance, immunity to electromagnetic interference, and excellent multiplicity. Piezoelectric sensors work on the direct and inverse effect of piezoelectricity, which can be used as both sensors and actuators. This dissertation explores five innovative designs and applications of these two types of smart sensors in the field of SHM, especially in civil engineering, with two of them are based on fiber optic sensors and the other three are based on piezoelectric sensors.

In the first study, a novel rebar corrosion detection technique for reinforced concrete structure was proposed based on active thermal probe. The active thermal probe was designed and fabricated according to the combined fiber Bragg grating and carbon

fiber. The magnitude of the temperature response of the thermal probe correlates to the corrosion severity.

In the second study, a novel type of ferromagnetic distance-based metal loss sensor was proposed based on the principle of fiber optic macro-bend loss. The practicality of the proposed distance sensor for metal loss measurement was validated through scanning the fabricated corrosion samples.

The third study presented the feasibility of using smart aggregates, which are a type of embedded piezoelectric sensors, as embedded acoustic emission sensors for the health monitoring of concrete structures. The performance of the embedded smart aggregates were compared with the traditional surface mounted acoustic emission sensors in their ability to detect and evaluate the damage to the concrete structure.

The fourth study experimentally investigated the feasibility of debonding characterization in fiber-reinforced polymer rebar reinforced concrete using acoustic emission technique. The results demonstrated a clear correlation between the damage evolution of carbon-fiber-reinforced polymer rebar pullout and the acoustic emission parameters.

The final study employed an electromechanical impedance-based structural health monitoring technique by applying piezoelectric sensors to detect the debonding damage of a carbon fiber reinforced polymer rebar reinforced concrete. Statistical damage metrics, root mean square deviation and mean absolute percentage deviation, were used to quantify the changes in impedance signatures measured by the piezoelectric sensors due to various debonding conditions.

Table of Contents

List of Figures

List of Tables

1 Introduction

1.1 Research Motivation and Objectives

Civil, mechanical, and aerospace engineering structures are the foundation of modern society and directly related to the economic achievement of a nation. However, these structures, such as buildings, bridges, pipelines, highways and other lifeline systems, deteriorate with time due to various reasons including loading, environmental impacts, and extreme events like earthquake. Additionally, many of these structures are approaching the end of their designed service life. The situation of aging infrastructure has become a great concern for human society. Therefore, it is imperative to effectively monitor and predict the health conditions of the structures at the earliest possible time so that the structures can continue to be safely operated, and further improve the public safety. Structural health monitoring (SHM) is a process in which damage identification strategies are implemented for determining the presence, location, and severity of damages and the remaining life of the structure after the occurrence of damage. SHM is a way to continuously monitor structural response and evaluate structural condition in real-time. SHM involves the integration of sensors, particularly smart materials, data acquisition and transmission, computational power, and processing capability inside the structures.

Various types of sensors can be adopted in the structural health monitoring system, among which fiber optic sensors and piezoelectric sensors are the most widely adopted sensor types due to their distinct advantages. Fiber optic sensors are passive by nature, which have the advantages of small size, remote sensing, corrosion resistance, immunity to electromagnetic interference, and excellent multiplicity. Piezoelectric sensors work on the direct and inverse effect of piezoelectricity, which can be used as both sensors and actuators. This dissertation describes five innovative designs and applications of these two types of smart sensors in structural health monitoring of civil structures. Chapter three and chapter four are associated with the innovative designs and applications of fiber optic based smart sensors, and chapter five through seven present the innovative applications of piezoelectric based smart sensors.

Corrosion of the steel reinforcement is one of major culprits for the deterioration of reinforced concrete structures. Corrosion products are usually two to six times more voluminous than that of the original steel consumed, therefore exerting expansive pressure on the surrounding concrete wall and eventually leading to concrete cover cracking, spalling and debonding. Such damages reduce span of service life of the structural component while adding up maintenance cost. The commonly used measures for corrosion detection at present are not sufficient to provide sufficient justification for making decision on structural maintenance and repair. Hence, it is very important to develop an early and reliable method for detecting steel reinforcement corrosion in concrete structure. Chapter three presents an innovative corrosion detection method for steel reinforced concrete based on the combined carbon fiber and fiber Bragg grating (FBG) active thermal probe. The proposed corrosion detection method lies in the fact that the corrosion products act as thermal barriers trapping the heat generated by the probe and the probe concurrently measures the temperature response. The characteristics of the temperature response are correlated to the corrosion severity.

Chapter four deals with a more general form of corrosion, the corrosion of metallic structures. Corrosion of metallic structures is a problem across multiple industries. For example, in the oil and gas industry, the corrosion of pipelines can lead to leakage, and thus a major loss of profit. While some nondestructive methods are available, such as ultrasound, much of the work must be done manually and can take much time. For pipeline interiors and other inaccessible areas, monitoring for corrosion regularly is even more difficult. Thus, the objective of the research described in chapter four is to develop a metal loss detection sensor by fully utilizing the advantages offered by the fiber optic sensors, such as small size and low weight, immunity to electromagnetic interference, corrosion resistance and the potential for remote operation. To this end, a novel type of ferromagnetic distance sensor was proposed based on the principle of fiber optic macro-bend loss, with the aim to measure the metal loss due to corrosion, or any other process that can cause metal loss. The proposed fiber optic macro-bend distance sensor utilizes the phenomenon of bending losses of light intensity inside optical fiber which is dependent on the radius of bending.

Chapter five begins the theme of piezoelectric based smart sensors. The acoustic emission (AE) method has emerged as a promising nondestructive evaluation technique for long-term monitoring and evaluating of damage evolution of the concrete structures. The AE signals offer rich damage-related information of the host structure, which are well-suited for damage detection and assessment of concrete structures. Conventionally, AE sensors are mounted on the surface of a structure to capture the AE signals generated from the structure. The coupling between AE sensors and the structure is achieved using a couplant such as oil or grease. However, it is difficult to maintain a stable coupling over long period so that the measurement accuracy will decrease in cases of in-situ and long-term monitoring of concrete structures. Additionally, the AE signal will dramatically attenuate as it travels through the concrete due to the high attenuation property of concrete material, which makes traditional AE technique inappropriate for health monitoring of the large-scale concrete structure. Moreover, traditional AE sensors can hardly be applied to the structures that are difficult to access, for example, the underground structures. To solve the problems encountered by traditional surface mounted AE sensor, a novel type of embedded AE sensors was developed and tested using the smart aggregate (SA) in chapter five. The smart aggregate, as a piezoceramic based embeddable transducer, is made of a thin PZT (lead zirconate titanate) patch that is protected by a concrete or marble case. The feasibility study of using the smart aggregates as embedded AE sensors for structural health monitoring of concrete structures is presented in this chapter.

Chapter six and chapter seven present the novel studies on debonding detection in fiber reinforced polymer (FRP) rebar reinforced concrete using acoustic emission technique and electro-mechanical impedance (EMI) technique, respectively. The application of FRP rebars as an alternative to the steel reinforcements has gained increasing interest over the last few years. The FRP composite reinforcing bars exhibit several advantages over their steel counterpart, such as light weight, high tensile strength, high corrosion resistance, good fatigue resistance and non-electromagnetic. The interfacial bonding between the FRP rebars and the concrete plays an important role in achieving the composite behavior and increasing the strength. The interfacial bonding will deteriorate due to environmental and load-related issues, leading to debonding between the concrete and the reinforcement. Interfacial debonding could weaken the structural integrity, reduce tensile resistance of the structure, and make the structure vulnerable to more damage. It is therefore essential to develop an appropriate SHM scheme towards the detection of interfacial bond failure between FRP rebars and concrete. In chapter six, the debonding characteristics between FRP rebar and concrete was explored using AE technique, along with finite element analysis. And in chapter seven, the debonding characteristics was characterized by electro-mechanical impedance technique. Since the damage assessment made from the impedance signatures is only qualitative, scalar damage metrics, including root mean square deviation (RMSD) and mean absolute percentage deviation (MAPD), were defined to quantify the difference in the electrical impedance signatures before and after the debonding damage.

1.2 Major Contributions

Each chapter in this dissertation has contributed to their respective engineering problem. In chapter three, the proposed combined carbon fiber/FBG active thermal probe was able to detect the presence of corrosion products of steel reinforced concrete based on the temperature response. Results suggest that there is a strong correlation between corrosion degree and temperature response. Increased degrees of corrosion lead to higher temperature on the thermal probe when a short duration of heat pulse is applied. Further work is necessary to fully understand the correlation between the corrosion degree and the temperature response measured by the thermal probe. The proposed corrosion detection method is quite efficient in measurement, which holds significant advantages for in-situ and long term inspection of a reinforced concrete structure.

The new fiber optic macro-bend based metal loss sensor in chapter four firstly contributes itself as another tool that can be used to detect and characterize the corrosion pits of metallic structures. The sensor is able to measure the rough geometry of the corrosion pit of various shapes. If more resolution is required, the performance of the sensor can be further improved. The proposed ferromagnetic distance sensor has the advantages of simple structure, low cost, non-contact and remote sensing, which will be a promising technique in detecting undesired metal loss, such as in the field of corrosion detection and assessment.

In chapter five, a new solution to the sensitivity issues of traditional AE sensors applied in concrete structures was proposed and examined. The smart aggregate, which is a piezoceramic patch sandwiched by two marble blocks, can be advantageously utilized as embedded AE sensors for concrete structures. The use of SAs as embedded AE sensors possesses several advantages. Firstly, the structure and fabrication process of SAs are simple and low cost. Secondly, the embedded SAs are capable of serving in-situ and long-term monitoring of concrete structures, without addition manual check for coupling between the sensor and the structure. Finally, the SAs can be pre-embedded into a structure, which make them more suitable for monitoring of large-scale structures and locations which are inaccessible.

In chapter six, acoustic emission technique was applied to characterize the interfacial debonding behavior of FRP rebar reinforced concrete structures. The changes in AE parameters were closely related to damage evolution in the reinforced concrete. The AE parameters, such as AE hits, amplitude and peak frequency, indicate the debonding characteristics at different stage of the pullout test. The presented study provide meaningful information on the understanding of debonding characteristics of FRP rebar reinforced concrete structures.

Finally in chapter seven, the interfacial debonding behavior of FRP rebar reinforced concrete structures was detected and characterized by the electro-mechanical impedance technique. Statistical damage metrics, such as RMSD and MAPD were adopted to quantify the changes in the spectra of impedance and admittance. These damage metrics can clearly indicate the debonding damage evolution and classify the three stages of the carbon fiber reinforced polymer (CFRP) rebar pullout experiment. The research outlined in this work would possibly serve as a valuable reference for practical engineering in terms of debonding damage monitoring of FRP rebar reinforced concrete.

1.3 Organization of the Dissertation

The rest of the dissertation is organized as follows:

Chapter two provides an overview of the SHM, followed by the details of commonly used smart sensors, especially fiber optic sensors and piezoelectric sensors. The principles for different sensing configurations of the fiber optic sensors and the piezoelectric sensors are also detailed.

Chapter three presents the development of the combined carbon fiber/FBG active thermal probe for corrosion detection of steel reinforced concrete structures. First, the working principle of the active thermal probe was described. And finite element modeling and simulation was performed to verify the feasibility of the proposed method. Finally, accelerated corrosion experiment of a steel reinforced concrete sample was conducted to validate the efficacy of the corrosion detection method.

Chapter four presents another type of sensor for pitting corrosion measurement of metallic structures, especially pipelines. The sensor utilizes fiber optic macro-bend light loss property and the property of magnetic force changes due to the loss of ferromagnetic material. The sensing principle was described and the sensor design and calibration were investigated. The practicality of the sensor was examined through scanning over several fabricated corrosion samples with various pit shapes. The scanning results showed that the simulated corrosion pit area can be easily distinguished from the even metal background.

Chapter five presents preliminary study of using smart aggregates as embedded acoustic emission sensors for health monitoring of concrete structures. The performance of smart aggregates were compared with traditional surface mounted AE sensors, in their ability to detect and evaluate the damage of concrete structures. The frequency response of the traditional embedded AE sensors was calibrated using the Hsu-Nielsen method. A concrete beam specimen with two embedded SAs and two surface mounted AE sensors was fabricated in the laboratory, and it was subjected to under a three-point-bending test to generate AE events.

Chapter six presents the characterization of debonding behavior of FRP rebar reinforced concrete using acoustic emission technique. Carbon fiber reinforced polymer rebar reinforced concrete pullout specimen was fabricated and it was subjected to pullout test and AE monitoring. The debonding characteristics were analyzed by AE hits, amplitude and peak frequency. Finally, finite element method was used to analyze the stress distribution of the pullout specimen.

Chapter seven presents the characteristics of debonding behavior of FRP rebar reinforced concrete using electro-mechanical impedance technique. The model for debonding induced impedance variation was derived to give a clear understanding of the detection principle. Then, pullout specimen was prepared and pullout experiment was performed where the electro-mechanical impedance changes were measured by the surface-bonded PZT patch. Statistical damage metrics, such as RMSD and MAPD were adopted to quantify the changes in the spectra of impedance and admittance. These damage metrics can clearly indicate the debonding damage evolution and the three stages of the CFRP pullout experiment.

Chapter eight presents a general summary of the significant results and conclusions as well as recommendations for future work.

2 Introduction to Structural Health Monitoring and Related Smart Sensors

2.1 Structural Health Monitoring

Structural health monitoring (SHM) is the multidisciplinary process of implementing damage identification methods to a structure which involves the integration of smart sensors, data transmission, computational power and processing capability [1]. This process includes the identification of potential damage conditions for a structure, the observation of the structure continuously using distributed measurements, the extraction of damage sensitive features and the analysis of these features to find out the structural conditions of the structure [2]. SHM provides a continuously updated information on the health condition of the structure and evaluates the follow up maintenance actions.

Structural health monitoring techniques differ from conventional nondestructive testing techniques in that structural health monitoring techniques can be operated off-line as well as on-line while nondestructive testing techniques can only be operated off-line [3]. The structural health monitoring system is an on-board systems in which sensors are permanently attached (surface sensors) to structural surface or embedded (integrated sensors) in the structure. As a result, the health status of the structure is available in real-time.

According to Farrar and Doebling [4], the process of SHM is essentially a type of statistical pattern recognition. The goal of statistical pattern recognition is to group data (patterns) based on either a priori knowledge or on statistical information extracted from the patterns. The patterns to be grouped are usually the groups of measurements that define points in a high dimensional space. Statistical pattern recognition includes all stages of an investigation from problem formulation and data collection through to discrimination and classification, assessment of results and interpretation [5]. Figure 2-1 illustrates the simplified process of statistical pattern recognition, which can be divided into a diagnostic part and a prognostic part [6]. Diagnostic analysis defines the current health condition of the structure and prognostic analysis evaluates the damage evolution and estimates the residual life of the structure [7]. The diagnostic part of the structural health monitoring process consists of four steps as follow [6, 8]:

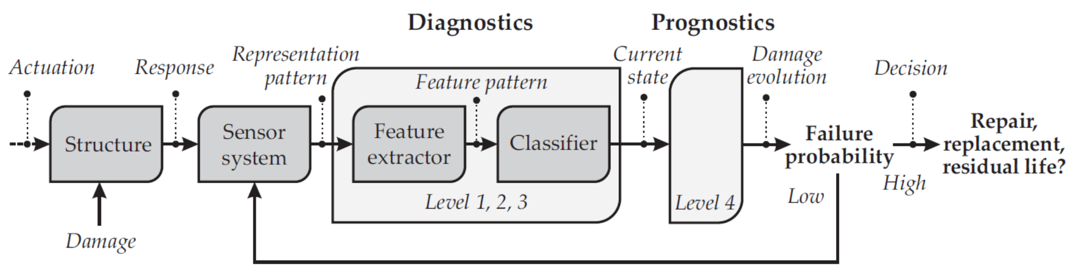

Figure 2-1 The multidisciplinary structural health monitoring process

1. Operational evaluation

Operational evaluation attempts to answer four questions regarding the implementation of the structural health monitoring system, which includes economic justification, potential damage modes, operational and environmental conditions, and limitations in data acquisition.

2. Data acquisition, normalization and cleansing

The data acquisition involves selecting the excitation methods, the sensor types, number and locations, and the hardware. Data normalization deals with separating variations in sensor reading caused by damage from those caused by varying operational and environmental conditions. Data cleansing is the process in terms of selecting useful data for the feature selection process.

3. Feature selection and information condensation

Feature selection is a process of extracting damage sensitive parameters from diagnostic measurements, numerical simulation, or accelerated testing. Since the data will be acquired over an extended period of time, information condensation reduction is necessary.

4. Statistical model development for feature discrimination

Statistical model development involves the implementation of the algorithms that operate on the extracted features to identify the damaged and the undamaged structural state and to quantify the damage state of the structure. The algorithms used can be classified into two categories, including the supervised learning (e.g., regression analysis) and the unsupervised learning (e.g., outlier detection).

Most papers published in the fields of SHM address some parts of this paradigm, and the number of studies that address all portions of the paradigm is very limited.

As stated by Doebling et al. [9], an ideal robust damage identification scheme should satisfy the following requirements: early detection of damage, able to locate the damage within the sensing capability of the sensors, estimation of the extent or severity of the damage and prediction of the remaining service life of the structural component when damage has been detected, able to isolate changes due to operational and environmental conditions. The method should also well-suited for automation and should not involve human judgment.

Damage identification of SHM has four levels according to Rytter [10],

Level 1: Determining the presence of damage in the structure;

Level 2: Determination of the location of the damage in the structure;

Level 3: Evaluating the severity of the damage;

Level 4: Predicting the remaining service life of the structure.

Levels 1 through 3 belong to the damage diagnosis, while level 4 is the damage prognosis part. Higher levels represent an increasing knowledge of the damage state and a greater need for mathematical models. For example, prediction made in level 4 is derived from fracture mechanics and fatigue life analysis.

2.2 Fiber Optic Sensors

The optical fiber has revolutionized the world of telecommunications due to its capacity to transmit large amount of information in a small footprint. The progress in optical fiber sensing technology in the past 40 years has facilitated the development of a large variety of fiber optic sensors, such as fiber optic gyroscopes, temperature sensors, vibration sensors, strain sensors, and chemical probes.

To date, the research and development of fiber optic sensor devices has extended their applications to diverse technological fields, including the civil, mechanical, aerospace, medical, and telecommunications industries [11-13]. Fiber optic sensors can be used to measure a wide variety of physical parameters, such as stress, strain, temperature, pressure, displacement, vibrations, chemical changes, electric and magnetic fields, radiation, flow, liquid level, light intensity, and color.

Fiber optic sensors are highly competitive with respect to the electrical sensors. Fiber optic sensors offer numerous advantages [14]; they

- are non-electrical devices;
- are small size;
- can be applied in normally inaccessible areas;
- are corrosion resistant and can be used in hostile environments ;
- permit remote sensing;
- are immunity to radio frequency interference (RFI) and electromagnetic interference (EMI);
- have high sensitivity, resolution and dynamic range;
- can be easily multiplexed.

Fiber optic sensors are dielectric devices that are generally chemically inert. Since they do not require electric cables for operation, they are ideal for working in hostile environments such as high voltage, high temperature, and high corrosive. In the last two decades, a considerable amount of investigations have been conducted to develop various optical fiber sensors for structural health monitoring of various kinds of engineering structures.

Fiber optic sensor consists of three basic components, which are the optical source, a transducer, and a receiver, as illustrated in Figure 2-2 [15]. Commonly used optical sources are lasers and light emitting diodes. The optical fibers are configured into the transducers to detect the physical perturbation. A photodetector is used to receive the changes in the optical signal. In the optical fiber sensors systems, the optical parameters that can be modulated are the intensity, phase, polarization, wavelength and spectral distribution.

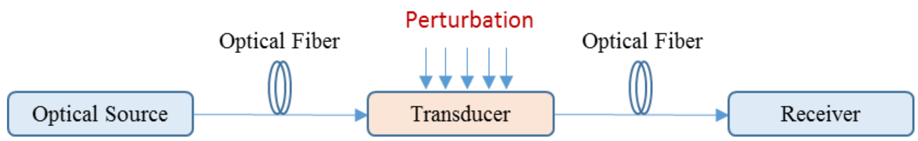

Figure 2-2 Basic components of an fiber optic sensor

Based on their operating principle, fiber optic sensors developed to date of interest for structural health monitoring can be grouped into four main types: intensity-based, grating-based, distributed, and interferometric fiber optic sensors. Different types of sensors offer different spatially-resolved measurement resolution. The intensity-based and interferometric sensors are suitable for single-point detection, while grating-based and distributed sensors can be used for quasi-distributed and distributed measurements, respectively. Figure 2-3 shows the overview of the major sensors types.

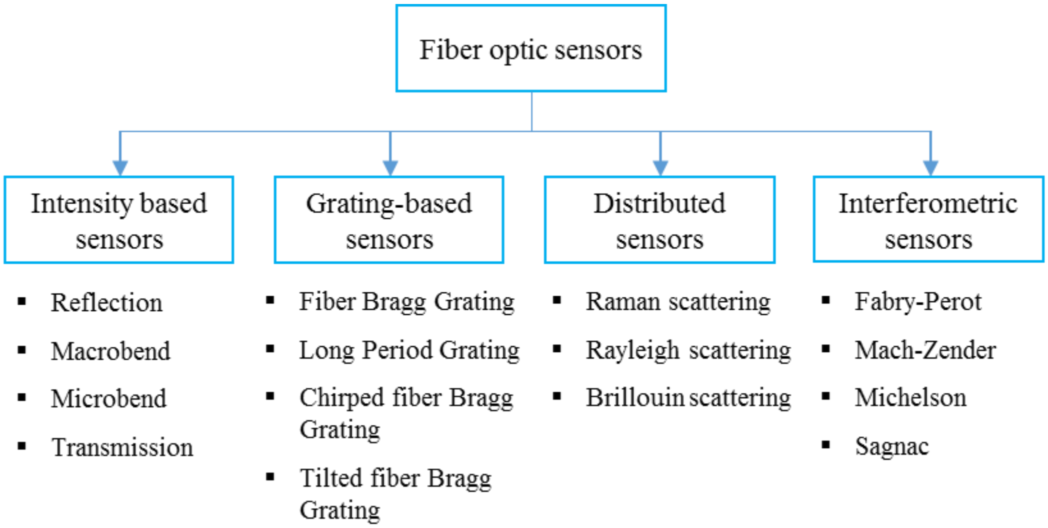

Figure 2-3 Overview of basic principles and types of fiber optic sensors

2.2.1 Fiber Optic Macro-Bend Light Loss

The transmission of light in an optical fiber relies on total internal reflection. Some light rays will leak out the fiber when total internal reflection fails due to bending of the fiber, resulting in the phenomenon of bending losses, as shown in Figure 2-4. This phenomenon is one of the issues in the field signal transmission in optical telecommunication. Derived from the coupled mode theory for optical waveguides, the mathematical model describes the power loss in a bending fiber is given as [16]:

$$2\alpha = \frac{\sqrt{\pi}\kappa^2 \exp\left[-\frac{2}{3}(\gamma^3/\beta_g^2)R\right]}{2\gamma^{3/2}V^2\sqrt{R}(\ln\gamma a)^2}, \tag{2-1}$$

where 2α is the optical power loss and R the bending radius, respectively; a is the core radius while β_g, γ, κ, V are propagation constants and waveguide quantities, respectively.

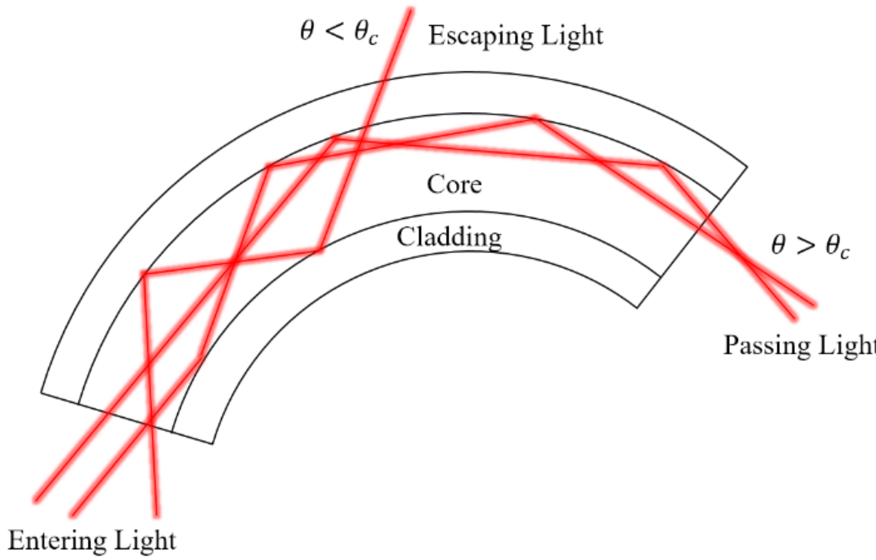

Figure 2-4 Geometrical illustration of macro-bend loss in an optical fiber

In geometrical approach the optical power leakage can be regarded as a distortion of the angle of incidence on the boundary of core and cladding due to the geometry deformation. In the case of bending of the fiber, the incident angle of the light rays become smaller than the total internal reflection angle. Some of these rays will leak from the fiber core which lead to optical power losses in the fiber. The effect of macro-bend losses of optical fiber can provide useful signal and quantity corresponding to the bend radius.

2.2.2 Fiber Bragg Gratings

A FBG is produced by inscribing a periodic and permanent modifications in the core refractive index along the optical fiber axis [17]. When a broadband light is launched through the gratings, the reflected Bragg wavelength follows the form

$$\lambda_B = 2n_{eff}\Lambda, \quad (2\text{-}2)$$

where λ_B is Bragg wavelength, n_{eff} is effective refractive index of FBG and Λ is grating period. The grating period, and therefore the Bragg wavelength, are linear to both strain and temperature. The relation between relative Bragg wavelength shift and the axial strain ε and the temperature variation ΔT is expressed as

$$\frac{\Delta\lambda_B}{\lambda_B} = C_\varepsilon \varepsilon + C_T \Delta T, \qquad (2\text{-}3)$$

where C_ε and C_T are strain and temperature sensitivity coefficients, respectively.

As illustrated in Figure 2-5, when a broadband light passes through optical fiber grating, the portion of the spectrum which equals to the Bragg wavelength of the FBG is reflected, and others can pass through the FBG with small attenuation. In this way, the interrogation of FBG sensors can be easily multiplexed using the wavelength division multiplexed (WDM) technique to realize quasi-distribution sensor network [18].

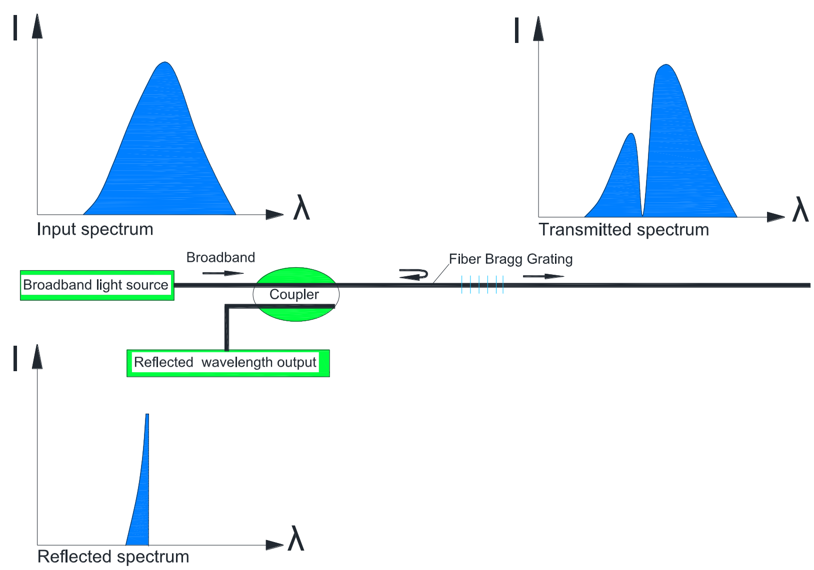

Figure 2-5 Measuring principle of the FBG sensor

2.2.3 Brillouin Fiber Optic Sensors

Brillouin scattering is a phenomenon in which a light wave transmitted in an optical fiber is scattered by the interaction with acoustic waves [19, 20]. The frequency of the scattered Brillouin light is dependent on the strain and temperature of the optical fiber, which will shift from the frequency of the incident light. The Brillouin frequency shift v_B is given by the following equation

$$v_B = \frac{2nv_A}{\lambda}, \tag{2-4}$$

where n is the refractive index, v_A is the sound wave velocity and λ is the wavelength of incident light. The Brillouin frequency shift is linearly proportion to the change of strain or temperature, which is expressed as

$$v_B(\varepsilon, T) = v_{B0}(\varepsilon_0, T_0) + C_\varepsilon(\varepsilon - \varepsilon_0) + C_T(T - T_0), \tag{2-5}$$

where $v_B(\varepsilon, T)$ is Brillouin frequency shift at strain ε and temperature T; C_ε and C_T are the strain and temperature coefficients, respectively; T_0 and ε_0 are the initial strain and initial temperature that correspond to the reference Brillouin frequency v_{B0}.

There are two types of Brillouin fiber optic sensors. Brillouin Optical Time Domain Reflectometers (BOTDR) resolve the strain or temperature based Brillouin scattering of a single pulse. Brillouin Optical Time Domain Analysis (BOTDA) uses a more complicated phenomenon known as Stimulated Brillouin Scatter (SBS).

Figure 2-6(a) shows Brillouin scattering intensity distribution at different frequencies along the optical fiber. Figure 2-6(b) shows the frequency shift of the Brillouin back scattering light at a specific location due to its corresponding strain, Figure

2-6(c) shows the Brillouin scattering intensity spectrum at a specific frequency along the optical fiber. BOTDR is very suitable for long-distance distributed strain sensing with a sensitivity of 5 $\mu\varepsilon$ [21]. However, the spatial resolution is relatively low of about 1 m and therefore this technique is not suitable for structural monitoring applications that require dense measurements.

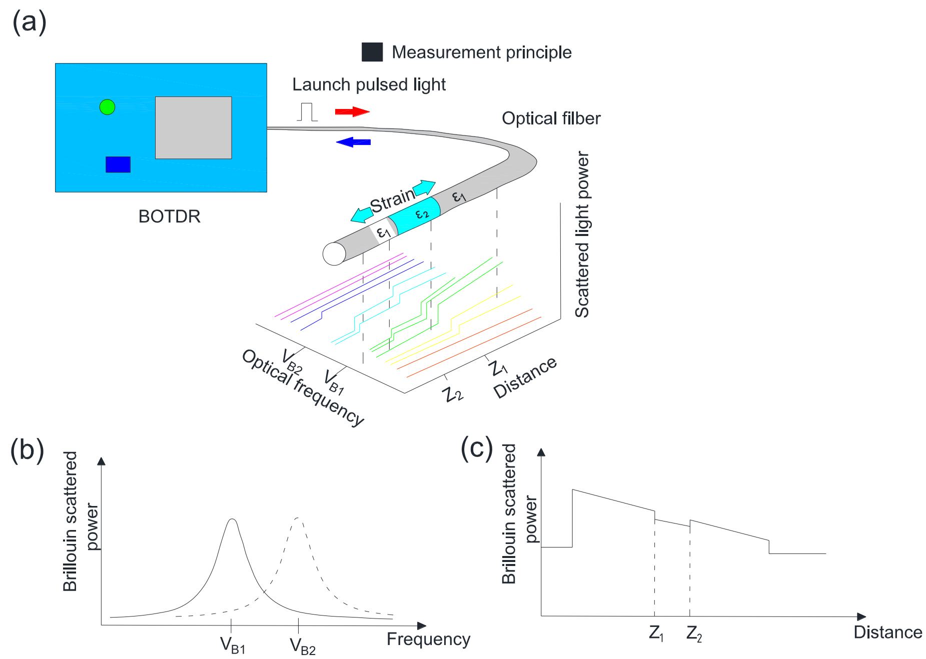

Figure 2-6 (a) The Brillouin scattering spectrum, (b) The Brillouin scattering spectrum at a specific location, (c) The Brillouin scattering spectrum at a specific frequency

2.3 Piezoelectric Sensors

Piezoelectricity is a phenomenon that a piezoelectric material is able to convert mechanical energy into electrical energy and vice versa. In a direct manner, electric charges are generated when the piezoelectric material is mechanically stressed. Conversely, the geometry of the piezoelectric material will deform according to the applied electrical field. The direct effect of the piezoelectric material can be utilized in dynamic sensing applications. And the converse effect can be used in actuation [22]. There are a few materials that possess the properties of piezoelectricity, including piezoelectric ceramics (Lead Zirconate Titanate, also known as PZT), piezoelectric polymers (Polyvinylidene Fluoride, denoted as PVDF) and piezoelectric ceramic/polymer composites, are frequently used as piezoelectric actuators and sensors for structural health monitoring of various structures [23, 24].

According to compact matrix notation [25], the coupled electromechanical constitutive equations of a linear piezoelectric material can be expressed as

$$\begin{bmatrix} D \\ S \end{bmatrix} = \begin{bmatrix} \varepsilon^T & d \\ d^t & s^E \end{bmatrix} \begin{bmatrix} E \\ T \end{bmatrix}, \tag{2-6}$$

where D and E are the electric displacement (3×1) (C/m^2) and electric field (3×1) (V/m) respectively. S and T are the mechanical strain (6×1) and stress (6×1) (N/m^2), d, ε^T and s^E are the piezoelectric strain constant (3×6) (C/N or m/V), dielectric permittivity (3×3) (Farad/m) and compliance constant (6×6) (m^2/N), respectively. The superscripts E and T indicate that the values of the constant stress respectively. When the mechanical stress/strain are in x-direction and the electrical field/displacement in z-direction, the constitutive equations can be simplified as

$$\begin{aligned} D_3 &= \varepsilon_{33}^T E_3 + d_{31} T_1 \\ S_1 &= s_{11}^E T_1 + d_{31} E_3. \end{aligned} \tag{2-7}$$

2.4 Acoustic Emission

Acoustic emission (AE) is associated with the emission and the propagation of elastic waves generated by the rapid release of internal energy due to deformation of a material [26]. AE signals can be generated as a result of various sources including dislocations, micro-cracking, and other changes due to the increase in the strain. AE method works in high frequency range, normally in the kHz range. Therefore, its sensitivity is very high, which enables it to detect incipient damage. AE sensors detect the stress waves generated from microfracture sources when they reach the material surface. An AE sensor is made by placing a piezoelectric ceramic inside an aluminum or steel casing. The piezoelectric ceramic converts the received stress wave to electric signal, amplifies the signal (internally or using external pre-amplifier), and transmits the signal to the data acquisition system. Figure 2-7 shows a schematic for AE monitoring process.

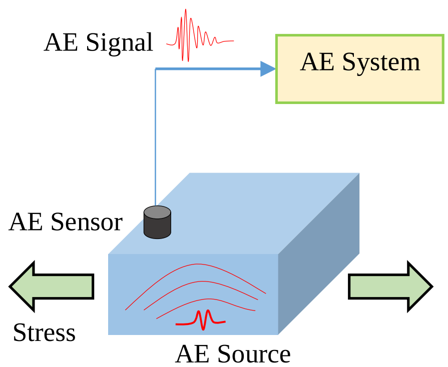

Figure 2-7 AE monitoring process

The acoustic emission signal is characterized AE parameters. Figure 2-8 shows some parameters of an AE waveform [26]. The definitions of these parameters are listed as follow [27]:

Maximum amplitude (dB): the largest amplitude of the signal expressed in decibels.

Duration (µs): the time from the first threshold crossing to the end of the last threshold crossing of the AE signal from the AE threshold.

Energy (energy unit): integral of the amplitude square of the AE signal over all the duration of the signal.

Rise time (μs): the time from an AE signal's first threshold crossing to its peak.

Counts (without dimension): the number of times the AE signal exceeds the detection threshold.

The number of events "hit": it is the counting of events having exceeded a threshold either during a time base, or throughout the test. In the first case, one speaks about rate of events, in the second of cumulated events.

Peak frequency (kHz): the frequency in the power spectrum at which the peak magnitude occurs.

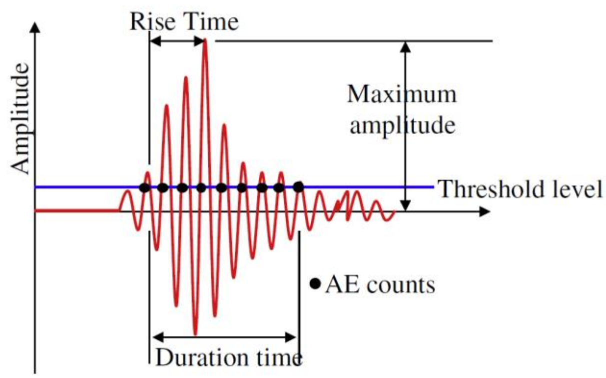

Figure 2-8 Schematic showing some parameters of an AE waveform

The passive feature of AE does not require external excitation or stimulus once sensors are installed, which makes it very suitable for real-time monitoring of in-service structures. The AE method has shown to be a promising damage assessment tool for different structures and materials including fiber reinforced polymer, metallic structures, reinforced concrete, and prestressed concrete.

2.5 Electro-Mechanical Impedance

PZT patches are small, noninvasive, and inexpensive sensors/actuators that can be easily attached to or embedded into a structure. They operate on the principle of piezoelectricity, which means surface charges are generated when mechanical stressed, and conversely, mechanical strains are produced when electric fields are applied. The Electro-Mechanical Impedance-based health monitoring techniques employ one PZT patch for both actuation and sensing of the structural responses. The PZT patches are surface-bonded or embedded into a host structure, and electrically excited by an impedance analyzer with a high frequency band (typically between 30 kHz and 400 kHz) and the electrical impedance signatures are simultaneously measured. The interaction between the PZT patch and a host structure can be idealized as an electro-mechanical system, as shown in Figure 2-9. The analytical model of this setup was first proposed by Liang et al. [28] and subsequently implemented by many others researchers [29-33]. The electrical admittance (inverse of the electrical impedance), $Y(\omega)$, of a PZT patch is related to the mechanical impedance of the host structure, $Z_s(\omega)$, and that of a PZT patch, $Z_a(\omega)$ through the following equation:

$$Y(\omega) = j\omega \frac{wl}{h}\left\{\bar{\varepsilon}_{33}^{T} - d_{31}^{2}\bar{Y}^{E} + \left(\frac{Z_a(\omega)}{Z_s(\omega)+Z_a(\omega)}\right) d_{31}^{2}\bar{Y}^{E}\left(\frac{\tan\kappa l}{\kappa l}\right)\right\}, \qquad (2\text{-}8)$$

where w, l and h are the width, length and thickness of the PZT patch, respectively; $\bar{\varepsilon}_{33}^{T} = \varepsilon_{33}^{T}(1-\delta)$ is the complex electric permittivity of a PZT patch at constant stress, where δ denotes the dielectric loss factor of a PZT patch; $\bar{Y}^{E} = Y^{E}(1+\eta)$ is the complex Young's modulus of a PZT patch at a constant electric field, η denotes the mechanical loss factor of the PZT patch; d_{31} is the piezoelectric constant of a PZT patch, $Z_s(\omega)$ and

$Z_a(\omega)$ are the mechanical impedance of a PZT patch and the host structure, respectively; $\kappa = \omega\sqrt{\rho/\bar{Y}^E}$ is the wave number and ρ is the mass density of a PZT patch.

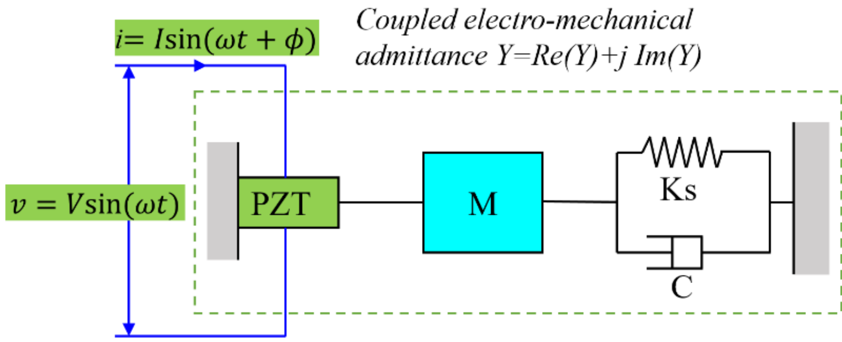

Figure 2-9 One-dimensional electro-mechanical model between a PZT patch and a host structure

Damage to a structure causes direct changes in the structural stiffness and/or damping, and thus alters the mechanical impedance of the structure. As indicated by Equation 2-8, as long as the mechanical impedance and material properties of the PZT patch remain unchanged, any modifications in the mechanical impedance of a structure results directly in the changes in the electrical impedance measured by the PZT patch.

3 Corrosion Detection of Steel Reinforced Concrete Using Combined Carbon Fiber and Fiber Bragg Grating Active Thermal Probe

3.1 Introduction

Steel reinforced concrete have become the most widely used type of material for civil infrastructures over the past several decades. The steel used in reinforced concrete relies on a protective passivation layer that fights corrosion. However, cracks in the concrete may allow the invasion of corrosive agents such as chloride to reach from the outside of the structure to the internal steel reinforcement members. Under chloride attack, the protective layer on steel is destroyed and a rust layer is formed at the concrete-steel interface. Corrosion products are usually two to six times more voluminous than that of steel [34], thus exerting expansive pressure on the surrounding concrete wall and eventually leading to concrete cover cracking, spalling and debonding. Such damages reduce the structures span of service life while adding up maintenance cost. It was estimated by the U.S. Federal Highway Administration (FHWA) in 2002 that corrosion cost was 276 billion dollars annually [35]. Thereafter, an effective and accurate corrosion detection method can help to save repairing cost and guarantee safe performance of the reinforced concrete structures.

Extensive investigations concerning corrosion monitoring for reinforced concrete structures have been conducted for the last several decades. Some commonly utilized reinforcement corrosion monitoring techniques are electrochemical measurements [36-38], ultrasonic testing methods [39, 40], infrared thermography [41, 42], fiber optic sensing [43, 44], and radio frequency [45, 46]. Each technique performs well for intended purposes, but are limited in other regards. For example, methods based on electrochemical measurements may provide information about the possibility of corrosion, but fail to quantify the accumulated amount of corrosion. Ultrasonic testing detects damage based on changes in ultrasonic wave propagation properties due to corrosion-induced structural damage. However, ultrasound is limited by short propagation distance and can insensitive to minor defects depending on the wavelength of ultrasound used. Infrared thermography, while able to detect defects that are either too small or are not visible on the surface, is constrained when concrete cover depth is large. Significant challenges also exist with fiber optic corrosion sensors, and their reliability remains low. An upcoming method is the use of active thermal probes, which have been traditionally utilized for determining a materials' thermal properties, such as thermal conductivity, thermal diffusivity, thermal resistivity and heat capacity [47-49]. The suitability of thermal probes for corrosion detection will be tested in this paper.

Active thermal probes work by generating heat and measuring the resultant transient thermal response of the surrounding material. The thermal probe usually consists of a heating wire with a temperature sensor attached to it. Heat is generated within the heating wire by passing through electric current to induce resistive heating, and the time-dependent temperature information is recorded by the temperature sensor. By analyzing the temperature history, local thermal properties can be obtained. Historical differences in thermal properties can be used to track changes in the surroundings of the thermal probe. It is well known that corrosion products have a relatively low thermal conductivity of 0.07 $\mathrm{W/(m \cdot {}^{\circ}C)}$ while concrete and reinforcement have thermal conductivity of $2.7\ \mathrm{W/(m \cdot ℃)}$ and $16\ \mathrm{W/(m \cdot ℃)}$, respectively [42]. The formation of corrosion products will modify the local thermal properties around steel reinforcement by inhibiting the diffusion of heat that is generated by the thermal probe.

Within the aggressive chloride environment, however, metallic thermal probes may not last long. To ensure the survival of the thermal probe, carbon fiber was utilized as the heating element and an optical fiber temperature sensor was used as the temperature sensing unit. Both components have the advantages of small size and corrosion resistance. Carbon fiber materials have been verified in the literature for use as a thermal source for pavement deicing [50-52]. Therefore, in our application, carbon fiber is considered as heating element in the thermal probe. On the other hand, optical fiber sensors have been widely applied in the field of structural health monitoring due to their advantages [53], such as corrosion resistance, small size, high sensitivity, immunity to electromagnetic interference, flexible shape, distributed monitoring and long distance monitoring. Zhao et al. devised a pipeline scour monitoring system based on active thermometry [54, 55], in which distributed Brillouin optical fiber is treated as temperature sensing unit. Considering the requirements of high sampling frequency and high temperature resolution in the our case, fiber Bragg grating (FBG) temperature sensing technique was employed as temperature sensing for the thermal probe.

In this chapter, a novel steel corrosion detection method is proposed for reinforced concrete based on a combined carbon fiber/FBG active thermal probe. To verify the feasibility of using the custom-made active thermal probe to detect corrosion in reinforced concrete, the thermal probe was bonded on the reinforcement surface inside a concrete block, and temperature measurements using the thermal probe were conducted periodically to detect and track corrosion severity. To corrode the reinforced concrete in a reasonable time frame, electric current was passed through the specimen, which was placed in sodium chloride solution. The proposed corrosion detection method is quite efficient in measurement, which holds significant advantages for in-situ and long term inspection of a reinforced concrete structure.

3.2 Principle of the Active Thermal Probe

3.2.1 The Principle of FBG Temperature Sensor

A FBG is created by periodic and permanent modification of the core refractive index along the optical fiber axis [17]. When a broadband light is guided through the gratings, the reflected Bragg wavelength is expressed by

$$\lambda_B = 2n_{eff}\Lambda, \tag{3-1}$$

where λ_B is Bragg wavelength, n_{eff} is effective refractive index of FBG and Λ is grating period. The grating period, and therefore the Bragg wavelength, is linearly proportional to both strain and temperature. The relation between relative Bragg wavelength shift and the applied axial strain ε and temperature change ΔT is given as

$$\frac{\Delta\lambda_B}{\lambda_B} = C_\varepsilon\varepsilon + C_T\Delta T, \tag{3-2}$$

where C_ε and C_T are strain and temperature sensitivity coefficients, respectively. For the case of pure temperature variation, the relation is simplified as

$$\frac{\Delta\lambda_B}{\lambda_B} = C_T\Delta T. \tag{3-3}$$

3.2.2 The Principle of the Active Thermal Probe

The heat generating thermal probe can be approximated as a line heat source which produces a constant heat input of q_l (W/m) in an infinite homogeneous medium at a uniform initial temperature T_0. The temperature distribution depend on the duration of heating and thermal conductivity of the medium. In mathematical form the temperature distribution can be expressed as [56]

$$\frac{\partial T(r,t)}{\partial t} = \frac{\lambda}{\rho c}\left(\frac{\partial^2 T(r,t)}{\partial r^2} + \frac{1}{r}\frac{\partial T(r,t)}{\partial r}\right) + \frac{q_l}{\rho c}, \tag{3-4}$$

where T (°C) is the temperature distribution at time t (s), r (m) is the radial distance from the heat source, λ (W/(m · °C)) is the thermal conductivity, ρ (kg/m^3) is the density of the solid, c (J/(kg · °C)) is the specific heat capacity of the solid.

For a sufficiently large time domain ($t \gg r^2/4\kappa$ and $t - t_0 \gg r^2/4\kappa$), the solution for the differential equation can be approximated as [57, 58]

$$T(r,t) - T_0 = \frac{q_l}{4\pi\lambda}\left(\ln t + \ln\frac{4\kappa}{r^2} - \gamma\right), for\ 0 < t < t_0 \text{ and} \tag{3-5}$$

$$T(r,t) - T_0 = \frac{q_l}{4\pi\lambda}\ln\frac{t}{t - t_0}, for\ t > t_0, \tag{3-6}$$

where t_0 (s) is the heating duration, $\kappa = \lambda/\rho c$ (m^2/s) is the thermal diffusivity of the solid, and $\gamma = 0.5772$ is Euler's constant. Essentially, Equation 3-5 describes the heating-up process, while Equation 3-6 describes the cooling-down process. Note that a plot of temperature against the natural logarithm of time yields a linear asymptote of slope $q_l/4\pi\lambda$. The thermal conductivity λ of the solid can thus be determined graphically.

The heat input per unit length can be computed as

$$q_l = i^2 \cdot \xi, \tag{3-7}$$

where i (A) is the electrical current and ξ (Ω/m) is the resistance per unit length. As the thermal conductivity of the material around the thermal probe changes, then for the same amount of electrical current, the time it takes to heat up and cool down the material will also change. Thus by observing the evolution of the temperature distribution profile across time, the progression of corrosion can also be tracked.

3.3 Simulation and Experimental Setup

3.3.1 Finite Element Modeling and Simulation

To analyze the feasibility of the proposed active thermal probe method for corrosion detection of reinforcement, a finite element model was established using ANSYS. The finite element model simulates the experimental configuration, which will be detailed in the following subsections. The model treats the present problem as two dimensional for the sake of easy computation. The model consists of a mortar block, steel reinforcement, a rust layer and the thermal probe, as shown in Figure 3-1. Uniform corrosion on the reinforcement surface was assumed, thus the rust layer was of constant thickness. It is challenging to measure thermal properties for the experimental prototype, thus for simulation purposes, typical material parameters for these materials are used, as listed in Table 3-1. For the transient analysis, a 4-node, 2-D thermal element PLANE55 was used. Both uniform initial temperature and ambient temperature were set at 20 ℃. Convective film coefficient on the mortar block surface was 20 W/($\mathrm{m}^2 \cdot$ ℃). To simulate the heat generated by the thermal probe, heat generation rate (HGEN) was applied, which will be valued at 99,972,882.8 W/m^3. The heat generation rate was equal to the heat input per unit length divided by cross-section area of the probe. Specifications will be detailed in the following sections. To study the effect of corrosion degree on the response of the thermal probe, different thicknesses of the rust layer was simulated. The rust thickness varied from 0 mm to 0.6 mm, with increments of 0.2 mm. After all the loads were applied, the simulation was executed for 5 seconds, including 1 second of heating and 4 seconds of cooling. Specifically, after running for 1 second, the HGEN was set to 0 W/m^3 and the simulation continued for another 4 seconds.

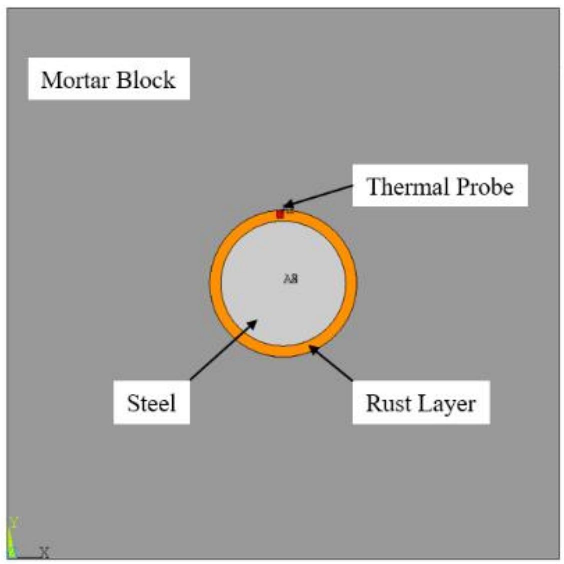

Figure 3-1 Geometry of the finite element model

Table 3-1 Materials parameters for simulation

Material	Conductivity W/(m· ℃)	Density kg/m^3	Specific Heat J/(kg· ℃)
Mortar	2.7	2,400	880
Rebar	16	7,850	450
Rust	0.07	5,120	781

3.3.2 *Fabrication of the Active Thermal Probe*

The physical thermal probe consisted of a carbon fiber bundle and an FBG made enclosed in a thin-wall stainless tubing of 0.9 mm outer diameter and 30 mm length. The heating element used was carbon fibers which were pulled into the stainless tubing, as shown in Figure 3-2(a). An FBG sensor was also pulled into and centered in the tubing. The two ends of the probe were sealed with epoxy to provide water-resistant environment. In order to prevent strain from transferring from the probe tubing to the FBG, the FBG was given some slack within the tube prior to sealing. The leading carbon fibers and transmission optical fiber were protected using heat-shrink tubes. The resistance of the thermal probe was measured to be 99.3 Ω/m. The fabricated thermal probe is shown in Figure 3-2(b).

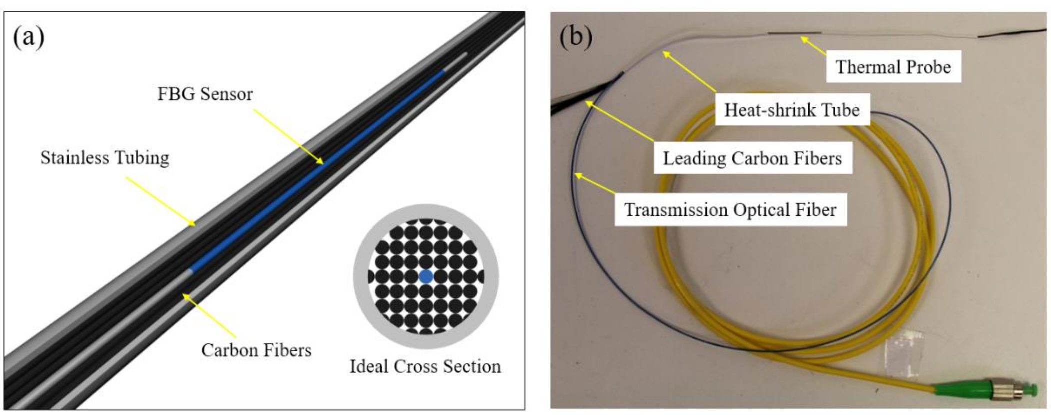

Figure 3-2 (a) Detailed view of the thermal probe; (b) Fabricated thermal probe

3.3.3 *Corrosion of the Reinforced Mortar Specimen*

The reinforced mortar block was 200 mm long, 60 mm wide and 60 mm high, as shown in Figure 3-3. The cement used was ordinary Portland cement (OPC) and the cement, water and sand mix ratio was 1:0.5:2 by weight. One deformed rebar of 150 mm long and 16 mm diameter was embedded into the center of the mortar. The thermal probe was bonded on the rebar. An electric wire was connected to one end of the rebar and the connection was sealed with epoxy to protect it against corrosion.

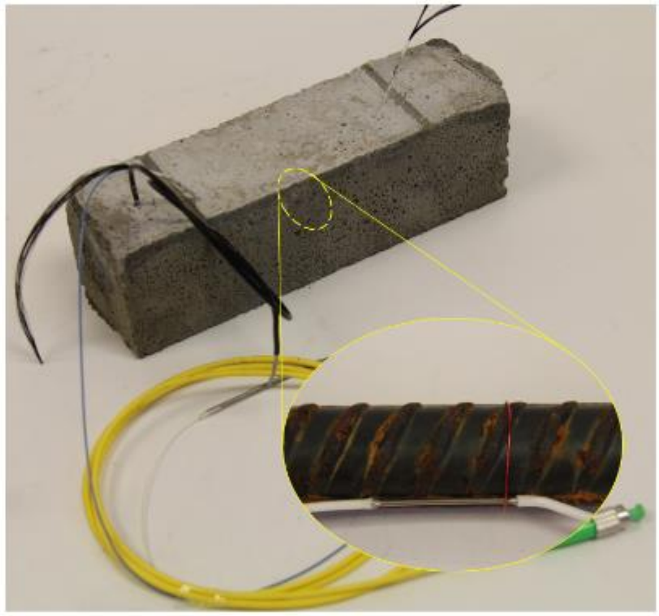

Figure 3-3 Reinforced Mortar Specimen

The mortar was cured in a moist environment for seven days before being immersed in 3.5% sodium chloride solution for three days for an accelerated corrosion test. After seven days, the thermal conductivity has been shown to no longer change significantly. After three days of being immersed in sodium chloride solution, a constant current of 50 mA was applied through the rebar. The rebar was connected to the positive pole of the power supply and the sacrificial stainless steel plate was connected to the negative pole, as shown in Figure 3-4. The presence of water could affect the response of the thermal probe significantly. To reduce the effect water presents inside the specimen, the specimen should be dried before conducting measurements using the thermal probe. The specimen was subjected to wet-dry cyclic corrosion tests to study the response of the thermal probe under different degrees of reinforcement corrosion. One cycle includes implementing accelerated corrosion for five days and air-drying for three days before alternating again. The impressed current was discontinued during air-drying. The air-drying process produced a dry ambient environment around the thermal probe prior to thermal tests, eliminating the influence of moisture on the heat transfer through conduction.

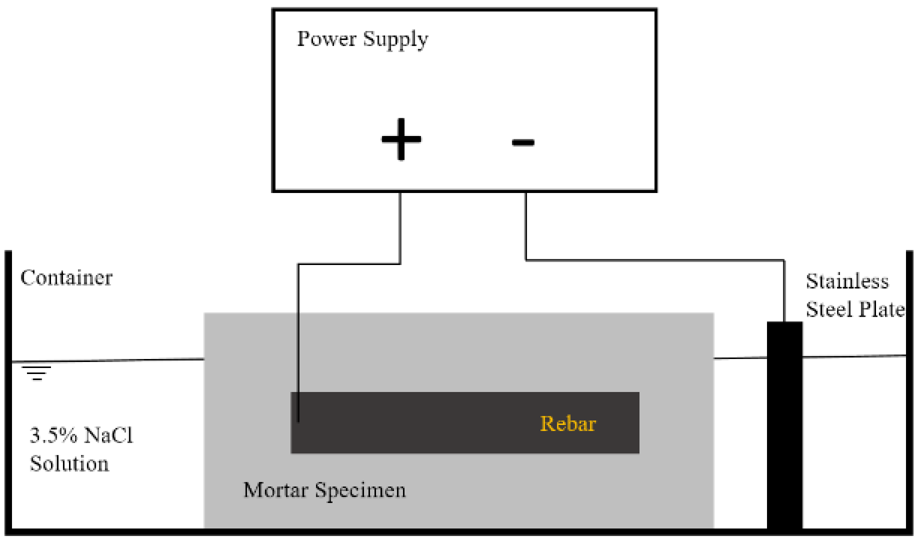

Figure 3-4 Accelerated corrosion test

3.3.4 Active Thermal Probe Experiment Setup

The instrumentation for active thermal probe experiments was divided into two parts, which were heat control and temperature sensing, as illustrated in Figure 3-5. The thermal probe was connected to a programmable power supply (6542A, Agilent). The heating and cooling time, and the applied heating current were controlled by the power supply via NI USB-6363 DAQ-card using a custom LabVIEW program. As for the temperature sensing, the FBG temperature sensor was interrogated by an FBG interrogator (sm130, Micron Optics) and the data was saved at 1000 Hz. The applied heating current was selected to be 0.8 A, which was large enough to heat up the thermal probe while still be handled by the power supply. For the thermal probe experiments, three different heating times were chosen: 0.5 second, 1 second and 2 seconds. The duration including heating and cooling for each test was 5 seconds. The measurements were repeated three times.

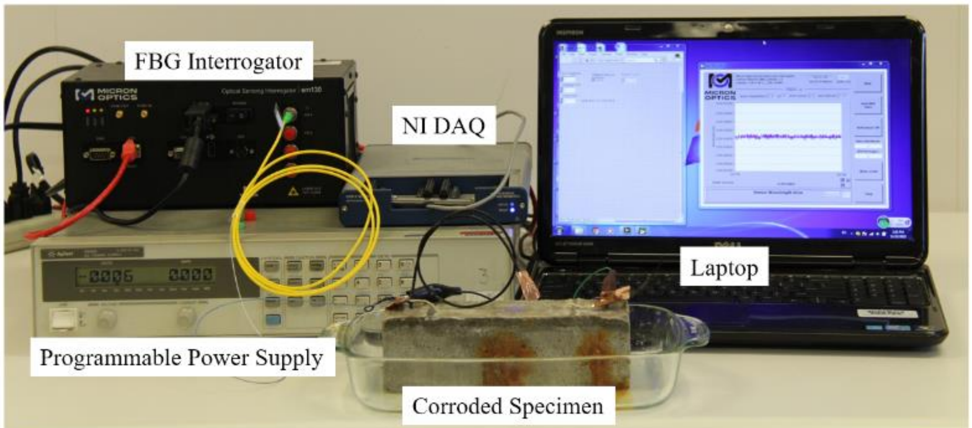

Figure 3-5 Instrumentation for thermal probe experiments

3.4 Results and Discussion

3.4.1 Finite Element Simulation Results

The temperature response of different rust thicknesses obtained via finite element simulation is given in Figure 3-6. It can be seen that the temperatures rise quickly when the heating power is on, and returns to the initial temperature gradually after the heating power is off. The max temperatures and heating rate became higher with the increase of rust thickness. The results show that the rust, which has much poorer thermal conductivity, will impede heat propagating away from the active thermal probe and result in higher temperatures. According to theoretical analysis and finite element simulation, it is verified that the proposed corrosion detection through the use of the active thermal probe for reinforced concrete structures is feasible.

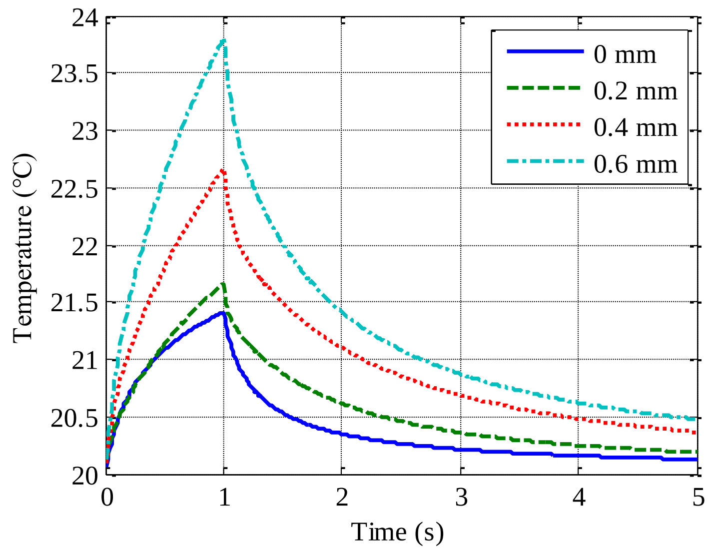

Figure 3-6 Temperature response for different rust thickness under 1 s heating time from finite element simulation

3.4.2 *Experimental Results*

In order to predict mass loss during the accelerated corrosion test, Faraday's law is adopted as in Equation 3-8.

$$\Delta m = MIt/zF, \tag{3-8}$$

where Δm (g) is the mass of steel consumed, M (g) is the atomic weight of metal (56 g for Fe), I(A) is the current, z is the ionic charge (z = 2), F (A/s) is the Faraday's constant (96,500 A/s) and t (s) is the duration. For each wet-dry cycle lasting 5 days, the mass loss is thus 6.26 g. The original mass of the rebar is 219 g and hence the corrosion amount for each wet-dry cycle is 2.86 %. Also, the wavelength shift is converted to temperature variation using a temperature sensitivity coefficient of 10.3 $\mathrm{pm}/^{\circ}\mathrm{C}$, which was calibrated through a warm water bath beforehand.

The original signal contains a certain amount of instrumentation noise (approximately 0.001-0.002 nm). In order to reduce the effect of the noise on the gathered data, wavelet threshold denoising was performed using MATLAB. Figure 3-7 presents the results of temperature change and their corresponding maximum temperatures as a function of time for different corrosion degrees when the heating time was set to 0.5 s. The maximum temperatures plummeted when the reinforcement reached 8.58 % corrosion severity. The presence of a crack was verified visually and the time of its presence was coincident with the drop in maximum temperature. It appeared that the mortar specimen was cracked due to the expansive stress exerted by the accumulation of corrosion products after 5.72 % corrosion degree. Before specimen cracked, the temperatures increased logarithmically when the heating current is injected, and quickly return to the initial temperatures the moment the heating current is disconnected. The rate and maximum temperature increased as the corrosion became more severe. This phenomenon can be explained by the poor thermal conductivity of corrosion products, which act as thermal inhibitor, and thus lead to a faster increase rate and higher temperature. Therefore the thicker the rust layer, the larger the heating rate and maximum temperature. However, after cracking, the maximum temperature dropped dramatically to a lower value. The drop in maximum temperature may be attributed to convective cooling as now the corrosion area is now exposed to air and heat is no longer trapped as easily as before cracking. The crack opening exposes the thermal probe to air and allowed for convection. The heat generated from the thermal probe dissipated faster through convection with air, resulting in a lower temperature increase rate and lower maximum temperature. As the corrosion became more severe, the cracks became wider and in the process exposed additional surface area of the thermal probe to air. With more area exposed, the heating rate and max temperature is further driven down. It may be noted that, with other variables such as weather being equal, tracking the maximum temperature measured by the sensor can be an indirect way to indicate cracking since cooling since crack-enabled convection will be the only major factor reducing the maximum temperature. Figure 3-8 and Figure 3-9 show the cases for 1 s heating time and 2 s heating time, respectively. Both of these cases show similar results with the case of 0.5 heating time, but with larger maximum temperatures due to the larger amount of heat input.

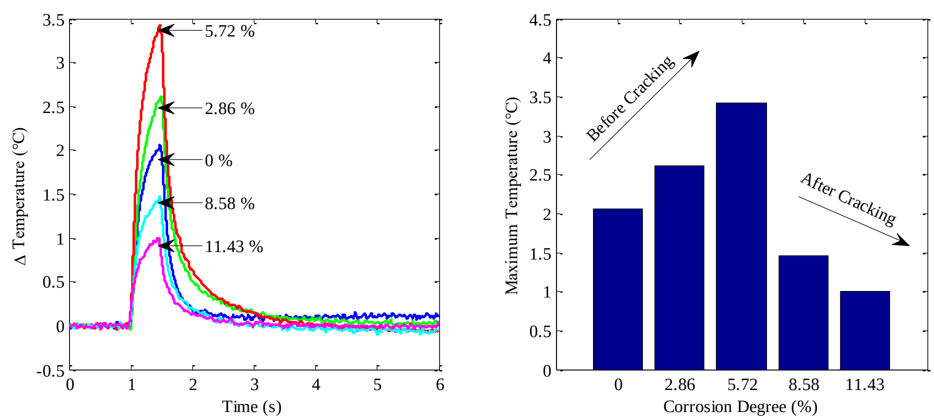

Figure 3-7 Temperature versus time response of different corrosion degree under 0.5 s heating time and their corresponding maximum temperatures

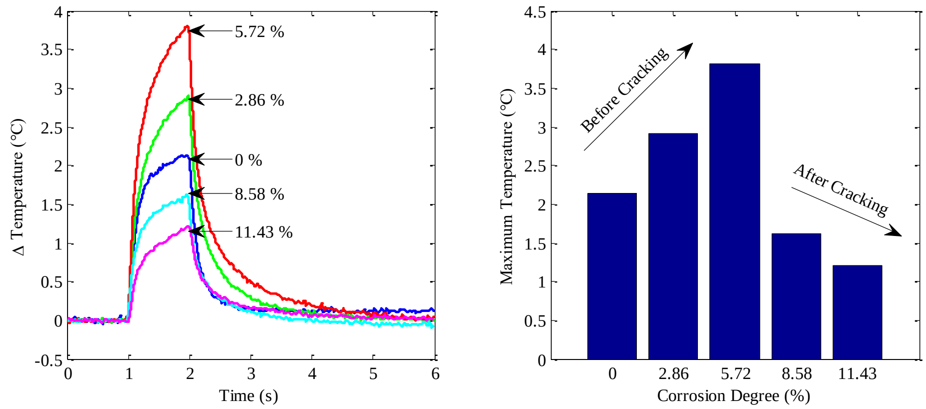

Figure 3-8 Temperature versus time response of different corrosion degree under 1 s heating time and their corresponding maximum temperatures

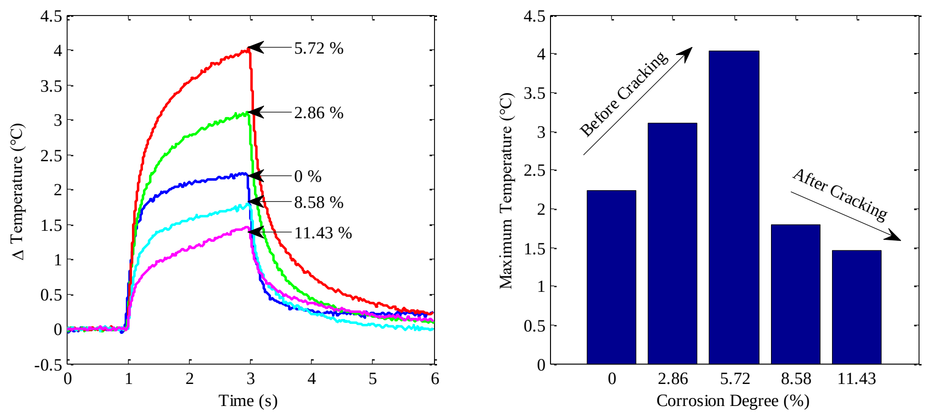

Figure 3-9 Temperature versus time response of different corrosion degree under 2 s heating time and their corresponding maximum temperatures

As indicated by Equation 3-5, the temperature has a linear relationship with the natural logarithm of time. The equivalent thermal conductivity surrounding the probe can be calculated from the slope of the rise in temperature against a logarithmic time interval. A longer heating duration usually yields a more obvious linear trend, therefore the case of 2 s heating time is taken for analysis. The mathematical model is valid only when there is no convection heat transfer involved, hence the temperatures after cracking are not included. Figure 3-10 plots the temperature versus the logarithm of time for different corrosion degrees. The points that vary linearly with the logarithm of time are from 0.25 to 1.08, corresponding to 1.28 s to 2.95 s in the original time scale. The linear curves are fitted in this larger time domain. As can be seen from the figure, the slope of the fitted curve increases in proportion to the severity of corrosion. From the slope, the thermal conductivity of the material surrounding the probe can be determined. The slope equals to $q_l/4\pi\lambda$ and $q_l = i^2 \cdot \xi$ with i = 0.8 A and ξ = 99.3 Ω/m. The calculated thermal conductivity for different degrees of corrosion is shown in Figure 3-11. The thermal conductivity shows a decreasing trend as more corrosion products are generated around the thermal probe. The results confirm that generation of corrosion products leads to a poorer thermal conductivity around the probe, which inhibits the diffusion of heat inside the mortar specimen.

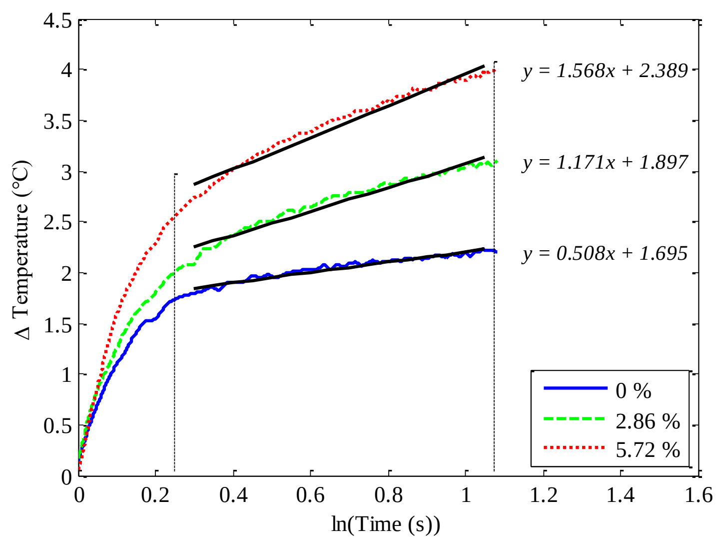

Figure 3-10 Temperature versus logarithm of time of different corrosion degree under 2 s heating time and their linear fit equations

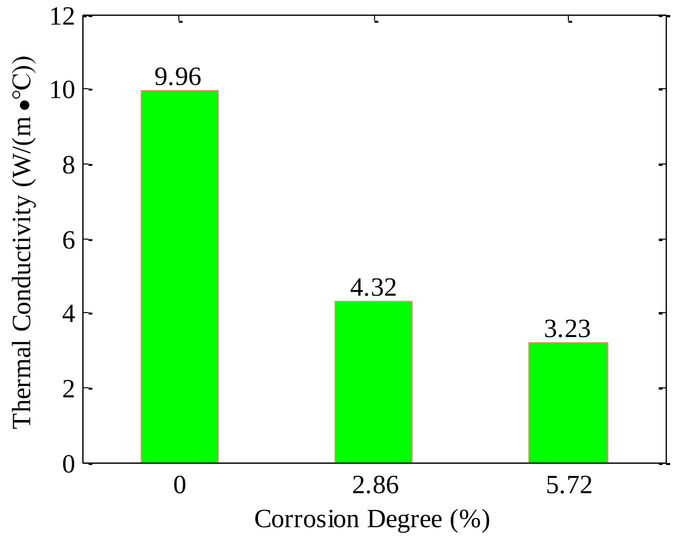

Figure 3-11 The thermal conductivity surrounding the thermal probe

Figure 3-12 shows the cracked mortar and the thermal probe. It should be stressed that the calculated thermal conductivity is not for a specific material, but the equivalent thermal conductivity around the thermal probe. Note that when there is no corrosion, the thermal probe is surrounded by mortar and rebar. The thermal conductivity for mortar and rebar are 2.7 W/(m· ℃) and 16 W/(m· ℃), respectively. The calculated equivalent thermal conductivity at the interface between mortar and rebar valued at 9.96 W/(m· ℃), right between those of mortar and rebar. The presence of corrosion products, which has a much smaller thermal conductivity of 0.07 W/(m· ℃), lower the equivalent thermal conductivity to smaller values.

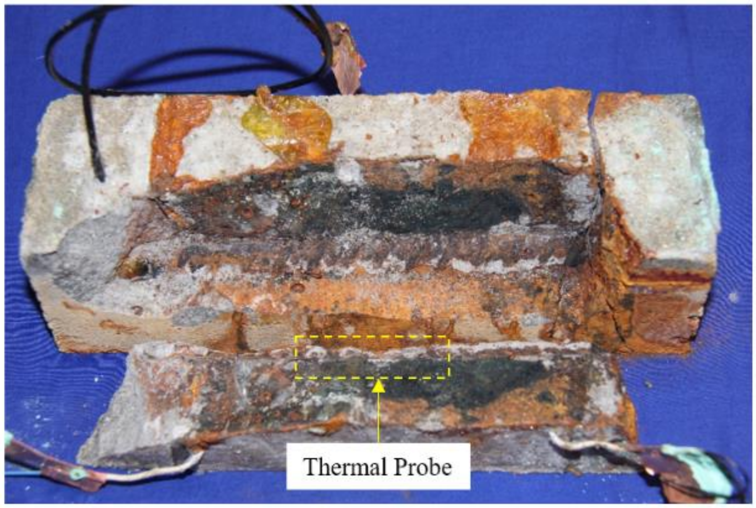

Figure 3-12 Cracked mortar exposing the thermal probe

This research is an attempt to investigate the feasibility of reinforcement corrosion in concrete structures through the use of an active thermal probe. From theoretical analysis, finite element simulation and laboratory experiments, the proposed method provides an accurate and efficient alternative to detecting reinforcement corrosion. With the help of high frequency sampling of FBG temperature sensors, corrosion detection can be done within seconds. The thermal probe is small in size, with minimal intrusion to the concrete structures. Therefore, the thermal probe can be embedded inside the concrete structure in the long term and provide automated periodic corrosion monitoring. The current results are qualitative in nature, and further investigations are required to relate the temperature response to the corrosion severity. The effect of environmental changes, such as moisture content and temperature, should be treated carefully before the technique is applied. Since real world concrete structures are not always in a dry environment, experiments should be performed to study the effect of moisture content on the response of the thermal probe. Also, seasonal changes of the environment may affect the performance of the active thermal probe. To compensate for such factor, one possible solution would be to install a reference probe in the vicinity of the one that in service but with certain distance from the reinforcement so that the only difference between these two probes is whether or not they are in contact with corrosion products. One shortcoming of the proposed thermal probe design is that it can only test one point in one measurement, though quasi-distributed can be achieved by the multiplexing nature of FBG sensors. It would be interesting and challenging to develop a distributed thermal probe based on distributed fiber optic temperature sensing techniques.

As a final point of discussion, one may be concerned with the sensor performance parameters, such as resolution, accuracy, and sensitivity of the active thermal probe. Determination of resolution and accuracy in this case will require a quantitative measurement of corrosion in order to calibrate the sensor temperature readings. In the experiment described in this paper, this was done through measuring the mass of the sample and inputting the data into Equation 3-8 to obtain the corrosion severity. In practical scenarios, where the sensor may be embedded in a large structure, such a method cannot be used. Thus at the current stage of development, a number is not yet assigned to the resolution and accuracy of the sensor, although future studies may be able to calibrate the sensor, concrete type, and rebar type to more universal measures of corrosion, such as rust layer thickness. On the other hand, the resolution of the FBG itself can be used as a temporary description of the sensor resolution. The FBG has a temperature resolution of 0.1 ℃, meaning that changes in corrosion must be large enough to cause a max temperature shift (due to the heat pulse injection) preferably by more than

0.1 ℃ (e.g. a max temperature shift from 4 ℃ to 4.1 ℃ to increase in corrosion severity). However, as of now, a general measurement of corrosion other than as described in Equation 3-8, which cannot be applied to large structures, is unavailable.

The nature of probe's sensitivity, however, can be partially deduced from the data. As seen in Figures 3-7 through 3-9, an increase of heating time pushed the maximum temperature higher, and for different corrosion severities, the difference in maximum temperature per heating time diverged greatly. Therefore, increases in heating time in fact increases the sensitivity, albeit in a qualitative sense. Once cracking has occurred, however, the situation becomes harder to control; although from Figures 3-7 through 3-9, increasing corrosion after cracking leads to faster cooling due to widening of the crack and increasing areas exposed to convection. Practically, the heating time can be increased to much more than 2s as in the experiment, however, there will reach a point where the tradeoff between sensitivity and power consumption/efficiency may become an issue. At this point, the experiment has shown that 0.5-2s heating time was enough for differentiating the corrosion stages. It may also be noted that for longer heating times, more linear curve fits can be made to the heating process, as seen in Figure 3-10.

3.5 Conclusions

In this chapter, a novel reinforcement corrosion detection technique was proposed based on the use of a novel carbon fiber/FBG active thermal probe. The fabricated thermal probe has a simple structure consisting of a bundle of carbon fibers, an FBG sensor and an encapsulating stainless tubing. The corrosion detection technique takes advantages of the relatively poor thermal conductivity nature of corrosion products, whose conductivity value is two orders of magnitude less than those of concrete and steel. Therefore, the corrosion products have the effect of inhibiting heat propagation. By placing the thermal probe on the reinforcement, the presence of corrosion products can be detected by analyzing temperature response measured by the thermal probe. The heat transfer model of thermal probe heat generation and cool-down process was analyzed theoretically, and finite element simulation was performed to verify the feasibility of the proposed corrosion detection scheme. The results show that there is a strong correlation between corrosion degree and temperature response. Increased degrees of corrosion lead to higher temperature on the thermal probe when a short duration of heat pulse is applied. Experimental results further verify the proposed corrosion detection technique. The equivalent thermal conductivity surrounding the thermal probe was calculated for different corrosion severities. From a more straightforward perspective, the presence of corrosion products reduce the equivalent thermal conductivity significantly. The experimental results demonstrate the feasibility and potential of the proposed corrosion detection technique for practical applications. Further work is necessary to fully understand the correlation between the corrosion degree and the temperature response measured by the thermal probe.

4 Fiber Optic Macro-bend Based Sensor for Detection of Metal Loss

4.1 Introduction

The loss of metal in critical structures, commonly due to corrosion, is widespread and urgent problem across many industries. Corrosion is the irreversible consumption of metal or metal alloy due to the chemical reaction with its environment. Progressive corrosion and the consequential metal loss leads structural failure and economy loss, and in severe situations can be a culprit for some cases of injury and loss of life. It is reported by U.S. Federal Highway Administration in 2002 that U.S. alone spends 276 billion dollars annually for anti-corrosion design, manufacturing, construction and management [35]. Therefore, it is very important to monitor and characterize metal loss due to corrosion in metallic structures and accurately assess their performance and safety. While many non-destructive test (NDT) techniques have been developed to monitor and measure corrosion, a reliable method is more desirable.

Since corrosion is an electrochemical process involving the transfer of ions and electrons, electrochemical methods have been widely used for evaluation of corrosion in metallic structures. One of the commonly used electrochemical methods is the half-cell potential method which takes advantage of the electrochemical nature of corrosion and indicates the likelihood of corrosion by measuring the electrical potential difference [59]. A more negative value of potential difference usually represents a higher corrosion probability. The major limitation of this method is that it can only suggest the possibility of the corrosion occurrence and unable to give a quantitative measure of the accumulated amount of corrosion. Other techniques are available such as electrochemical noise measurements [60], pH measurements [61], and ultrasonic guided wave measurements [62]. These techniques lack the ability to quantify corrosion level and their testing procedures are complicated as well. The drawbacks of these traditional non-destructive methods to accurately measure the corrosion extent illustrate the necessity for new sensing techniques to determine corrosion.

Optical fiber sensing techniques have been emerging as powerful structural health monitoring tools in different fields of application [63-70]. Fiber optic devices are promising for corrosion sensor application systems due to their advantages of small size and low weight, immunity to electromagnetic interference, corrosion resistance and the potential for remote operation. A number of different approaches have been investigated over the last decades for the measurement of corrosion using fiber optics: metallized optical fiber [71-73], fluorescence [74-76], interferometry [77, 78], fiber Bragg grating wavelength shifts [79-83] and Brillouin scattering [44, 84]. These fiber optic corrosion sensors require either complex processing of the fiber such as the fabrication of metallized optical fiber and fiber Bragg grating, or expensive instrumentation such as the Brillouin scattering based sensors. Fiber optic sensing based on macro-bend loss rely on the modulation of light intensity loss due to the bending of optical fiber, which has the advantage of simple structure and low cost. Recently, significant efforts have been made by researchers to utilize the bend loss properties of single mode fiber for various sensing applications such as displacement sensor, seismic sensor, liquid level sensor and temperature sensor [85-88]. Up to now, there have been no reports about the corrosion measurement using fiber optic macro-bend properties.

In this chapter, a novel type of ferromagnetic distance sensor was proposed based on the principle of fiber optic macro-bend loss, with the aim to measure the metal loss due to corrosion, or any other process that can cause metal loss. The proposed fiber optic macro-bend distance sensor utilizes the phenomenon of bending losses of light intensity inside optical fiber which is dependent on the radius of bending. The sensor was composed of the bended optical fiber cable, the magnet and the restoring element (typically a spring). The magnet was attached to the restoring element and the fiber bend was arranged in such a way that the movement of the magnet will induce a change in bending radius of the optical fiber and thus the light intensity signal. One end of the bended fiber was connected to a laser source and the other was connected to a photodetector, from which the signal was further processed by a data acquisition unit and computer. Sensor configuration like this ensures low cost while maintains high accuracy. Ferromagnetic metal loss due to corrosion increases the distance between the magnet and the metal surface and thereby reducing the magnetic force. The change in magnetic force induce the change in light intensity loss of the fiber, thus corrosion pits can be detected by the proposed sensor. The practicality of the proposed distance sensor for corrosion measurement was validated through scanning the fabricated corrosion samples.

4.2 Operating Principle of the Sensor

The transmission of light in an optical fiber relies on total internal reflection. Some light rays will leak out the fiber when total internal reflection fails due to bending of the fiber, resulting in the phenomenon of bending losses, as shown in Figure 4-1. This phenomenon is one of the issues in the field signal transmission in optical telecommunication. Derived from the coupled mode theory for optical waveguides, the mathematical model describes the power loss in a bending fiber is given as [16]:

$$2\alpha = \frac{\sqrt{\pi}\kappa^2 \exp\left[-\frac{2}{3}(\gamma^3/\beta_g^2)R\right]}{2\gamma^{3/2}V^2\sqrt{R}(\ln\gamma a)^2}, \tag{4-1}$$

where 2α is the optical power loss and R the bending radius, respectively. a is the core radius while β_g, γ, κ, V are propagation constants and waveguide quantities, respectively.

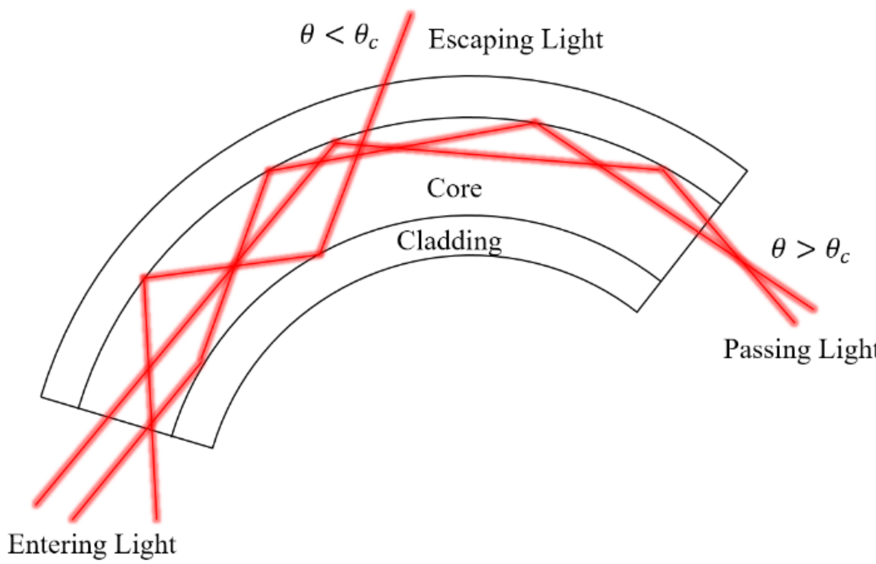

Figure 4-1 Geometrical illustration of macro-bend loss in an optical fiber

In geometrical approach the optical power leakage can be regarded as a distortion of the angle of incidence on the boundary of core and cladding due to the geometry deformation. In the case of bending of the fiber, the incident angle of the light rays become smaller than the total internal reflection angle. Some of these rays will leak from the fiber core which lead to optical power losses in the fiber. The effect of macro-bend losses of optical fiber can provide useful signal and quantity corresponding to the bend radius. Figure 4-2 shows the relationship between light intensity and the bend radius of a single mode optical fiber from experimental configuration. The light intensity is measured and converted to voltage using a photodiode. The output voltage is amplified (20 times) to give better resolution. As can be seen from the figure, there is no significant power loss when the bending radius is larger than 4 mm and the optical power is totally lost when the bending radius is less than 3 mm. Significant light loss is experienced between 3 mm and 4 mm bending radius. This sensitive region can be used to form the radius of the macro-bend sensor. In the proposed sensor system, the optical power losses provide useful information about the corrosion induced metal loss on the metal surface.

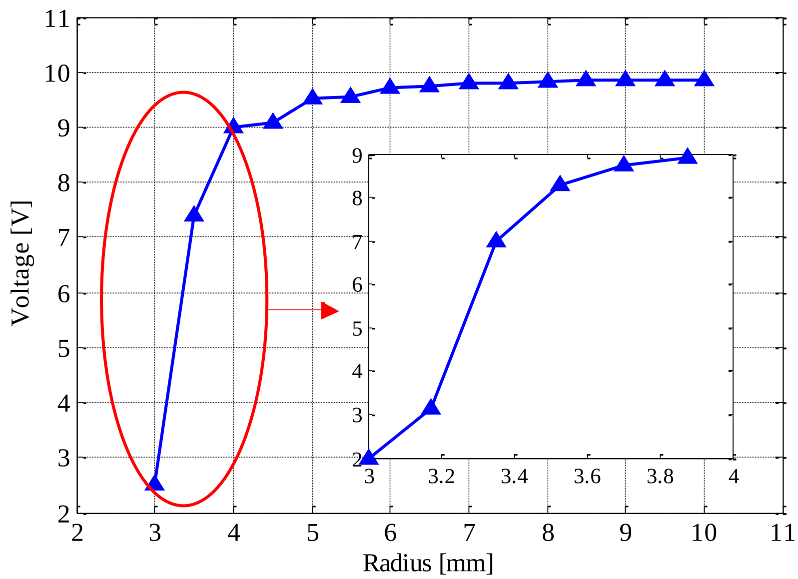

Figure 4-2 Output voltage versus bend radius for a single mode optical fiber

4.3 Sensor Design and Experimental Setup

4.3.1 Sensor Design and Calibration

In this section, the sensor fabrication process and the measurements of the sensor calibration curves are reported. Figure 4-3 shows the schematic and photograph of the fabricated ferromagnetic distance sensor. The proposed fiber optic macro-bend sensor consists of three major components, the bended optical fiber, the magnet and the spring. The magnet was connected to the spring and the single mode optical fiber bend was attached to the spring using epoxy glue. Arrangement like this ensures that the movement of the magnet will induce a change in bending radius of the optical fiber and thus the light intensity signal. The cylindrical magnet has a diameter of 4.7 mm and height of 12 mm, whose magnetization direction is along its axial direction. The bended optical fiber has an initial radius of 4 mm. The stiffness of the spring is 750 N/m. A ball bearing was used to guide the axial movement of the magnet as well as to minimize the friction. All these components were packed inside an outer casing, which was fabricated by 3D printing. The casing has a diameter of 30 mm and a height of 100 mm. The two ends of the bended fiber were passed through the casing, one was connected to a laser source and the other end was connected to a photodiode.

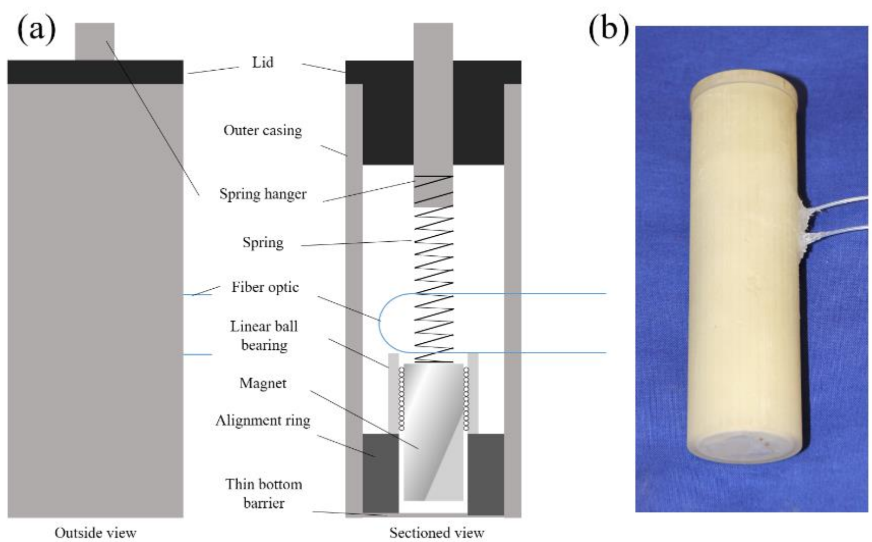

Figure 4-3 (a) Schematic drawing of the optical fiber macro-bend distance sensor; (b) Photograph of the fabricated distance sensor

The static calibration of the sensor is to obtain the response of the sensor versus the distance between the sensor head and the ferromagnetic material. The setup of static calibration of the fiber optic macro-bend distance sensor is schematically shown in Figure 4-4(a). The light source was launched into the bending section of the sensor before reaching the photodiode. The light intensity variation due to bending radius change was converted to voltage signals using a photodiode. The light source used is a C-band (1528 nm - 1563 nm) amplified spontaneous emission [14] light source (Opeak Technology Cooperation). The voltage output from the photodiode was amplified using amplifying circuits (20 times amplification) and it was then received by a data acquisition (DAQ) board (myDAQ, National Instruments). The voltage signals were processed and stored on a personal computer using LabVIEW.

The static calibration of the sensor was performed on a translation stage, as shown in Figure 4-4(b). A steel plate was fixed on the lower part of the translation stage and the sensor was fixed on the upper part of the stage. The distance between the sensor and the steel plate was varied by moving the lower part of the translation stage upward or downward. The output voltages corresponding to different distance between the sensor head and the steel plate were recorded. The distance was calibrated using a laser displacement sensor (MX1A, IDEC Corporation), which has a resolution of 10 μm. The measurements were repeated for ten times to check to repeatability of the sensor.

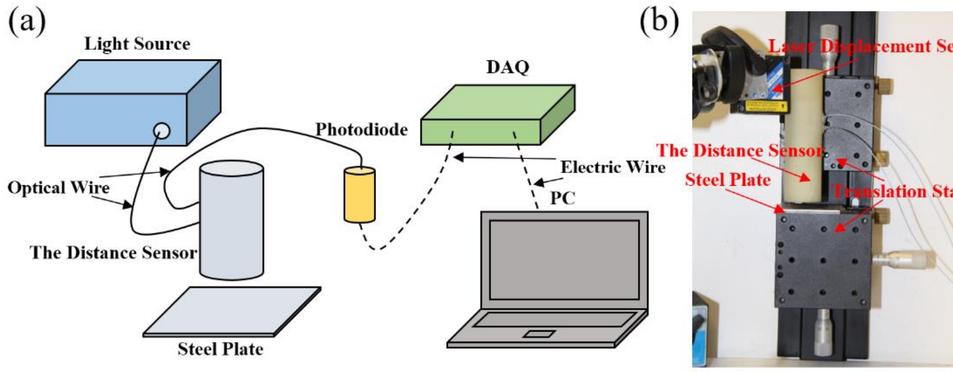

Figure 4-4 (a) Schematic of the experimental setup for calibrating the distance sensor; (b) Photograph of the static calibration on a translation stage

The dynamic response of the sensor was performed in the same manner as the static calibration. As shown in Figure 4-5, the steel plate was fixed on a flexible aluminum beam. The beam was cantilevered and free vibration of the beam was initiated by offsetting the free end with an initial displacement. The senor was placed over the steel plate to measure its dynamic response. As for comparison, a laser displacement sensor was also used to measure the vibration of the steel plate.

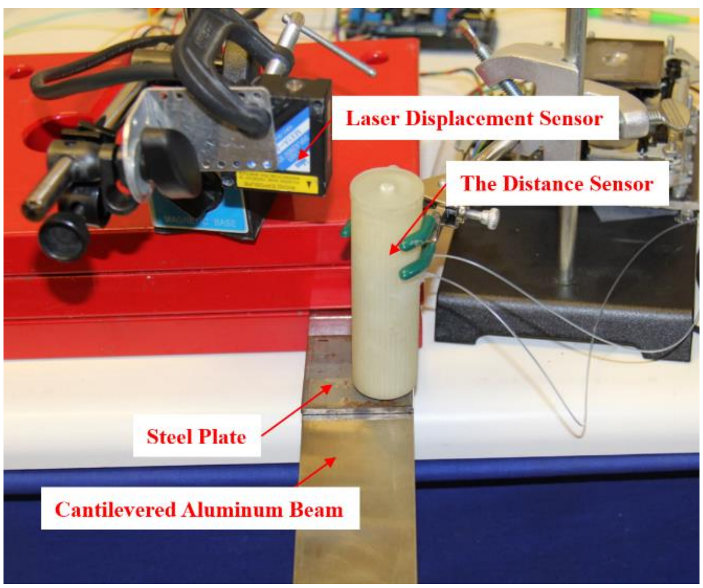

Figure 4-5 Experimental setup for calibrating the dynamic response of the sensor

4.3.2 Corrosion Samples Scan Experiments

To validate the feasibility of the proposed distance sensor for measuring pitting corrosion on the surface of the ferromagnetic materials, several corrosion samples were fabricated in laboratory. The corrosion samples were made from steel plates (length: 50 mm, width: 50 mm, thickness: 3.3 mm). These corrosion samples have various corrosion pit shapes which were commonly encountered in real world situation, including wide shallow pit, narrow deep pit, elliptical pit and subsurface pit. Three corrosion samples were prepared as shown in Figure 4-6. The elliptical sample can be regarded as subsurface pit sample by flipping itself over.

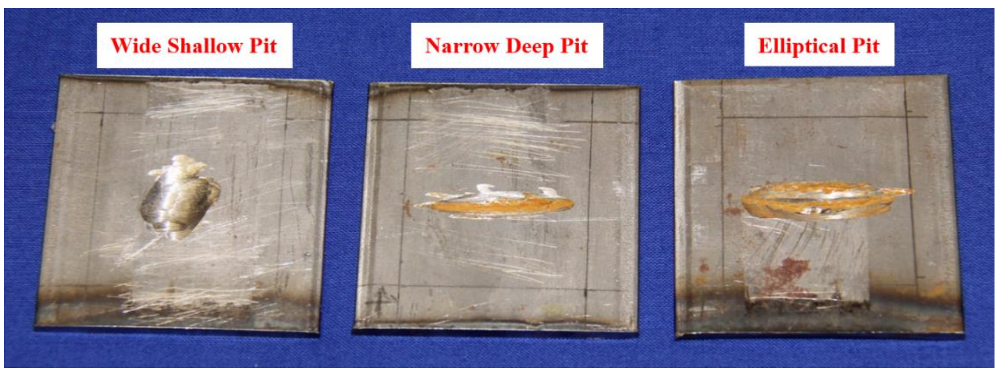

Figure 4-6 The fabricated corrosion samples.

The experimental setup for scanning the corrosion samples is shown in Figure 4-7. A two dimensional scanning stage was built using two guiding trails from old CD players. These guiding trails were arranged perpendicular to each other. The maximum travel distance of the trails is 34 mm. A microcontroller (Arduino Mega) was utilized to control the movement of the scanning stage via a motor shield (L293D, MH Electronics). Finally, the DAQ board, programed by LabVIEW code in the personal computer, gave instruction to the microcontroller to move the scanning stage. In the meantime, the DAQ board recorded the voltage output from the photodiode corresponding to the specific location. Prior to performing the corrosion sample scanning experiments, the corrosion samples were placed on the scanning stage and the sensor was overhung above the corrosion sample. To provide reference measurement of the geometry of the corrosion pits, the corrosion samples were also scanned using the laser displacement sensor. The measurements for each corrosion samples were repeated 10 times.

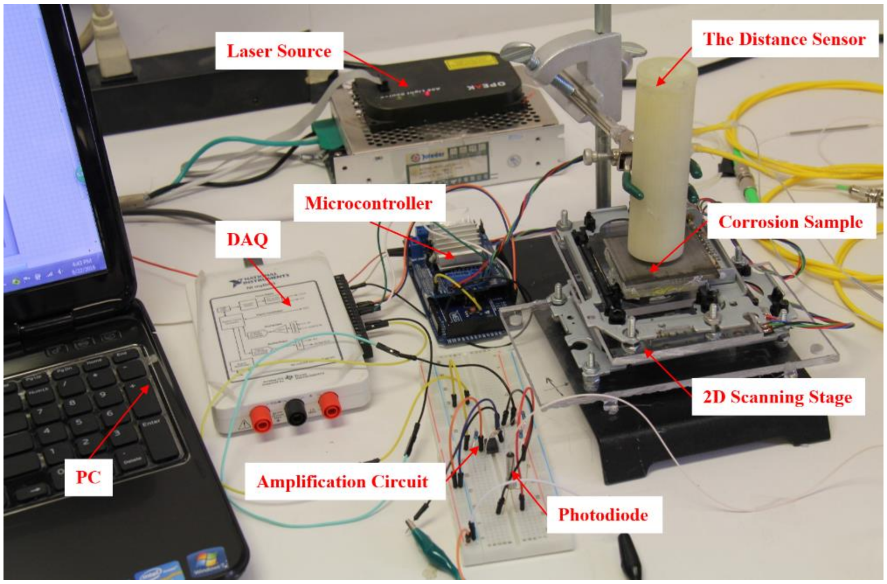

Figure 4-7 Experimental setup for scanning the corrosion samples

4.4 Results and Discussion

4.4.1 Static and Dynamic Calibration Results

Figure 4-8(a) shows the static response of the sensor to the varying distance of the steel plate for ten repeated measurements. The steel plate moving toward and away from the sensor head for ten repeated measurements. And Figure 4-8(c) shows the average signal with the 95% confidence interval, which indicate good repeatability of the sensor.

The sensor shows good response up to a distance of 5 mm and tends to be saturated when the distance between the sensor head and the metallic surface is larger than 5 mm. As can be seen, the response of the sensor is nonlinear due to combined effects of the nonlinearity of the magnetic force and the nonlinearity of fiber optic macro-bend light intensity loss. The smaller the distance between the sensor and the steel plate, the larger the slope of the voltage because of the more rapid increase of magnetic force. This means that the sensor is more sensitive and responsive at smaller distance. It should also be noted that the sensor signal does not travel along the same curve when the steel plate is moving toward and moving away from the sensor head. This phenomenon is the so-called hysteresis, which is unavoidable for sensors working on the principle of magnetic field. Apart from the magnetic hysteresis, the friction between the magnet and the ball bearing guiding cylinder may also contribute to this hysteresis issue. For the application of determining the rough geometry of the corrosion pit on a metallic surface, as demonstrated in the following contents, the accuracy is adequate. However, if more accurate determination of the corrosion pits is required, hysteresis compensation techniques should also be developed to accurately compensate the hysteresis. For now, the modeling and calibration for hysteresis compensation are beyond the scope of this study.

To correlate the voltage reading to the corresponding distance of the sensor to the metallic surface, the distance axis and voltage axis in Figure 4-8(a) were interchanged, and then the data points were fitted with curve. During the curve-fitting, the voltages of distance greater than 5 mm were neglected. In the sensing distance up to 5 mm, the data points were approximated by a linear curve, as shown in Figure 4-8(b). An inverse of the slope of the fitted curve gives the sensitivity of the sensor, which is 1.67 V/mm. The fitted curve was used to characterize the approximate shape of the corrosion pit of the corrosion sample. To suit for various applications, the sensitivity accuracy can be easily adjusted by changing the size of the magnet, the stiffness of the spring element, and the amplification of the output voltage.

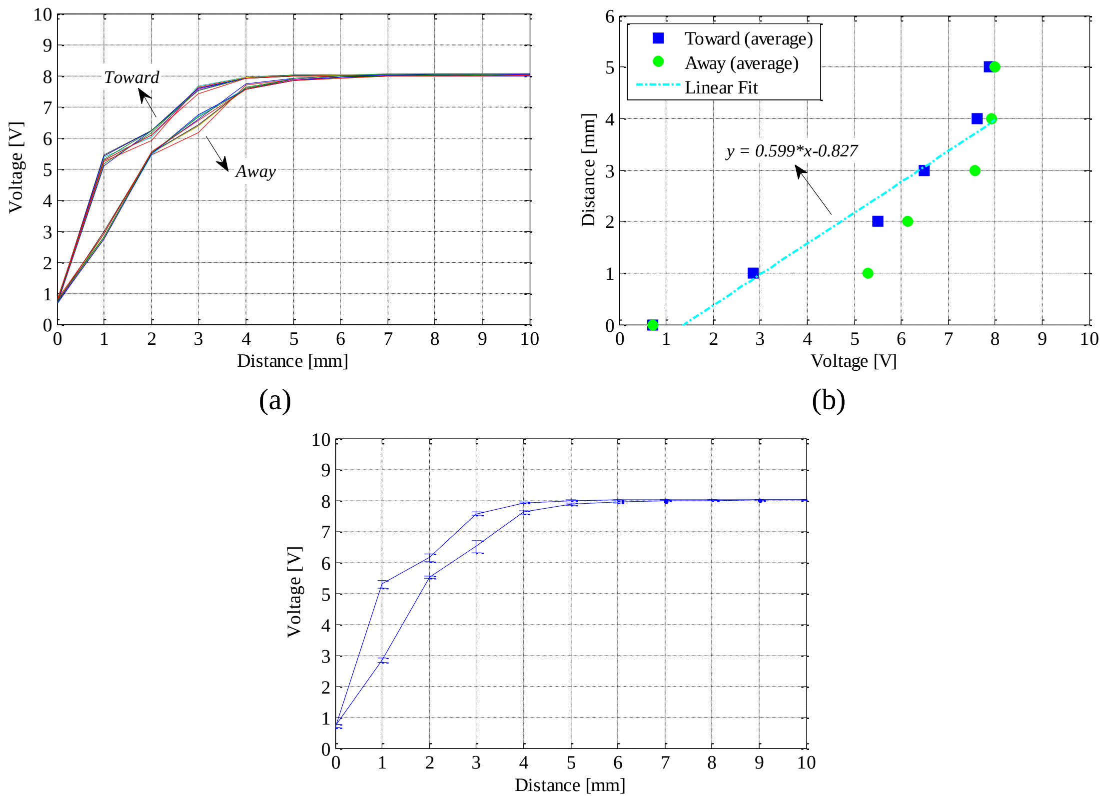

(c)

Figure 4-8 (a) Voltage versus the distance; (b) The distance as a function of voltage and the fitted curve. (c) The average signal

The envisioned application of proposed sensor will be used to scan over the metallic surface for determining and assessing any pitting corrosion. The structures requiring corrosion assessment may be large in scale, such as oil and gas pipelines, fuel storage tanks. A quick scan over the structure will be favorable. Therefore, the dynamic response of the sensor is examined, Figure 4-9 shows the dynamic response of the sensor and the comparison to the laser displacement sensor. The shape of the vibration response of the sensor is non-symmetric due to the nonlinearity of the sensing mechanism. As stated above, the corrosion is more responsive when it approaching the metallic surface while less responsive when it is further away from the metallic material. Irrespective of the nonlinearity of the sensor, the sensor is responsive to the vibration of 2 Hz, which should be well-suited for in-situ scanning of metallic structures.

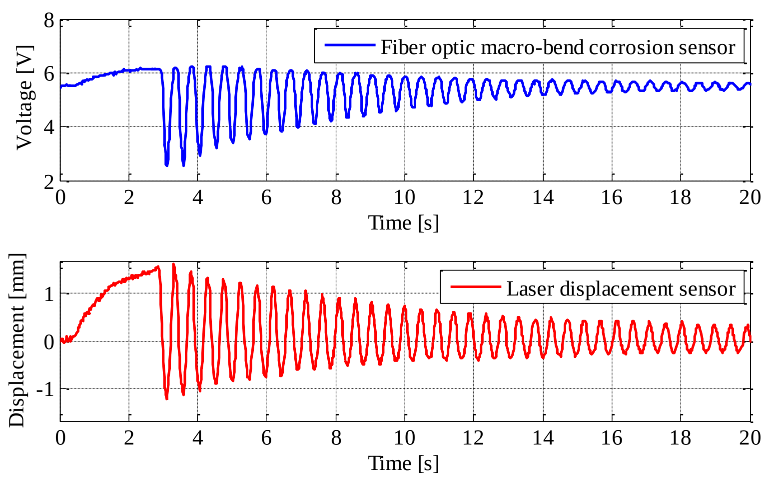

Figure 4-9 Results of dynamic response of the distance sensor (top) and comparison with the results from laser displacement sensor (bottom)

4.4.2 Scanning on Fabricated Corrosion Pit Samples

The fiber optic macro-bend distance sensor was used to detect the fabricated corrosion pits of various shapes and forms that were commonly encountered in real world situation. Figure 4-10 illustrates the scanning results of wide shallow corrosion pit and a comparison with the scan with laser displacement sensor. As can be seen, the proposed distance sensor is able present the rough shape of the corrosion pit. The voltage readings were converted to distance using the above-mentioned linear approximation. The scanning results for narrow deep and elliptical corrosion pits are shown in Figure 4-11 and Figure 4-12, respectively. The narrow deep and elliptical pits seem to be similar but possess different magnitude. The scanning results for subsurface corrosion pit is not shown since the distance sensor is not able to detect the subsurface corrosion pit. One can conclude that despite the removal of the metal at the targeted site, enough metal was still present to fully contain the magnetic field of the sensor magnet. Once the metal becomes thin enough, it may saturate quickly and not able to contain the full magnetic field, thus not activating the full pulling force of the magnet. Thus, the sensor is limited to subsurface defects that are severe enough to influence the magnetic saturation of the metal by the magnet. The limit can be designed based on the properties of the magnet.

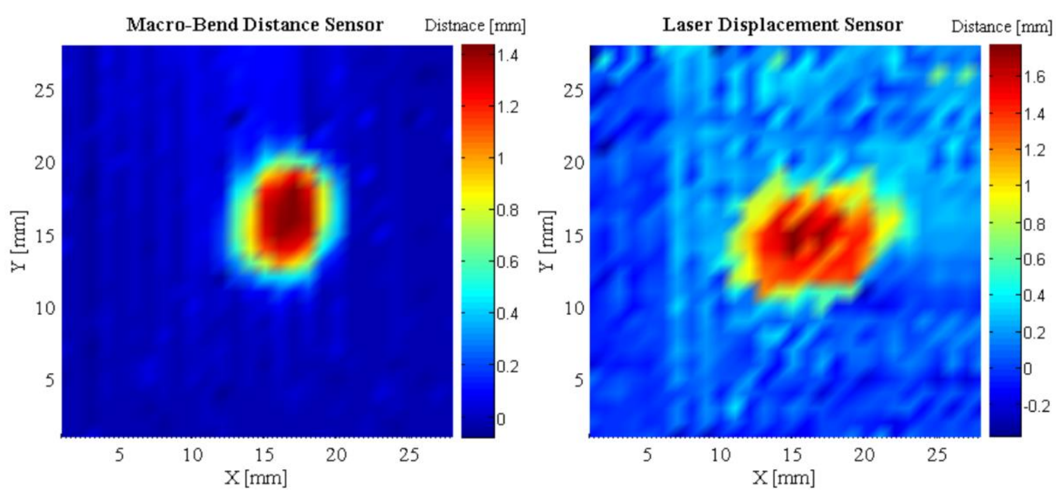

Figure 4-10 Wide shallow corrosion pit scan: macro-bend distance sensor (left) and laser displacement sensor (right)

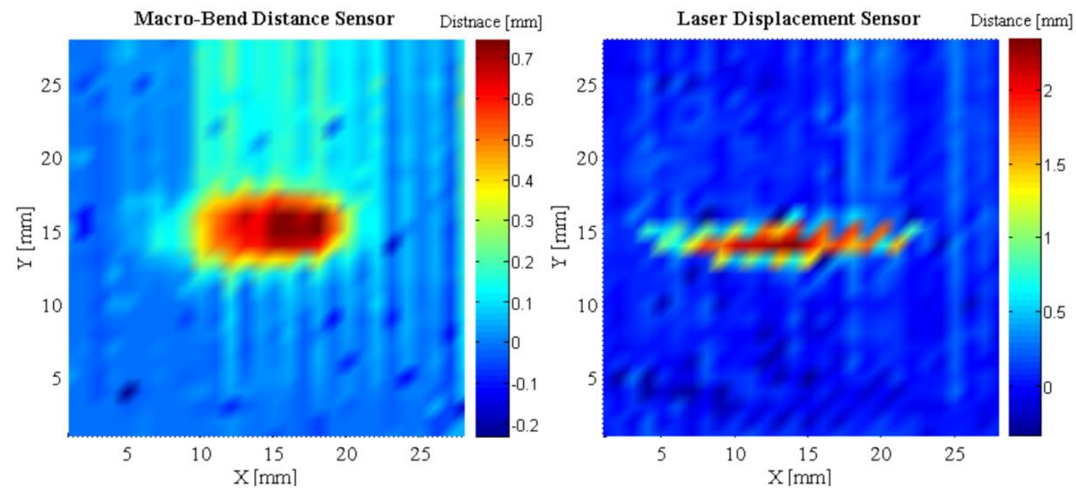

Figure 4-11 Narrow deep corrosion pit scan: macro-bend distance sensor (left) and laser displacement sensor (right)

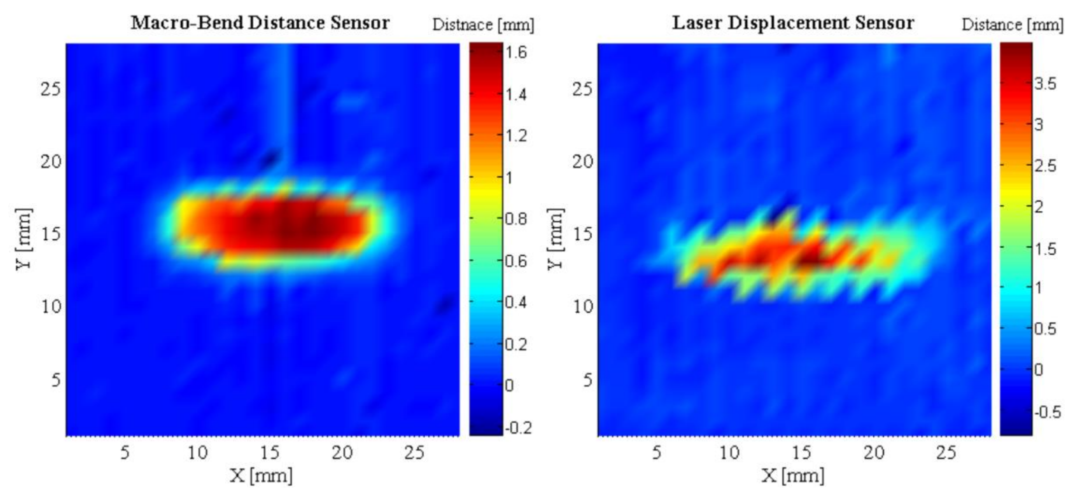

Figure 4-12 Elliptical corrosion pit scan: macro-bend distance sensor (left) and laser displacement sensor (right)

Attention should be paid to the scale of the scanning results for these three figures. It can be seen that the distance sensor predict the wide shallow pit more accurately. However, for narrow and deep pit, the distance sensor cannot clearly tell the detailed profile of the pits, especially when the size of the pit is smaller than the size of the magnet. The measurement from the proposed distance sensor is corresponding to a small region on the corrosion sample around the sensor head, but not a point in front of the sensor head as the laser displacement sensor does. Thus, the distance sensor will be less accurate when the size of the pit is smaller than the size of the magnet. One can imagine that the lines of magnetic force are spreading around a small region on the ferromagnetic surface. And owing to this phenomenon, the scanning results tend to have a smooth shapes. In order to obtain more refined shapes, smaller sensor can be designed using smaller magnets.

While the laser displacement sensor provided more precise results, the distance sensor compensates through the applicability towards situations where the laser sensor cannot function properly. For example, the proposed sensor can detect the loss of metal even when the metal is covered with opaque liquid or covered with a filling layer of debris, as long as the liquid or debris does not contain strongly ferromagnetic material. The use of optical signals also means that the sensor signal is immune to electromagnetic interference that may incapacitate other electronics based sensing methods, such as magnetic flux, eddy current, etc. The presence of another magnetic field, while not affecting the actual fiber optic cable and the properties of the optical signal, may still have an effect on the movements of the magnet in the proposed sensor. The amount of disturbance will depend on the magnitude of the intruding magnetic field. However, it is foreseen that in most applications, a magnetic field that is strong enough to noticeably affect the sensor will not be encountered. Water, hydrocarbons (e.g. petroleum), and rust, while possessing diamagnetism and are foreseen to contact and surround the sensor including, are not likely to register measurable effects on the magnetic field of the sensing magnet. Depending on the situation, the lack of need for physical contact also provides the sensor an advantage over ultrasound, which requires a firm sensor-specimen coupling. The advantage of the proposed sensor is the ability to work in opaque liquids, or in situations where gases may scatter the light of the laser sensor and prevent the laser sensor from working. Furthermore, the simple construction of the sensor head should lend to lower costs compared to most conventional sensors. The most costly component of the sensor is the fiber laser source, which can be chosen to be even more inexpensive. With a controllable light switching device, a single fiber laser source can be used for an array of sensors.

In regards to the performance, the sensor at this point will not provide the same level of accuracy as precision instruments such as the laser sensor. On the other hand, the accuracy may be improved through further engineering, such as the size and material of the magnet as well as the fiber optic bend. In cases where there is no optically occluding substance between the sensor and the structure and where the cost is not an issue, the laser sensor will provide a superior performance. In cases where light may not transmit very well, and where cost is an issue, the proposed sensor may prove beneficial. Examples of such cases where the metal loss sensor will be beneficial is the embedment of the sensor into concrete to monitor the degradation of steel reinforcement, or if it is to be incorporated into pigging for internal pipeline monitoring, where residual liquids and debris may prohibit other types of sensors.

4.5 Conclusions

In this chapter, a novel type of ferromagnetic distance sensor was proposed based on the principle of fiber optic macro-bend loss and magnetic force and it was used to measure loss of metal in metallic structures. The proposed sensor consisted of a bended optical fiber cable, a magnet and a spring. The magnet was attached to the spring and the fiber bend was threaded through the spring such that the movement of the magnet will induce a change in bending radius of the optical fiber. In this way the ferromagnetic metal loss due to corrosion reduces the magnetic force between the magnet and the metal surface, and thereby inducing a change in light intensity. The performance of the sensor was calibrated through static and dynamic calibration. The sensor is responsive up to a distance of 5 mm between the sensor head the metal surface. Hysteresis was observed which requires further study to seek for compensation techniques. The sensor was also highly responsive to a vibration of 2 Hz, enabling the quick scanning for large structures such as pipeline and storage tanks. The practicality of the sensor was examined through scanning over several fabricated corrosion samples with various pit shapes. The scanning results showed that the simulated corrosion pit area can be easily distinguished from the even metal background. If more resolution is required, the performance of the sensor can be improved through using smaller size magnets. The proposed ferromagnetic distance sensor has the advantages of simple structure, low cost, non-contact and remote sensing, which will be a promising technique in detecting undesired metal loss, such as in the field of corrosion detection and assessment.

5 Feasibility Study of Using Smart Aggregates as Embedded Acoustic Emission Sensors for Health Monitoring of Concrete Structures

5.1 Introduction

Concrete is the most widely used construction material all over the world. Deterioration of concrete structure results in human injuries and economic losses. Nondestructive evaluation of concrete structures has been an engineering challenge and popular research topic. Among various nondestructive evaluation techniques, acoustic emission (AE) has attracted increasing attentions since it is a promising tool for long-term monitoring and evaluating of damage evolution of the concrete structures. An acoustic emission sensor detects the stress waves that is generated by the rapid release of energy from a source within a structure undergoing deformation, crack initiation or propagation. The AE signals offer rich damage-related information of the host structure, which are well-suited for damage detection and assessment of concrete structures [26, 89, 90]. Conventionally, AE sensors are mounted on the surface of a structure to capture the AE signals generated from the structure. The coupling between AE sensors and the structure is achieved using a couplant such as oil or grease. However, it is difficult to maintain a stable coupling over long period so that the measurement accuracy will decrease in cases of in-situ and long-term monitoring of concrete structures. Additionally, the AE signal will dramatically attenuated as it travels through the concrete due to the high attenuation property of concrete material, which makes traditional AE technique inappropriate for health monitoring of the large-scale concrete structure. Moreover, traditional AE sensors can hardly be applied to the structures that are difficult to access, for example, the underground structures.

To avoid the disadvantages of externally mounting AE sensors onto the surface, the concept of direct embedment of the AE sensors into the structures was proposed. The method of sensor embedment provides excellent coupling between AE sensors and host materials, eliminating the measurement bias due to decoupling between the AE sensor and the host structure over time. These sensors can be installed in locations where accessibility is serious problem after the structure is built and in service. Over the last few years, some advances have been achieved in developing embedded piezoelectric sensors as acoustic emission sensors for the health monitoring of concrete structures. In 2010, Qin et al. [91] introduced a novel embedded AE sensor based on 0-3 (first and second digit represent the dimension of the piezoelectric particles and the matrix, respectively) cement-based piezoelectric composites. The sensor was fabricated by compacting mixed cement-piezoelectric powder into a thin plate patch and higher sensitivity was achieved through four point bending test of a concrete beam. Likewise in 2011, Lu et al. [92] devised a 0-3 cement-based piezoelectric composite and it was employed as embedded AE sensors in monitoring the damage process of a reinforced concrete frames subjected to seismic loading. In 2014 however, other than the 0-3 type, Qin et al. [93] investigated the practicality of the 1-3 type cement-based piezoelectric composites as embedded AE sensors. The characteristic of the broadband frequency response of the sensors was validated through concrete hydration and thermal cracking experiments. However, the fabrication procedures of these piezoelectric composite AE sensors are complicated, requiring specialized mixing ratio. Though extensive work has been done in developing the embedded AE sensors, a desirable embedded AE sensor has not yet been discovered.

Smart aggregate (SA), as a piezoceramic based embeddable transducer, is made of a thin PZT (lead zirconate titanate) patch that is protected by a concrete or marble case [94]. The smart aggregates can act as both actuators that generate high frequency stress waves and sensors that receive the waves. Most applications of SAs are focus on the transmitter-receiver configuration for structural health monitoring of concrete structures, such as early age concrete characterization [95, 96], damage detection of concrete columns [97] and crack propagation monitoring for reinforced concrete beam structure [98]. The suitability of SAs as embedded AE sensors has not been investigated. Compared to the embedded cement-based piezoelectric composites, SAs are of low cost, without the need for complicated fabrication procedures as in piezoelectric composites.

This chapter presents the feasibility study of using the smart aggregates as embedded AE sensors for structural health monitoring of concrete structures. The performance of smart aggregates are compared with traditional surface mounted AE sensors, in their ability to detect and evaluate the damage of concrete structures. The frequency response of the traditional embedded AE sensors is calibrated using the Hsu-Nielsen method. A concrete beam specimen with two embedded SAs and two surface mounted AE sensors was fabricated in the laboratory. In the experimental study, the concrete beam specimen was loaded under a three-point-bending test. The crack evolution during the loading test was monitored by using the two types of sensors and the experimental results were compared.

5.2 Embedded PZT-based Smart Aggregates

PZT is a piezoelectric material which can function as both a sensor and an actuator. As a sensor, the PZT produces a voltage when subjected to stress or strain. Conversely, as an actuator, the PZT generates stress wave when an electric field is applied. The SA is fabricated by sandwiching a PZT patch between two marble blocks with epoxy, as illustrated in Figure 5-1. The dimension of the PZT patch is 15 mm × 15 mm of thickness 0.3 mm. The SA has a diameter of 25 mm and a height of 20 mm. The SA is interfaced to the instruments via Bayonet Neill–Concelman (BNC) connector. The properties of the PZT are listed in Table 5-1. The marble protection of the SA serves two purposes. First, the structure protects the fragile PZT patch from external disturbance or water damage. Second, the structure maximizes the energy transmission between the PZT patch and the test specimen, which is also known as acoustic impedance matching [98].

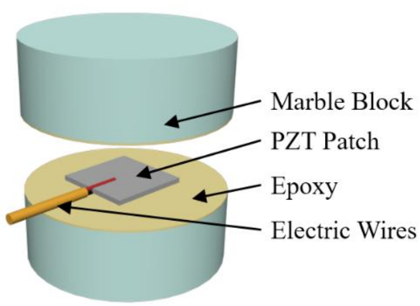

Figure 5-1 Illustration and photo of the smart aggregate

Table 5-1 Typical properties of the PZT patch

Property (unit)	Magnitude
Young's Modulus (GPa)	46
Density (10^3 kg m^{-3})	7.45
d_{31}, d_{32} (pC N^{-1})	-186
d_{33}(pC N^{-1})	670
d_{15} (pC N^{-1})	660

Since SAs have the similar size as aggregates in concrete mix, it can provide excellent embeddability and compatibility when using as an embeddable sensor. The nondestructive evaluation of concrete structure will be enhanced when the SAs are incorporated within the structure. In such a case the structure becomes an integrated smart system which can perform both AE sensing and active-sensing based health monitoring (e.g. transmitter-receiver configuration and impedance approach) of the concrete structures.

5.3 Experimental Setup

To study the suitability of the smart aggregates as embedded AE sensors, a plain concrete beam was constructed with pre-embedded SAs in the laboratory. The concrete has a cross-section of 100 mm × 100 mm and a length of 400 mm, as shown in Figure 5-2. The expected compressive strength of the concrete is 27 MPa after a curing duration of 28 days. Two SAs were used, located at the left and right quarter points of the longitudinal axis of the concrete beam, respectively, as shown in Figure 5-2. As for comparison, two AE sensors were mounted on the front surface of the concrete beam which share the same cross-sections with the SAs. The AE sensors used were wideband sensors (Physical Acoustic Corporation (PAC)) which have very good frequency response over the range of 100 kHz to 900 kHz. The AE sensors were coupled to the concrete surface using brown grease and tightly attached using hot glue. The left side of the SA and AE sensor are labeled as SA-1 and AE-1, and the right side of the two sensors are labeled as SA-2 and AE-2.

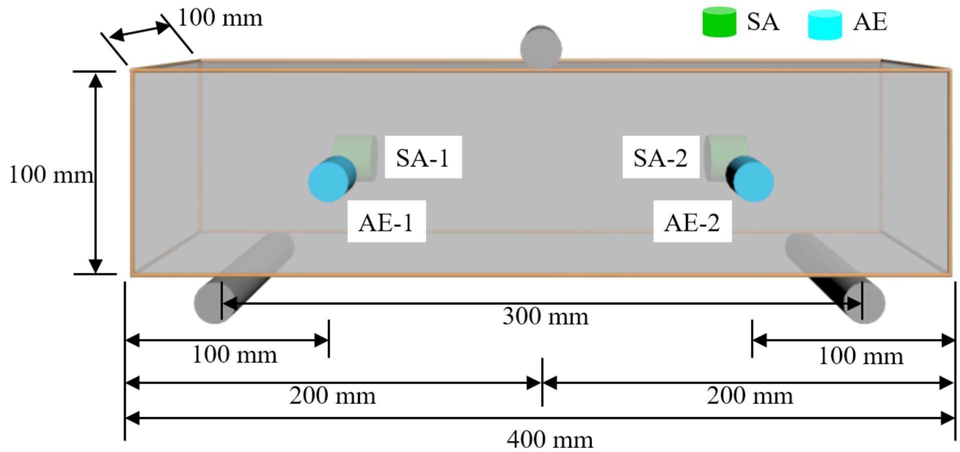

Figure 5-2 Dimensions of the concrete beam with embedded SAs and surface mounted AE sensors

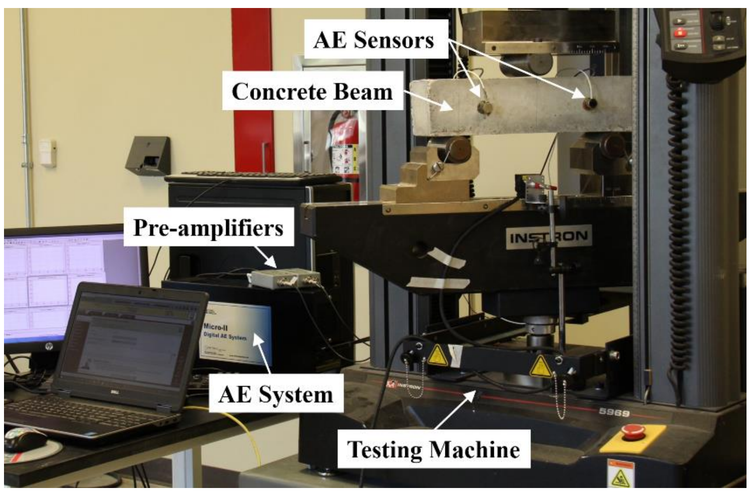

Figure 5-3 AE system setup and three-point-bending test

Three-point-bending test was adopted to induce cracking damage to the concrete specimen. The support conditions are shown in Figure 5-2. The upper load bar was centered between the two supports. The distance between the two supports were 300 mm. Figure 5-3 shows the three-point-bending test setup using an INSTRON 5969 testing machine with 50 kN capacity. The testing machine was set at displacement control mode at a rate of 0.05 mm/min. The load-displacement relationship at the mid-span of the beam was automatically registered by the testing machine. The machine will automatically stop after a drop of 40% of the maximum load to ensure safe operation. The AE data acquisition system used is Micro-II Digital AE System from PAC. Both the SAs and the AE sensors are connected to pre-amplifiers before feeding to the AE system. The sampling frequency for the recording AE waveforms was 5 MHz. The threshold level was set at 40 dB, which was calibrated using a pencil lead break test. The threshold was sensitive enough to capture significant AE signals while able to reject noise from the testing environment. The signals were amplified with 40 dB gain by the pre-amplifiers. The AE waveforms and parameters, such as hits, amplitude, counts and energy were recorded on the computer, and can be exported as text files for further processing.

Prior to the three-point-bending test, the frequency response of the SAs was examined using Hsu-Nielsen method. The Hsu-Nielsen source was generated by breaking a 0.5 mm pencil lead against the concrete specimen [99]. The pencil lead break source is a flat and broadband acoustic source which is very suitable for frequency response calibration of AE sensors. The pencil lead break locations are along the longitudinal center line on the top surface, from left end to the right end with a spacing of 50 mm. There are 9 locations in total and the test repeated for three times.

5.4 Results and Discussion

5.4.1 Frequency Response of Smart Aggregate

The amplitude of the sensors along the center line on the top surface at different pencil lead break locations was plotted in Figure 5-4. As can be seen, all of their amplitudes can reach around 80 dB, which is a typical value for a pencil lead break acoustic source. From sensitivity point of view, the SAs share the same sensitivity as the surface mounted traditional AE sensors. Normally, the sensitivity of the SA is directional, which means that the SA receives stronger signals when a wave hits the SAs along its axial direction and weaker signals when a wave is received from radial direction of the SA. Note that at location 100 mm for SA-1 and 300 mm for SA-2, these pencil lead break locations are along the radial planes of SA-1 and SA-2 respectively, as shown in Figure 5-2. At these locations, the AE sources reach the SAs from radial direction, which should have the lowest sensitivity since the PZT patch is under compressive mode. From Figure 5-4, no significant signal attenuation along the radial direction can be found. These experimental verification shows that SAs can be good candidates to function as an AE sensor. Directionality of the SA can be negligible in our study.

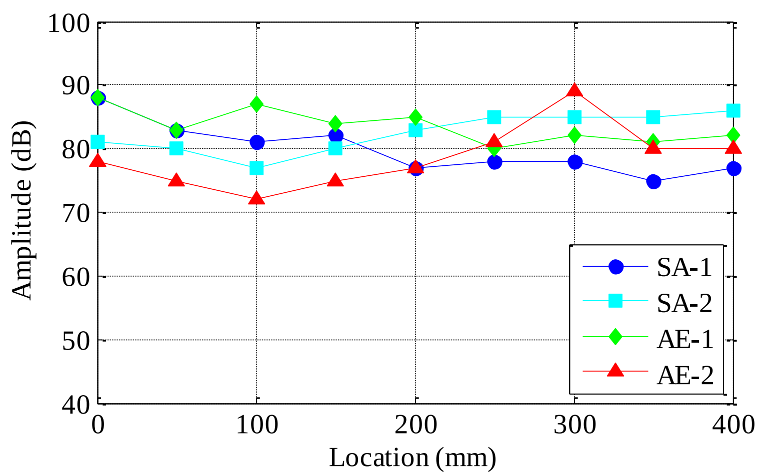

Figure 5-4 Amplitude plot of the sensors at different location

Figure 5-5 shows the response of the SAs and the traditional AE sensors due to pencil lead break tests, including time domain and frequency domain. It is clearly shown in the figures that the frequency response of SAs tend to show higher magnitude in low frequency band, which ranges from 20 kHz to about 200 kHz. For the traditional AE sensors, their frequency response tend to peak in frequency bands from 20 kHz to 50 kHz and around 100 kHz.

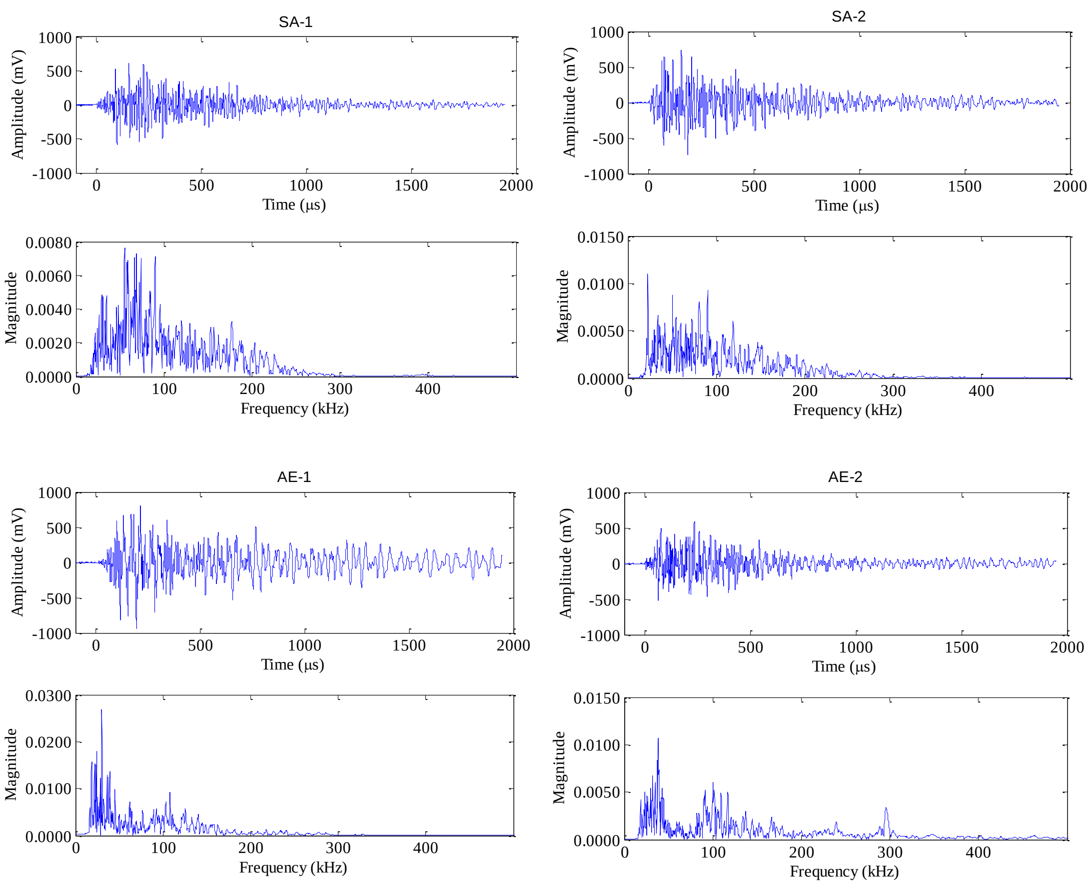

Figure 5-5 Frequency response of the SAs and the traditional AE sensors due to pencil lead break

5.4.2 Results of the Concrete Beam Test

Figure 5-6 shows the load curve and the AE activity evolution. When the load was low, say less than 2 kN, very limited AE events were detected by both SAs and AE sensors. As the applied load increased, the concrete beam began to damage in form of micro-cracking within the structure. The progression of the micro-cracking damage of the concrete beam was indicated by a constant evolution of AE hits before the ultimate failure of the concrete beam. As the concrete beam failed, marked by a sudden drop of load capacity and macro-cracking on the surface, a sudden increase of the AE hits was detected by all the sensors, as shown in Figure 5-6. As can be seen, the developing trend of the AE events recorded by these four sensors follow the same pattern. All sensors except AE-1, recorded about 1000 AE events. The reason that AE-1 registered more AE events maybe relate to a tighter coupling condition during the coupling process as compared to AE-2 sensor.

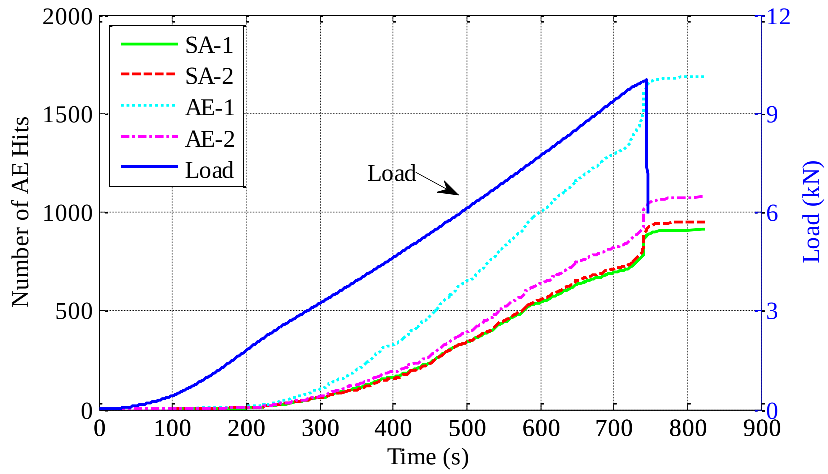

Figure 5-6 Load curve and accumulated AE hits plot

AE parameters, such as amplitude, counts, energy, duration and rise time in time domain and peak frequency and average frequency in frequency domain, provide useful information for the source identification and determining the severity of the structure. During the process of the deterioration of the concrete structure, types of cracks (micro-cracks and macro-cracks) are closely related to the AE amplitude distribution. The micro-cracking usually generates a large amount of events of small amplitude, while macro-cracking generates fewer events but of larger amplitude. The amplitude plots of AE events recorded by these four sensors are shown in Figure 5-7. As can be seen, most of the events show low amplitude across the time frame of the test, which are related to the initiation and propagation of micro-cracks. When the concrete approaches the ultimate failure state (around 720 s), strong and dense events were detected, which were generated from the macro-cracking of the concrete specimen. It is evident that the amplitude plots of SAs share the similar trend with that of AE sensors. Therefore, the feasibility of SAs as embedded AE sensors were further validated. The counts plots are shown in Figure 5-8, which also present the same indication as amplitude plots. There are strong signals at the moment when the concrete totally failed. All other AE parameters in time domain also show the same indication since these parameters as closely correlated to each other.

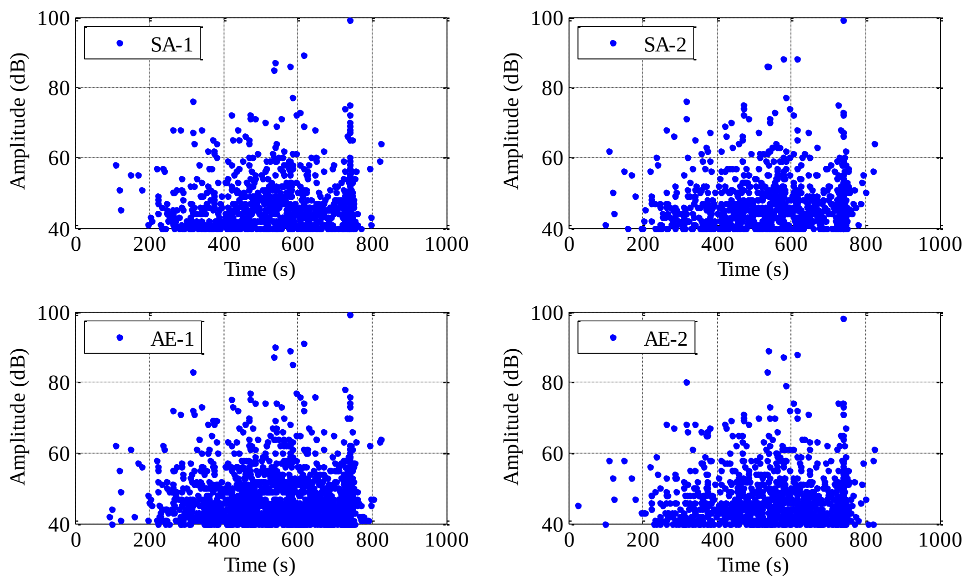

Figure 5-7 Amplitude plots of AE signals from the four AE sensors

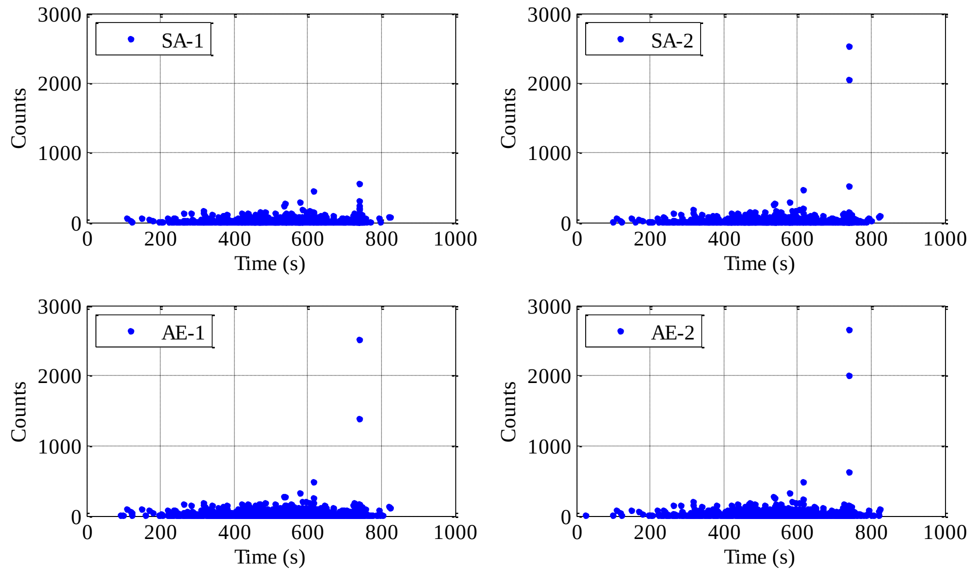

Figure 5-8 Counts plots of AE signals from the four AE sensors

From sensitivity point of view, the embedded SAs have not shown superiority over the conventional surface mounted AE sensors since the dimension of concrete sample is pretty small. The location of the SAs and AE sensors are very close to each other in this case. It should be noted that the high-frequency acoustic emission waves are rapidly attenuated in concrete structures. The attenuation rate of the AE wave propagation in concrete structures can go up to 29 dB/m [100]. The attenuation of AE signals will significantly affect the value of AE signal parameters such as amplitude, duration and energy, which are the most important parameters in evaluating the damage severity of the structure. The application of conventional surface mounted AE sensors usually requires stringent sensor placement scheme for each individual tested structure to ensure the adequate coverage of the structure under test [101]. However, as a type of embedded AE sensor, the SAs can be easily embedded at the location of interest that are more prone to be damaged. In this way the SAs are more sensitive to detect the damage of a structure, and more information will be registered in evaluating the integrity of the tested structures.

Another important issue need to point out is the effect of temperature on the AE properties of the structure since such issue will be faced in certain applications. This is not an issue in most environments, but may be important in very hot or very cold climates [102], and in some engineering structures affected by high temperature in gas explosion, nuclear reactor shielding layer, tunnel and mine fire, etc [103]. In low or in high temperature, the properties of the concrete structure are becoming complicated and the physical and mechanical properties of the concrete will change with temperature, so does the AE characteristics of the structure. Geng et al. detailed the property changes of concrete structure at different temperature [103]. According to their findings on the effects of temperature on the strength and real-time acoustic emission signals of concrete, the number of AE events were less at high temperature than that at lower temperature. The concrete at low temperature tends to be more compact and has higher bonding strength, and thus will release more energy in the course of loading. As a result, more AE events will be generated. In contrast, when the concrete is treated in high temperature, the concrete become loose. Under the effect of loading, the concrete will release less energy and less AE events. The properties of the AE waveforms and the propagation of the waves will also be modified due to the physical and mechanical properties changes of the concrete. These properties include the AE wave velocity, amplitude, resonant frequency and so forth. In general, the effect of temperature on the AE characteristics of concrete structures is a complicated problem and requires in-depth study.

5.5 Conclusions

In the present study, the feasibility of using SAs as embedded AE sensors for damage characterization of concrete structures has been experimentally investigated. A pre-experimental verification using a standard pencil lead break test was conducted to compare the frequency response of SAs and traditional AE sensors. Results showed that the SAs tend to be more sensitive in low frequency band, ranging from 20 kHz to 200 kHz. Further, in order to study the functionality of SAs of being used as AE sensors in concrete health monitoring, a plain concrete beam with two embedded SAs and two surface mounted AE sensors was investigated under a three-point-bending test. The AE parameters that were used to describe the damage progression of the tested concrete structures, such as hits, amplitude and counts, from both the SAs and traditional AE sensors showed similar characteristics. The results confirmed that the feasibility of using SAs as embedded AE sensors for the structural health monitoring of concrete structures. The use of SAs as embedded AE sensors possesses several advantages. Firstly, the structure and fabrication process of SAs are simple and low cost. Secondly, the embedded SAs are capable of serving in-situ and long-term monitoring of concrete structures, without additional manual check for coupling between the sensor and the structure. Finally, the SAs can be pre-embedded into a structure, which make them more suitable for monitoring of large-scale structures and structures with accessibility issue. While the results from laboratory tests are encouraging, the efficacy of the SAs as embedded AE sensors have never been tested for practical applications. In the future, SAs will be deployed in large-scale concrete structures, and further feasibility study on practical applications of using SAs as embedded AE sensors will be conducted.

6 Acoustic Emission Monitoring and Finite Element Analysis of Debonding in Fiber-Reinforced Polymer Rebar Reinforced Concrete

6.1 Introduction

Polymer composite materials were gradually adopted in civil engineering applications in various forms including rebars for reinforced concrete structures, sheets for flexural and shear strengthening, and sheets to wrap concrete columns and bridge piers to increase the confinement [104-107]. The application of fiber reinforced polymers (FRP) rebars as an alternative to the steel reinforcements has gained increasing interest over the last few years. The FRP composite reinforcing bars exhibit several advantages over their steel counterpart, such as light weight, high tensile strength, high corrosion resistance, good fatigue endurance and non-electromagnetic. Therefore, FRP rebars can be advantageously utilized as reinforcing element for concrete structures in highly corrosive environments such as seawalls, bridge decks and pavements exposed to deicing salts. A significant amount of in-situ applications of the FRP rebars have been accomplished all over the world and the market with a high variety of reinforcement continues growing.

The structural performance of the reinforced concrete members depends on the composition of the concrete, the reinforcement members, and the bond between these two components. The interfacial bonding between the FRP rebars and the concrete plays an important role in achieving the composite behavior and increasing the strength. The primary mechanisms of the interfacial bonding comes from three contributions, including chemical adhesion, mechanical interlocking and friction resistance [108]. Each component contributes to the overall bond strength in varying degrees in such a way that the chemical adhesion is the main contributor to the interfacial bond strength while the other two mechanisms contribute to the pullout strength under slipping of the rebars. The interfacial bonding will deteriorate due to environmental and load-related issues, leading to debonding between the concrete and the reinforcement. Interfacial debonding could weaken the structural integrity, reduce tensile resistance of the structure, and make the structure vulnerable to more damage. It is therefore essential to develop an appropriate structural health monitoring (SHM) scheme towards the detection of interfacial bond failure between FRP rebars and concrete.

The acoustic emission (AE) technique is a non-destructive evaluation technique which is a promising method for the investigation of local damage of structures. The technique utilizes piezoelectric transducers mounted on or embedded in the structure to detect the transient elastic waves that are rapidly released by the growth of damage. The AE technique offers rich damage-related information in real time and thus can be used to detect, locate and characterize damage within a structure [26, 109-113]. One advantage of AE is that it capable of classifying mechanisms of the damage occurring within a structure through the interrogation and analysis of the recorded waveforms. The parameters that describe these waveforms, such as event hits, amplitude, and frequency content could suggest the nature of the event or the damage which produced them. These features make AE a powerful tool for structural health monitoring and damage characterization of concrete structures. Behnia et al. [114] comprehensively reviewed the application of AE technique for the structural health monitoring and condition assessment of concrete structures, especially concentrated on the AE parameters that used to describe damage evolution. Kawasaki et al. [115] used the AE technique to study the development of fractures in reinforced concrete members due to reinforcement corrosion. Gallego et al. [116] investigated the steel-to-concrete bond phenomenon with the aid of AE under the pullout tests. It has been shown that the transition points of the four stages that describing interfacial bonding agreed well with the measurement from AE system.

Nevertheless, the AE technique has never been used to characterize the interfacial debonding behavior of FPR rebar reinforcement concrete structures. This chapter presents the experimental investigation of using AE technique to characterize interfacial debonding failure in a FRP rebar reinforced concrete structure during pullout experiments. Three FRP rebar reinforced concrete specimens were prepared in laboratory and debonding experiments were conducted through pullout tests. The debonding behavior of the specimen was monitored in real time using a sophisticated AE system. In addition, a numerical approach, such as finite element analysis (FEA), was adopted to model the interfacial debonding behavior between FRP rebar and the concrete. Subsequently, the stress distribution during the reinforcement pullout was addressed.

6.2 Experimental Setup

6.2.1 Materials

To investigate the applicability of AE technique for characterizing debonding behavior and damage evolution of FRP rebar reinforced concrete subjected to pullout test, FRP rebar reinforced concrete specimens were prepared. The FRP rebar used was carbon fiber reinforced polymer (CFRP) due to its high strength property. For the experimental determination of the debonding behavior between reinforcement and concrete, pullout specimens with reinforcement embedded in the middle is usually used. Figure 6-1 shows the geometry of the specimen.

The CFRP rebar had a length of 600 mm and a nominal diameter of 10 mm with helical wrapping on its surface. The CFRP rebar was embedded in a 150 mm × 150 mm × 150 mm concrete cube and the bonding length was 50 mm. At the loading end of the specimen, bonding between rebar and concrete was prevented by inserting a 100 mm long PVC tube in order to minimize stress concentration at the loading end. A counteracting concrete block with 180 mm embedment length was casted on the other end of the rebar to facilitate the pullout loading experiment. A direct gripping on the CFRP rebar would induce breakage of the CFRP rebar due to the undesired imbalanced loading and poor shear resistance of CFRP rebar in the transverse direction. Therefore a counteracting concrete block with longer bonding length was used so that the fixtures were acting on the concrete blocks rather than directly on the CFRP rebar.

Concrete Mix 1101 (QUIKRETE) used for preparing the specimens (with 27 MPa compression strength at 28 days curing). The concrete mix contains a blend of Portland cement, sand and gravel, which is a product used for general purpose construction. The product meets the ASTM C387 compressive strength requirement. The concrete mix was thoroughly mixed using a mixer after adding adequate amount of water. The concrete mix was then poured into a wooden mold with CFRP rebar embedded in the middle and the specimens were compacted with a vibrating table. Finally, the specimens were cured for

7 days before the pullout tests. Three identical pullout specimens were prepared to check the reliability of the test setup and the reproducibility of the tests.

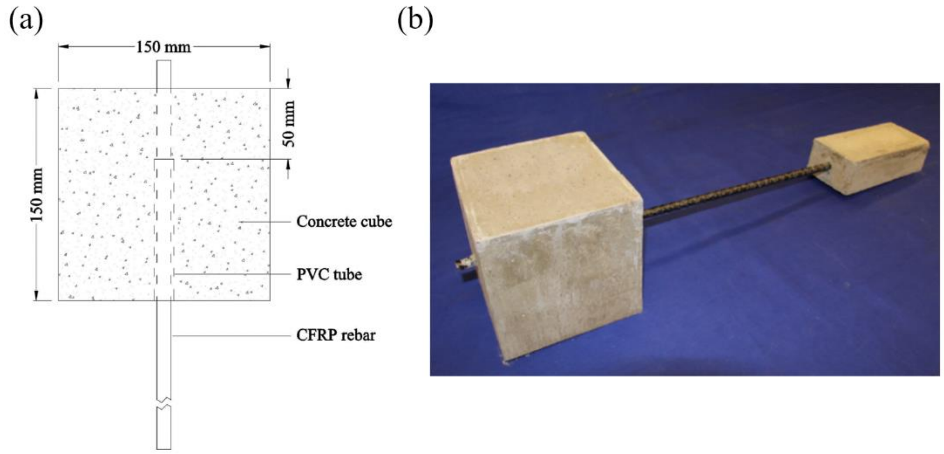

Figure 6-1 CFRP rebar reinforced concrete pullout specimen (a) sketch and (b) photo

6.2.2 Pullout Test Setup and Acoustic Emission Monitoring

The pullout test setup is shown in Figure 6-2. The tests were performed using INSTRON 4482 universal testing machine with a capacity of 100 kN. Two dedicated loading frames were manufactured to transfer the reaction from the specimen to the machine. The load was applied to the rebar with the displacement control mode at a rate of 1 mm/min. Displacement control was selected to acquire the post-peak behavior. The load and the displacement information were measured with the electronic load cell of the testing machine. The displacement measured from the testing machine includes the slippage of the reinforcement and the elastic elongation of the reinforcement under loading. The AE signals was acquired by one wideband AE sensor (Physical Acoustic Corp., (PAC)) which has a relative flat frequency response over the range of 100 kHz to 900 kHz. To ensure good acoustic coupling between the specimen and the AE sensor, brown grease was used as couplant. Then, the AE sensor was firmly attached to the surface of the specimen using hot glue. The sensitivity of the AE sensor and the parameters for the AE system were checked using pencil lead break tests. The debonding behavior of the specimen was monitored using an AE system (Micro-II Digital AE System, PAC). The sampling frequency for the recording waveforms was 5 MHz. The threshold level was set at 50 dB which was sensitive enough to capture significant AE signals while rejecting noise from the testing environment. The signals were amplified with 40 dB gain by a pre-amplifier. The AE waveforms and parameters, such as hits, counts, energy and duration were recorded on the computer, and can be exported as text files for further processing.

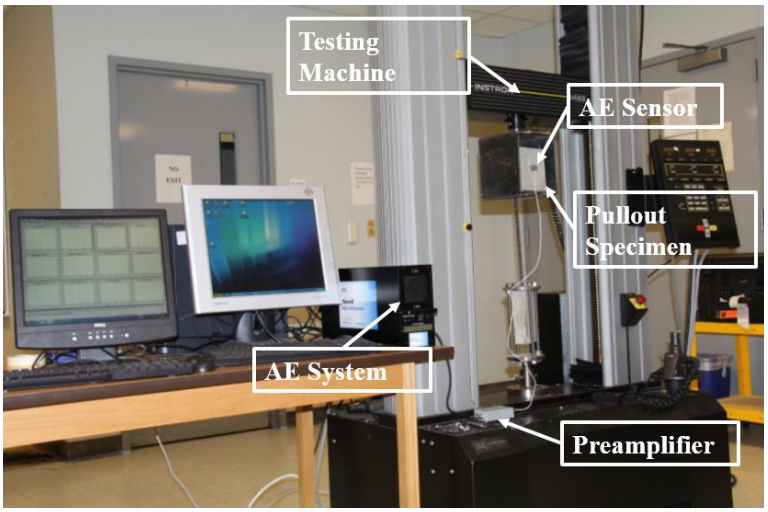

Figure 6-2 Pullout test setup and AE instrumentation

6.3 Results and Discussions

6.3.1 Debonding Characteristics

The specimens failed in pull-through mode. No split cracking occurred on the concrete cubes since the dimension and the embedment length of the reinforcement were relatively small as compared to the dimensions of the concrete blocks. The concrete block provided adequate confinement to the rebar. The specimens were split after the pullout tests to reveal the interface and examine the bond failure characteristics. The characteristics of the specimens after the pullout tests are shown in Figure 6-3. It can be seen that the helical wrapping layer of fiber was peeled off completely. This helical layer was broken down into pieces attached to the concrete at the location of the embedment. In our case, the ultimate bond strength of the specimen was governed by the bonding strength of the helical wrapping layer and the shear strength of the concrete surrounding the reinforcement.

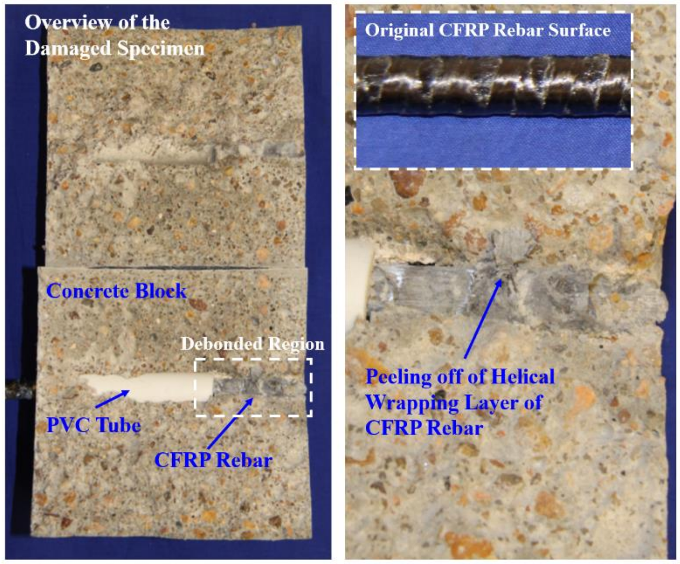

Figure 6-3 Debonding characteristics of the specimen: overview (left) and detailed view (right)

6.3.2 Acoustic Emission Response

The AE response gives an immediate indication of the behavior of a material under stress, closely connected with strength, damage and failure. The AE activity for all the three specimens showed similar patterns, only the AE results from one of the specimens are presented. The cumulative number of AE hits is plotted along with the load-displacement curve in Figure 6-4. From the load-displacement perspective, the behavior of the load-displacement relationship is characterized by an initial linear increase in bond strength, followed by a noticeable slippage (around a displacement of 7.5 mm) before the maximum bond strength is reached. Up to the noticeable slippage, bond strength can be attributed to mechanical interlocking, chemical adhesion and friction between the rebar and concrete. Once the adhesive bond fails completely, which occurred at a displacement of 7.5mm, the bond strength is made up of mechanical interlocking and friction. The bond strength keeps increasing after the loss of chemical bond, which shares the same phenomenon with the Baena's results on helical wrapping GFRP rebars [117]. In his work, he found that larger bearing resistance from interlocking mechanism develops after the point where chemical adhesion is lost and thereafter the bond strength increases. As the reinforcement being pulled further away, the interlocking mechanism fails with only the friction left. It can be seen from Figure 6-4 that the load drops to a relative constant value after a displacement of 14 mm, indicating the remaining bond strength that coming from friction force.

The AE hits is defined as the number of AE signals measured by the AE sensor on a channel. The AE hits number is one of the critical parameters to observe changes in mechanical properties and AE activities during debonding damage process. The AE hits number shown in Figure 6-4 illustrates an interesting characteristic during the pullout test of the specimen. The rate of the AE hits appears to increase just prior to the noticeable slippage of the reinforcement, which occurred at the displacement of around 7.5 mm. The change in AE hits rate likely indicates microstructural change taking place. Landis [118] also observed the same phenomenon in relating micro-macro fracture relationships in concrete using AE. As mentioned above, this is the moment when mechanical interlocking taking up most of the load. This change is most likely associated to the breakage of the helical wrapping layer of the CFRP rebar since these wrapping layer provides the interlocking force between the rebar and the concrete. In general, the AE hits is well in accordance with the debonding evolution of the specimen.

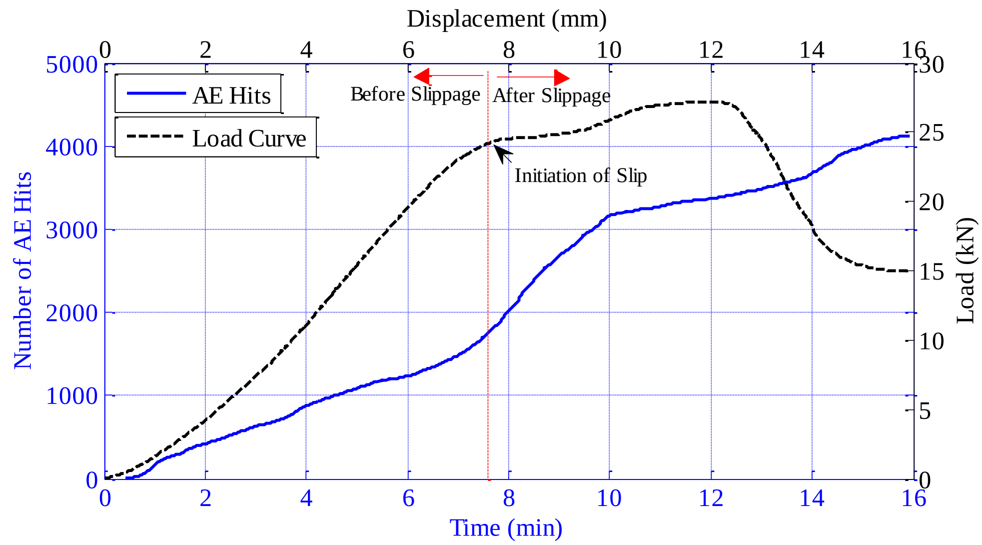

Figure 6-4 Cumulative number of AE events and load curve

Figure 6-5 shows the amplitude scatter plot of the AE signals and each dot indicates the amplitude of the corresponding AE signal. The AE signals were generated right after the load pullout load applied on the specimen. These AE signals are related to the microscopic fractures of the specimen. It can be clearly seen that three clusters of strong signals were generated at the transition phase of the bond mechanism, which are highlighted in dashed red square in the figure. The first cluster of strong signals indicates the initiation of losing chemical adhesion. The second cluster of strong signals corresponds to the moment when the total loss of chemical adhesion and mechanical interlocking taking up most of the load. And the third cluster are associated with the total loss of interlocking mechanism and the bond is only come from friction strength. Other descriptive parameters in time domain, like energy, counts and rise time, are also able to characterize the debonding evolution. They are not shown since these time domain parameters are highly correlated to each other and they share similar pattern.

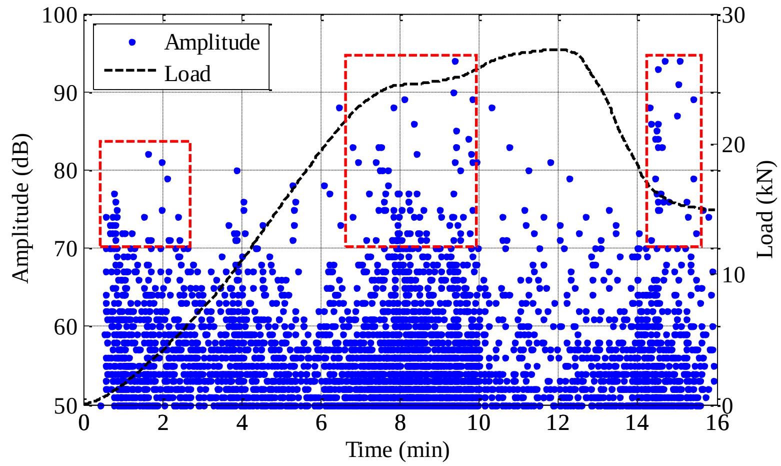

Figure 6-5 Amplitude scatter plot of the AE signals

Peak frequency is the frequency with the maximum magnitude as determined by a fast Fourier transform (FFT) of the recorded waveform. The peak frequency can serve as a good indicator of different AE sources arising from different types of fracture mechanisms [119-121]. Other indicators in frequency domain, such as average frequency and central frequency share the same properties. Figure 6-6 shows the peak frequency content of the AE signals. As can be seen, the peak frequencies can be divided into three major bands; the first band is lower than 150 kHz, the second band is between 200 kHz and 300 kHz and the third band is higher than 350 kHz. The frequencies lower than 150 kHz generated throughout the pullout test is most likely related to the microfracture of the concrete and possibly the matrix cracking of the CFPR rebar. Based on the peak frequency analysis by Gutkin [120] on CFRP composite material, frequency range for matrix cracking is below 100 kHz, fiber/matrix debonding is between 200 kHz and 300 kHz and fiber breakage is above 400 kHz. In our case, the second frequency band (between 200 kHz and 300 kHz) and the third frequency band (above 350 kHz) show up right from the moment of the noticeable slippage (a displacement of 7.5 mm). From this moment microstructural damage of the CFRP rebar is initiated and this explains the sudden increase in AE hits rate that discussed above. Therefore, frequencies between 200 kHz and 300 kHz are related to fiber/matrix debonding within the CFRP rebar and frequencies higher than 350 kHz are associated with fiber breakage within the CFRP rebar. The physical outcome of these microstructural damage is the peeling off of the helical layer of the CFRP rebar. Such division agrees well with the results obtained by Gutkin [120] and the aforementioned debonding characteristics.

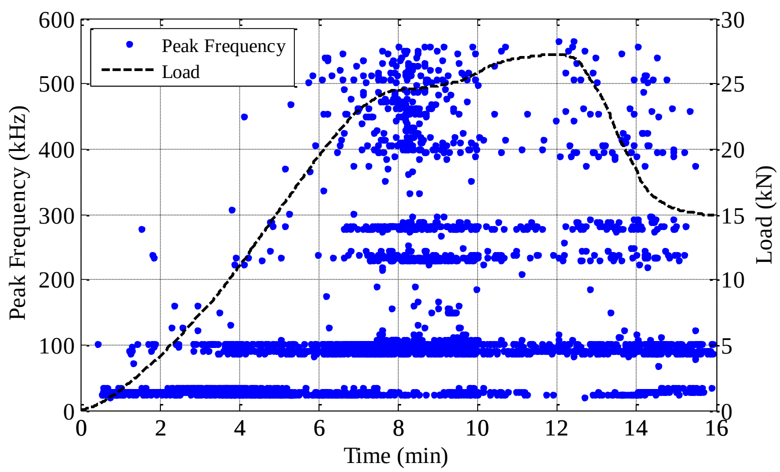

Figure 6-6 Peak frequency content of the AE signals

6.4 Finite Element Analysis

6.4.1 Details of Finite Element Analysis

Finite element analysis is a numerical method widely applied to model the nonlinear behavior of the concrete structures [122]. It was employed to analyze the bond performance between reinforcing FRP bar and concrete in a 2-dimensional manner [123]. In the present case, FEA was used to analyze the bond performance of the aforementioned pullout specimen in a 3-dimensional manner and also to take the nonlinearity of concrete into account. To this end, a finite element model was established using a general purpose finite element code ANSYS. The concrete was modeled with the dedicated concrete element SOLID65 and the CFRP rebar was modeled using the SOLID45 element. To account for the nonlinear bonding behavior between CFRP rebar and concrete, the nonlinear spring element COMBIN39 was adopted to simulate the bonding between rebar and concrete. The model was generated according to the dimensions used in the experimental setup. Only 1/4 of the model was required since we can take advantage of the two planes of symmetry, to reduce the number of elements and save computational time, as shown in Figure 6-7(a). The material properties for concrete and CFRP rebar are listed in Table 6-1. For concrete modeling, additional properties need to be defined to account for cracking and nonlinearity, namely the shear transfer coefficient β and compressive uniaxial stress-strain relationship. The open crack shear transfer coefficient was set at 0.35 and close crack shear transfer coefficient was set at 0.85. The compressive stress-strain curve of concrete was defined according to Hognestad’s model [124]. For CFRP rebar modeling, linear isotropic material property was assumed. For the nonlinear bonding simulation, the load-displacement acquired from pullout test was used as the input data of the nonlinear spring element CONBIN39.

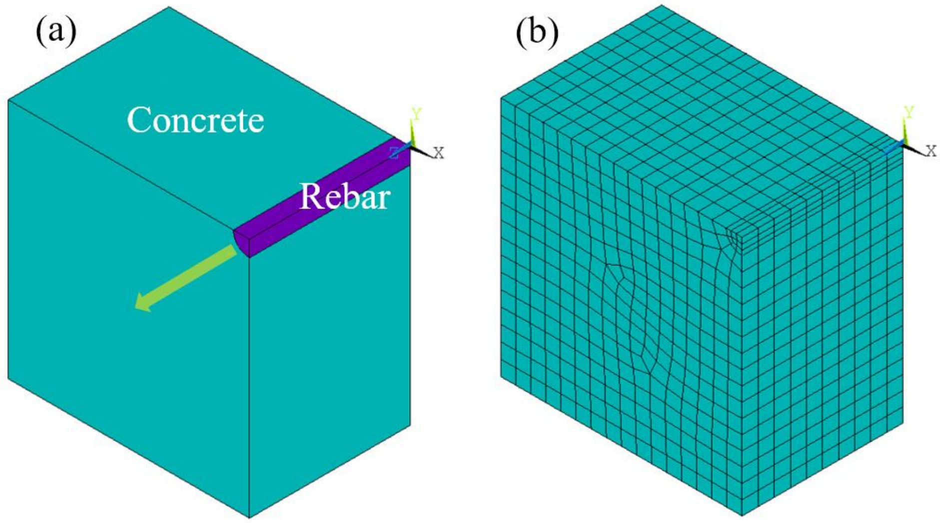

Figure 6-7 (a) Model geometry and (b) finite element mesh

Table 6-1 Material properties used for simulation

Material	Modulus of elasticity (MPa)	Poison's ratio	f_{c28} (MPa)	f_{t28} (MPa)	f_u (MPa)
Concrete	30,000	0.2	27	3	-
CFRP Rebar	115,000	0.3	-	-	1500

During the modeling of the pullout specimen, the concrete and rebar elements were built separately, with their interface having the same mesh so that the nodes of these two materials coincide at the interface. These nodes were selected to create the bonding element. Figure 6-7(b) shows the finite element mesh. After the finite element model was established, a displacement of 16 mm was imposed on the CFRP rebar to simulate the pullout of the reinforcement.

6.4.2 *Results of Finite Element Analysis*

The displacement field in Z direction, which is along the CFRP reinforcement pullout direction, is plotted in Figure 6-8(a). As can be seen, the loading end has the largest displacement and the displacement decreases toward the free end the rebar. Figure 6-8(b) shows the stress field in Z direction. Similar to the displacement field, the loading of the rebar has the largest stress and the stress decreases along the embedded length. Figure 6-8(c) and Figure 6-8(d) illustrate the shear stress field in XZ plane and YZ plane, respectively. They share the same characteristics but in a different direction. The contour results at different displacement levels shared similar pattern but with different stress levels. Chang et al. systematically studied the pullout behaviors of FRP rebar reinforced concrete at different stages [123]. It is evident that the reinforcement-concrete interface near the loading end shows the largest shear stress and propagates to the free end. The debonding initiated at the loading end of the reinforcement and propagated to the free end. The shear stress field is more related to the interfacial debonding between concrete and reinforcement. It can be observed that the shear stress was more concentrated at the interface between concrete and the reinforcement. The FEA results agree well with the experiments. According to experiments, the helical wrapping layer has the least load bearing capacity. The debonding failure occurred at the wrapping layer due to the concentration of shear stress at the interface between the concrete and the reinforcement.

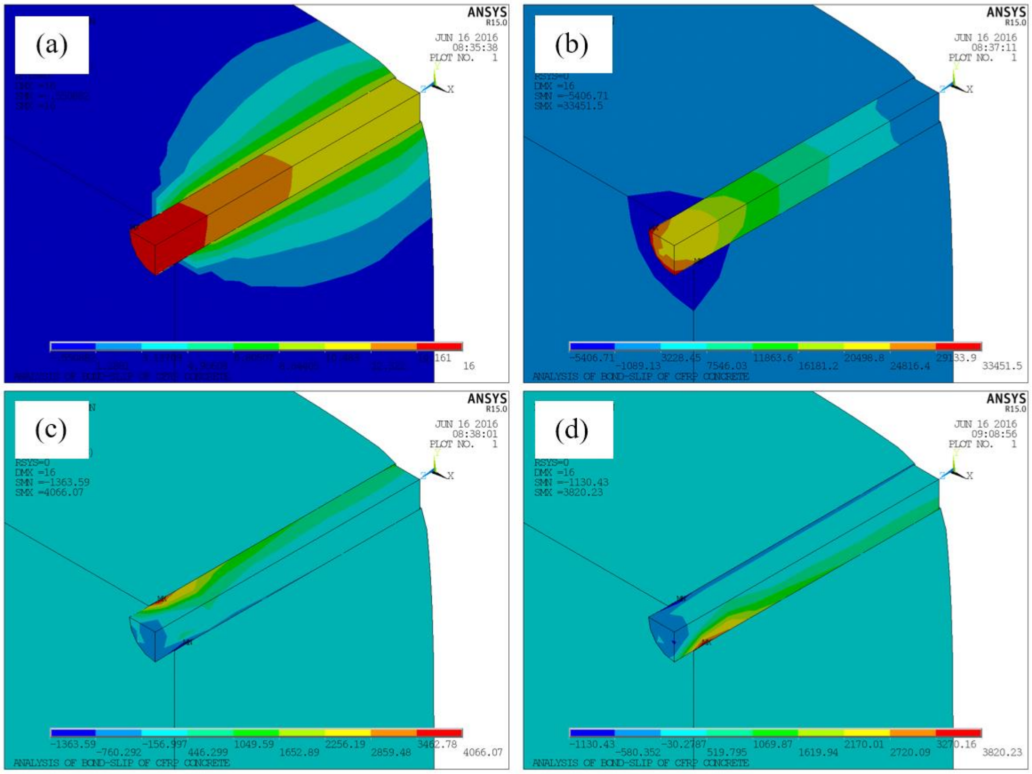

Figure 6-8 Coutour plots: (a) Z-component of displacement, (b) Z-component of stress

6.5 Conclusions

An experimental investigation of the debonding behavior between concrete and CFRP rebar using AE technique was conducted. Three CFRP rebar reinforced concrete specimens were prepared and subjected to pullout tests. The damage evolution during the pullout tests was continuously measured by a sophisticated AE system. Results showed that the debonding failure between concrete and reinforcement was characterized by the total peeling off of the CFRP helical wrapping layer. The changes in AE parameters were closely related to damage evolution in the reinforced concrete. Therefore, the AE response was analyzed by AE hits, amplitude and peak frequency. These parameters characterized the debonding damage evolution from different perspective. The sudden change in AE hits rate indicated the occurrence of new types of microstructural damage. A sudden increase in AE hits rate occurred after a noticeable slippage occurred. This stage was characterized by the total loss of chemical adhesion and mechanical interlocking dominated the load transfer capacity between concrete and reinforcement. The sudden increase in AE hits rate can be attributed to the breakage of the CFRP helical layer. From amplitude perspective, three clusters of strong signals can be observed at the transition phase of the bond mechanism. These clusters were corresponding to initiation of losing chemical adhesion, mechanical interlocking related damage and friction between concrete and reinforcement. The peak frequency plot clearly showed the occurrence of different damage mechanism. AE signals with peak frequency lower than 150 kHz were likely related to the microfracture of concrete and CFRP rebar. The signals with peak frequency range between 200 kHz and 300 kHz can be associated to fiber/matrix debonding occurred in the within the CFRP rebar. And lastly the third frequency band (above 350 kHz) was related to fiber breakage within the CFRP rebar. It can be concluded that the AE response was able to characterize the damage evolution during the debonding failure of CFRP rebar reinforced concrete. Lastly, stress field analysis using FEA of the indicated that the interface between reinforcement and concrete was the most critical region for the bonding strength between these two constituents.

7 Interfacial Debonding Detection in FRP Rebar Reinforced Concrete Using Electro-Mechanical Impedance Technique

7.1 Introduction

For reinforced concrete structures, the use of fiber reinforced polymers (FRP) rebars as an alternative to steel reinforcements has attracted much attention in recent years, particularly in the situations where corrosion is present. The FRP composite reinforcing bars have advantages in terms of light weight, high tensile strength, high corrosion resistance, good fatigue endurance and non-electromagnetic [125]. Thus, the FRP rebars can be advantageously utilized as reinforcing element for concrete structures in highly corrosive environments, such as seawalls, bridge decks and pavements exposed to deicing salts. The interfacial bonding between the FRP rebars and the concrete is critical in achieving the structural performance of the reinforced concrete. The bonding strength is made up of three forces that are present on the rebar-concrete interface: the chemical adhesion between the rebar and concrete, the frictional force between the rebar and concrete, and the mechanical interlocking force resulting from the ribs of the rebar [108, 126]. Each force contributes to the overall bonding strength in varying degrees. The chemical adhesion dominates if there are no slippage of the rebar, while friction and interlock forces dominate the overall bonding strength under slipping of the rebar. Over time, the interfacial bonding will deteriorate due to environmental and load-related issues, resulting in complete debonding damage to the FRP rebar reinforced concrete structure. Debonding damage could weaken the structural integrity, reduce the tensile resistance of the structure, and make the structure more vulnerable to further damage. In addition, in contrast to steel rebars, the stress-strain relationship of FRP rebars shows a linear characteristic at all stress levels up to the point of failure and there is no yielding characteristic. Therefore, there is a need to develop an effective nondestructive evaluation technique to monitor the initial installation quality and the long-term efficiency of the interfacial bonding between FRP and concrete.

To ensure the proper coupling of the FRP materials with the host structure, the interfacial bonding condition between them has to be monitored. Various debonding monitoring methods have been developed over the last few decades. To name a few, acoustic emission [127], time reversal acoustics [128], infrared thermography [129], fiber optic sensing [130-132], diagnostic lamb waves [133], have been applied. These techniques are demonstrated to successfully identify FRP debonding damage. However, these methods typically employ sophisticated and expensive instruments and substantial access to the structures that is not always possible for civil infrastructure applications. Furthermore, the interpretation of data often requires experienced personnel to analyze manually, and_the automation of data analysis remains largely unsolved. For some techniques, the measurement data are collected in the time domain and often require complex processing in frequency domain. The shortcomings of current techniques hold limited promise for real-time and in-service monitoring of structural damage.

Electro-mechanical impedance (EMI) based damage detection technique using Lead-Zirconate-Titanate (PZT) patches is emerging as an innovative and powerful tool for detecting local damage in a wide variety of structures [32, 134-138]. A key aspect of EMI based structural health monitoring (SHM) is the adoption of PZT patches as collocated sensors and actuators. The basic principle of EMI damage detection technique is to detect the variations of structural mechanical impedance caused by the occurrence of damage. According to the electro-mechanical coupling property of a PZT patch bonded on a host structure, the electrical impedance or admittance (inverse of impedance) of the PZT patches is directly associated with the mechanical impedance of the host structure, and will be affected by the occurrence of structural damage. Through monitoring the electrical impedance or admittance of the PZT patches bonded on the host structure and comparing it to a baseline measurement, the structural conditions of the host structure can be qualitatively determined. The small size PZT patches employed by EMI technique can be conveniently bonded on or embedded into a structure, even in locations that is inaccessible, to perform damage assessment actively. Additionally, this technique can assess the structural integrity in real-time and the requirements of the sensors and the procedures of data processing are minimal, which facilitate the autonomous structural health monitoring. Extensive research activities have been conducted in applying the EMI technique for local damage detection in a variety of research fields, such as crack detection [136, 139, 140], concrete strength monitoring [141-143], dental implant assessment [144, 145], corrosion monitoring of reinforced concrete [146], lap-joint monitoring [147], and debonding monitoring on CFRP laminated concrete [148] and concrete encased composite structure [149].

Nonetheless, the EMI technique has never been applied to monitor the interfacial debonding damage of a FRP rebar reinforced concrete structure. This chapter of the dissertation investigates the application of the EMI technique to detect interfacial debonding damage development in a FRP rebar reinforced concrete when the specimen was subjected to reinforcement pullout test. A CFRP rebar reinforced concrete specimen was prepared in laboratory and two PZT patches were attached to the specimen at different locations. The impedance and admittance signatures of the PZT patches bonded on the specimen were acquired under the pullout test. In order to quantify the impedance signatures under different debonding conditions, statistical metrics, which includes root mean square deviation (RMSD) and mean absolute percentage deviation (MAPD), were used.

7.2 Theoretical background

7.2.1 Electro-mechanical impedance-based SHM technique

PZT patches are small, noninvasive, and inexpensive sensors/actuators that can be easily attached to or embedded into a structure. They operate on the principle of piezoelectricity, which means surface charges are generated when mechanical stressed, and conversely, mechanical strains are produced when electric fields are applied. The EMI-based health monitoring techniques employ one PZT patch for both actuation and sensing of the structural responses. The PZT patches are surface-bonded or embedded into a host structure, and electrically excited by an impedance analyzer with a high frequency band (typically between 30 kHz and 400 kHz) and the electrical impedance signatures are simultaneously measured. The interaction between the PZT patch and a host structure can be idealized as an electro-mechanical system, as shown in Figure 7-1. The analytical model of this setup was first proposed by Liang et al. [28] and subsequently implemented by many others researchers [29-33]. The electrical admittance (inverse of the electrical impedance), $Y(\omega)$, of a PZT patch is related to the mechanical impedance of the host structure, $Z_s(\omega)$, and that of a PZT patch, $Z_a(\omega)$ through the following equation:

$$Y(\omega) = j\omega \frac{wl}{h}\left\{\bar{\varepsilon}_{33}^{T} - d_{31}^{2}\bar{Y}^{E} + \left(\frac{Z_a(\omega)}{Z_s(\omega)+Z_a(\omega)}\right) d_{31}^{2}\bar{Y}^{E}\left(\frac{\tan\kappa l}{\kappa l}\right)\right\}, \tag{7-1}$$

where w, l and h are the width, length and thickness of the PZT patch, respectively; $\bar{\varepsilon}_{33}^{T} = \varepsilon_{33}^{T}(1-\delta)$ is the complex electric permittivity of a PZT patch at constant stress, where δ denotes the dielectric loss factor of a PZT patch; $\bar{Y}^{E} = Y^{E}(1+\eta)$ is the complex Young's modulus of a PZT patch at a constant electric field, η denotes the mechanical loss factor of the PZT patch; d_{31} is the piezoelectric constant of a PZT patch, $Z_s(\omega)$ and $Z_a(\omega)$ are the mechanical impedance of a PZT patch and the host structure, respectively; $\kappa = \omega\sqrt{\rho/\bar{Y}^{E}}$ is the wave number and ρ is the mass density of a PZT patch.

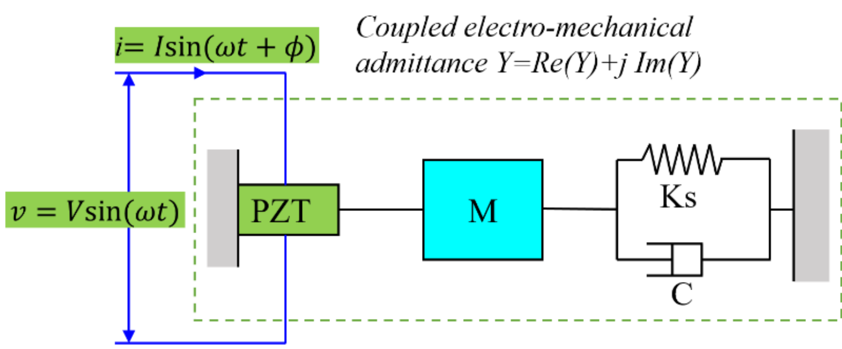

Figure 7-1 One-dimensional electro-mechanical model between a PZT patch and a host structure

Damage to a structure causes direct changes in the structural stiffness and/or damping, and thus alters the mechanical impedance of the structure. As indicated by Equation 7-1, as long as the mechanical impedance and material properties of the PZT patch remain unchanged, any modifications in the mechanical impedance of a structure results directly in the changes in the electrical impedance measured by the PZT patch.

7.2.2 Debonding induced impedance variation

The mechanical impedance of the host structure is the ratio of the applied force to the resulting velocity of the structure. According to another work by Liang et al. [150], the mechanical impedance of the host structure can be derived as

$$Z_s(\omega) = -\frac{F}{\dot{x}} = c + \frac{m\omega^2 - K_s}{\omega} i, \tag{7-2}$$

where F is the applied force, $\dot{x}$ the resulting velocity, c the damping coefficient, m the mass, ω the angular frequency, K_s the static stiffness and i is imaginary number, respectively. Then the static stiffness of the host structure can be calculated by the following equation

$$K_s = m\omega^2 - \frac{\omega[Z_s(\omega) - c]}{i}, \tag{7-3}$$

which relates the static stiffness to the mechanical impedance of the host structure.

Referring to Figure 7-2(a), the static stiffness of the pullout specimen is expressed as

$$K_s = F/u, \tag{7-4}$$

where F is the pullout force, and u is the overall displacement at the loading end. The overall displacement at the loading end of the rebar consists of three components, which is given by

$$u = u_c + u_s + s, \tag{7-5}$$

where u_c, u_s, s are the displacement of the concrete due to deformation, displacement of the FRP rebar due to deformation, and slip between rebar and concrete, respectively.

According to mechanics of materials, u_c and u_s can be expressed as

$$u_c = \frac{F}{A_c E_c} h_c \text{ and} \tag{7-6}$$

$$u_s = \frac{F}{A_s E_S} l_s, \tag{7-7}$$

where A_c, E_c, h_c are the cross-section, modulus of elasticity, and height of concrete, respectively; A_s, E_S, l_s are the cross-section, modulus of elasticity, and length of the FRP rebar, respectively.

Substituting Equation 7-5 through 7-7 back to Equation 7-4 and rearranging, we have

$$\frac{1}{K_s} = \frac{h_c}{A_c E_c} + \frac{l_s}{A_s E_S} + \frac{s}{F}. \tag{7-8}$$

As can be seen, in the CFRP rebar reinforced concrete structure, the stiffness K_s consists of three parts: the stiffness of concrete, the stiffness of CFRP rebar and the stiffness of the contact zone of the CFRP rebar and the concrete. Equation 7-8 relates the global stiffness of the pullout specimen and the debonding slip between rebar and the concrete. Combining Equation 7-3 and Equation 7-8, we can see that the debonding between the CFRP rebar and the concrete will induce a change in the mechanical impedance of the structure, which is detected by the electrical impedance of the PZT patch.

7.2.3 Statistical damage metrics: RMSD and MAPD

The damage assessment made from the impedance signatures is only qualitative. Thereafter, scalar damage metrics need to be defined to quantify the difference in the electrical impedance signatures before and after the damage. The RMSD and MAPD are the statistical metrics that are commonly used in structural health monitoring of structures as damage indices. The mathematical expressions of these metrics in terms of the real part of the electrical admittance $\mathrm{Re}(Y)$ of the bonded PZT, are given as follows [24]:

$$\mathrm{RMSD}(\%) = \sqrt{\sum_{i=1}^{N}\left[\mathrm{Re}\left(Y_{i,1}\right) - \mathrm{Re}\left(Y_{i,0}\right)\right]^2 / \sum_{i=1}^{N}\left[\mathrm{Re}\left(Y_{i,0}\right)\right]^2} \text{ and} \tag{7-9}$$

$$\mathrm{MAPD}(\%) = \frac{1}{N}\sum_{i=1}^{N}\left|\left[\mathrm{Re}\left(Y_{i,1}\right) - \mathrm{Re}\left(Y_{i,0}\right)\right] / \mathrm{Re}\left(Y_{i,0}\right)\right|, \tag{7-10}$$

where N is the number of sampling points in the EMI spectra; the subscripts 0 and 1 denote the baseline measurement and concurrent measurement, respectively. For these two metrics, the greater numerical value, the larger the difference between the baseline measurement and the concurrent measurement, indicating the presence of the larger or more damage in a structure.

7.3 Experimental setup

7.3.1 Materials

In order to verify the applicability and efficacy of the EMI-based SHM technique for debonding damage monitoring of FRP rebar reinforced concrete structure, experiments on a pullout specimen were conducted. The FRP rebar used was carbon fiber reinforced polymer (CFRP) due to its high strength property. For the experimental determination of the debonding behavior between reinforcement and concrete, a pullout specimen with rebar embedded in the middle of the concrete is usually adopted. Figure 7-2 depicts the geometry details of the specimen.

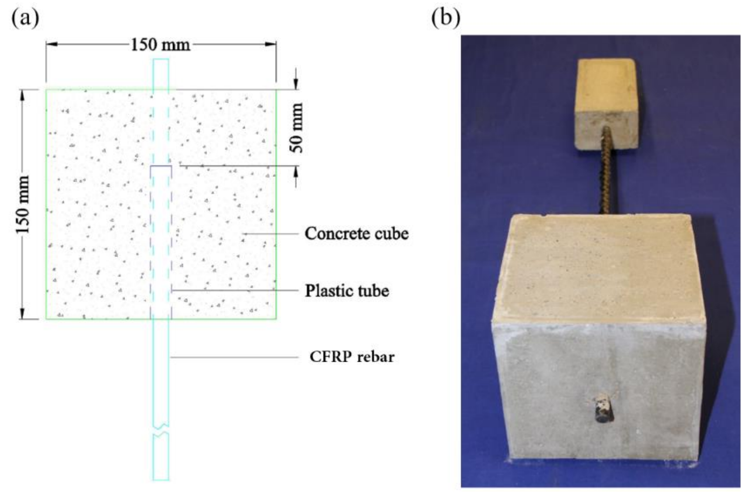

Figure 7-2 CFRP rebar reinforced concrete pullout specimen (a) sketch and (b) photo

The CFRP rebar used here is 600 mm long and has a nominal diameter of 10 mm with helical wrapping on its surface. The CFRP rebar was placed in the middle of a concrete cube with dimensions of 150 mm × 150 mm × 150 mm. The bonding length between the rebar and the concrete was set at 50 mm. At the loading end of the specimen, bonding was prevented by inserting a 100 mm long plastic tube to minimize stress concentration and reduce edge effects. In order to provide a pulling force on the rebar, a counteracting concrete block with an embedment 180 mm length was casted on the another end of the rebar as shown in Figure 7-2. The concrete used for preparing the specimens was a premixed, ready to use product (Concrete Mix 1101, QUIKRETE) with 27 MPa compression strength at 28 days curing. The concrete was compacted carefully using a table vibrator. The specimen was demolded from the wooden frame after 24 hours of casting. The specimen was cured for 7 days before the pullout test, which was used to initiate the debonding damage between the CFRP rebar and the concrete.

7.3.2 Pullout test setup and EMI monitoring

The setup for the pullout test is shown in Figure 7-3. The pullout test was performed on an INSTRON 4482 universal testing machine with a capacity of 100 kN. Two specialized loading cages were manufactured to transfer the force from the specimen to the machine. The testing mode was set to the displacement control at a rate of 1 mm/min. Displacement control was selected to obtain the post-peak behavior. The load and the displacement information were recorded by the electronic load cell of the testing machine.

The EMI measurements were performed using an Agilent 4294A impedance analyzer. The EMI measurement instrumentation consists of PZT patches, impedance analyzer and a personal computer equipped with data acquisition software, as shown in Figure 7-3. Two PZT patches, which have a size of 8 mm × 7 mm × 1 mm, were bonded on the surface of the concrete. One PZT patch was bonded very close to the CFRP rebar on the top surface of the specimen (denoted as PZT-T) and the other one on the front surface of the specimen (denoted as PZT-F), as shown in Figure 7-3. The PZT patches were bonded on the specimen surface using epoxy resin three days before the pullout test to ensure complete curing of the bond adhesive. Using the impedance analyzer, the EMI spectra of the PZT patches were scanned using a frequency range between 200 kHz and 260 kHz. The spectra for the impedance and admittance, including their real part and imaginary part, of the PZT patches were measured and stored in the control laptop for further processing. The real part and imaginary part of impedance are resistance and reactance, respectively. And the real part and imaginary part of admittance are conductance and susceptance, respectively. The sensitivity of these parameters were then compared using the quantitative measure, RMSD and MAPD. Baseline measurements of the PZT patches were firstly recorded at a healthy stage (before application of pullout displacement). Then, the EMI measurements were taken every 2 mm in displacement during which the testing machine was stopped.

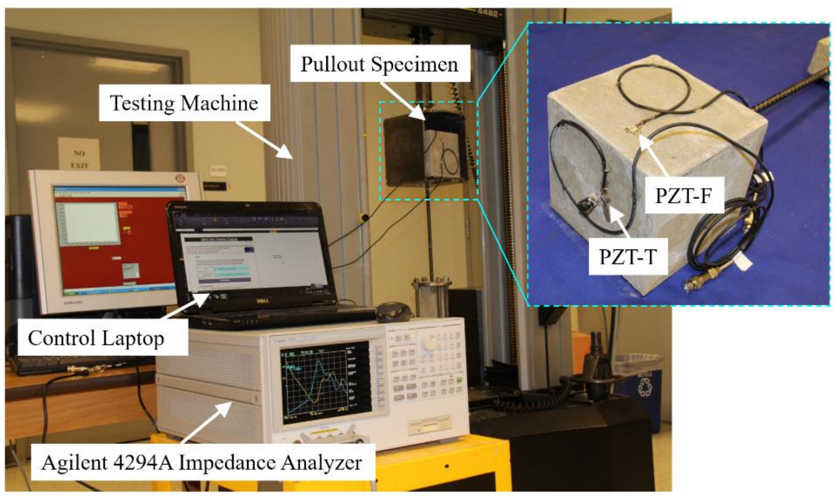

Figure 7-3 Experimental setup and PZT patches attached to the host structure

7.4 Results and discussion

7.4.1 Debonding characteristics

The load-displacement curve registered by the testing machine is shown in Figure 7-4. The load-displacement curve shows a relative linear relationship to the point that debonding mechanism is initiated, notably at a displacement of 8 mm. The load peaked at a displacement of 10 mm and began dropping. Based on the characteristics of the load-displacement curve, the pullout of the CFRP rebar can be divided into three stages. In

Stage I, the load-displacement curve shows linear relationship during which no slip occurs and the bonding strength is ensured mostly by the chemical adhesion. The end of Stage I is marked by the breakdown of the chemical adhesion that allows the slippage of the rebar. At this point the debonding mechanism is initiated. In Stage II, the slope of the load-displacement curve is decreased. The bonding strength is come from the mechanical interlocking and friction mechanisms. The load continues growing and the maximum bond strength is reached. A decrease in the pullout load indicates the loss of the mechanical interlocking strength and signifies the beginning of Stage III. In this stage, the bond strength is due to the friction between the rebar and the surrounding concrete. Under the continued loading, the interfacial surface of the CFRP rebar is smoothed, leading to a further decrease of the bond strength. It is worth noting that there are some relaxation effects at the measurement points at higher load levels since the testing machine was stopped every 2 mm displacement for EMI measurements.

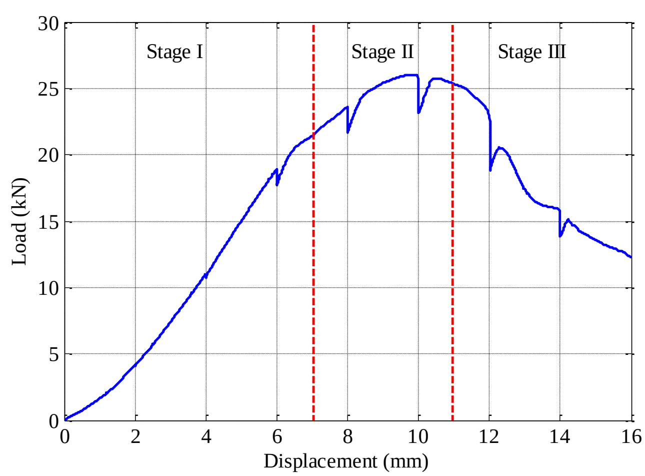

Figure 7-4 Load-displacement curve of the pullout specimen

7.4.2 EMI response spectra

Prior to measuring the signatures of impedance and admittance, the conductance (real part of the admittance) was scanned to determine an appropriate frequency range. Conductance was chosen for this scan because it is more directly related to the resonant frequency of the PZT patch. Figure 7-5 shows the conductance spectra when the PZT patches was free in the air and interacted with the host structure for a wide frequency range between 1 kHz and 1 MHz. In free condition, both PZT patches tend to resonate at 220 kHz. When the PZT patches were bonded onto the host structure, their amplitudes were significantly suppressed and their resonant frequencies shifted to 250 kHz. This is because the bonding of PZT patches restrained their vibration and increase their stiffness. Therefore, the frequency range between 200 kHz and 260 kHz was chosen for the scanning of impedance and admittance signatures during the pullout test.

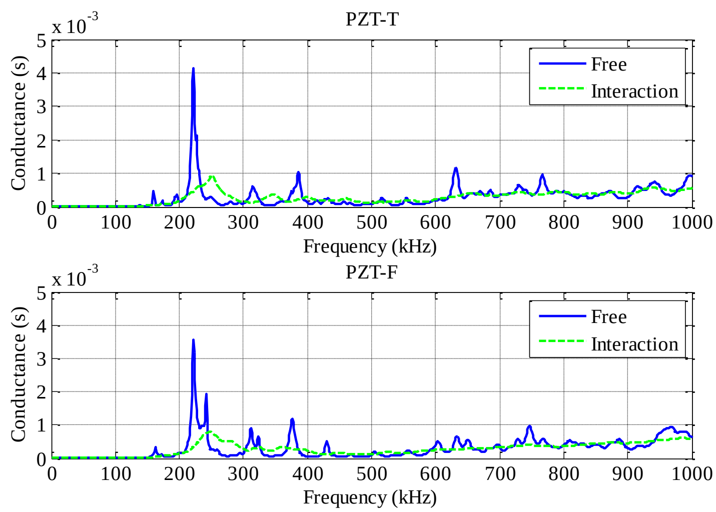

Figure 7-5 Conductance spectra between free condition and interaction condition: the one bonded on top surface (top) and the one bonded on front surface (bottom)

The electrical impedance and admittance spectra from EMI measurements of the PZT-T (the one bonded on the top surface) patch are shown in Figure 7-6. The impedance and admittance spectra as well as spectra for their real and imaginary part were scanned over the frequency range between 200 kHz and 260 kHz. Since the spectra are closely spaced, only five out of the nine measurements are presented for clarity, namely those for baseline, 4 mm, 8 mm, 12mm and 16 mm displacements. As can be seen from the figure, there are some noticeable variations for all these measurements at different displacement levels as compared to the baseline measurement. Intuitively, the deviation level increases with the increasing of the displacement levels. This can be explained by the fact that the debonding damage became more severe as the CFRP rebar was gradually pulled further away from the concrete. The debonding that occurred at the interface between the CFRP rebar and concrete destroyed the integrity of the CFRP rebar reinforced concrete structure, thus causing a change to the local stiffness and damping. As a result, the mechanical impedance of the specimen was altered as evident with the deviations in the impedance and admittance signatures. Figure 7-7 shows the impedance and admittance signatures of PZT-F (the one bonded on the front surface). Here, only two of the six parameters are shown. As can be seen, the variations of the spectra during the debonding process are very small as compared to the results from PZT-T. The main reason is that PZT-F was located further away from where the debonding damage took place, rendering it less sensitive to the damage. It is well-acknowledged that the sensing region of the PZT patch is limited to a small region around it under the high-frequency excitation. The sensing region is difficult to obtain though extensive theoretical modeling have been performed

[134]. Park et al. [134] estimated that a PZT can have a sensing radius of 0.4 m on composite reinforced concrete structures and 2 m on metal beams. The sensing region can also be varied by the materials properties, geometry of the structure. In our case, the debonding damage occurred at the interface between the CFRP rebar and the concrete. The PZT patch (PZT-T) located close to the damage was sensitive to the damage while PZT-F that located further from the damage showed very limited changes in the impedance signatures. Indeed, it would be very favorable to test the sensitivity of the EMI method for this type of structure prior to performing the experiment.

All these parameters explained the interfacial debonding damage evolution to a certain extent. However, it is difficult to determine different stages of the CFRP pullout experiment from the spectra. Thereafter, we should resort to the quantitative assessment metrics such as RMSD and MAPD.

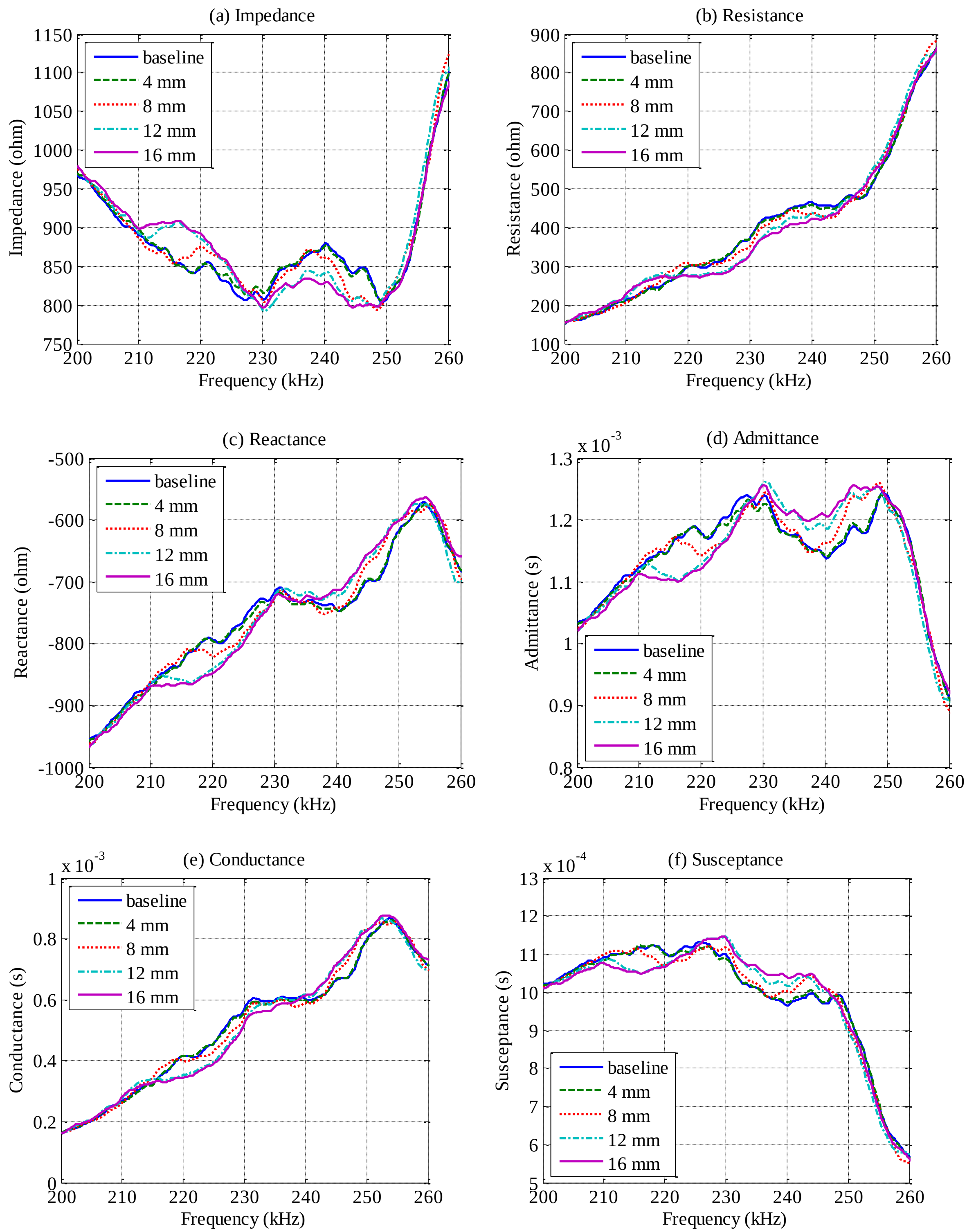

Figure 7-6 Impedance and admittance signatures of PZT-T: (a) impedance, (b) resistance, (c) reactance, (d) admittance, (e) conductance and (f) susceptance

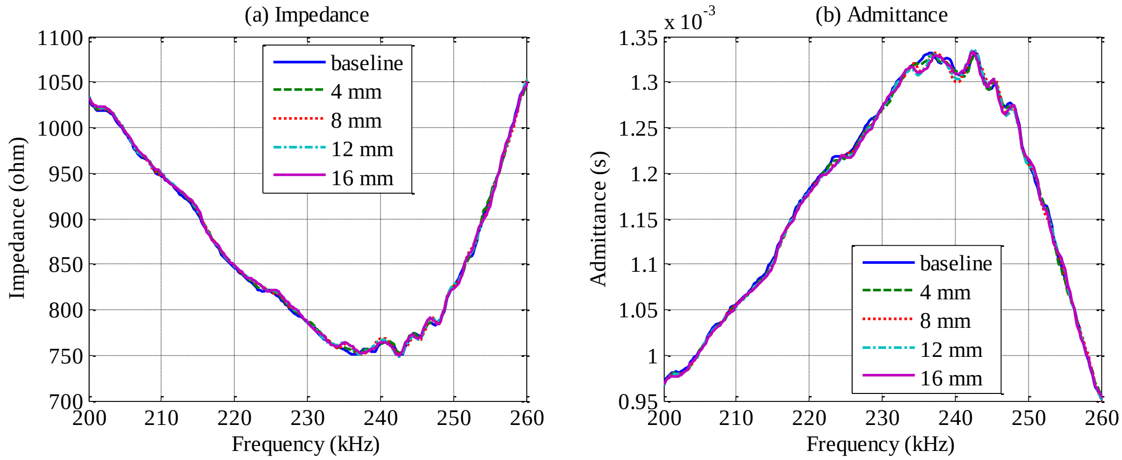

Figure 7-7 Impedance and admittance signatures of PZT-F: (a) impedance, (b) admittance

7.4.3 Quantitative damage metrics

Note that the results from the conductance signatures are so far qualitative. To account for the overall variations in the impedance and admittance signatures during the CFRP rebar reinforced concrete pullout test, statistical damage metrics such as RMSD and MAPD were used to quantify the debonding damage. Figure 7-8 shows the RMSD and MAPD damage metrics of the impedance and admittance signatures of PZT-T at different displacement levels, together with load-displacement curve. The RMSD metrics for these parameters show a resembling trend, with those for resistance and conductance have the highest sensitivity and the rest have similar sensitivity. It is evident that the RMSD metrics of all these parameters are able to reflect the debonding damage evolution and classify the damage process into three stages. The RMSD metrics stay at a low value in Stage I, where no debonding damage was detected. Starting from the Stage II, the RMSD metrics suddenly rise to a larger value. The sudden change in the damage metrics indicates some dramatic mechanical damage occurred in the CFRP rebar reinforced concrete. This transition point can be attributed to the initiation of debonding damage between the rebar and the concrete. A slight increases in these damage metrics are further observed after a displacement of 10 mm. The RMSD metrics reach relative stable values in Stage III due to no dramatic damage was occurred. The same characteristics can also be observed for the calculated MAPD damage metrics, as evident in Figure 7-8. Overall, these damage metrics are able to quantify the changes impedance and admittance signatures due to debonding of the pullout specimen and indicate the different stages of the CFRP rebar pullout process.

As for comparison of the sensing area, Figure 7-9 shows the RMSD and MAPD damage metrics of PZT-F at different displacement levels. It is evident that the metrics from PZT-F are a lot smaller, which have values less than 1 %. This means that the variations of the impedance and admittance signatures are very small due to the debonding damage. As mentioned above, the sensing area of the PZT patch is small for this type of structure. In practical application, it is suggested that the PZT patches should be installed in close proximity to the rebar in order to obtain more useful damage information.

It is interesting to note that resistance and conductance have the best sensitivity as compared to other parameters. Both of them are the real parts, especially impedance and admittance, respectively. As observed in Figure 7-8, the RMSD and MAPD of both resistance and conductance have higher percentage in the overall debonding process, which almost double those values of the other four parameters. The RMSD and MAPD of resistance and conductance have the highest values above 6 % while the highest values for the other four parameters are around 3 %. When it comes to real world application of the EMI technique for CFRP rebar reinforced concrete debonding detection, resistance and conductance should be primarily picked for scanning and subsequently performing damage assessment.

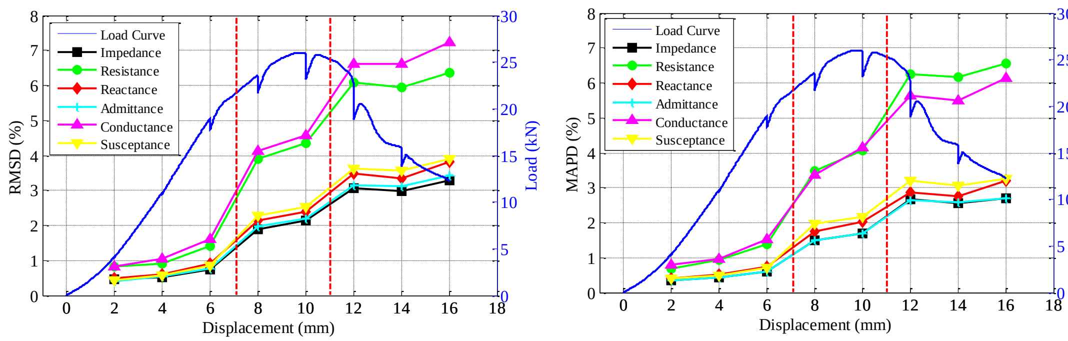

Figure 7-8 The RMSD (left) and MAPD (right) damage metrics of the impedance and admittance signatures for PZT-T at different displacement levels together with load-displacement curve

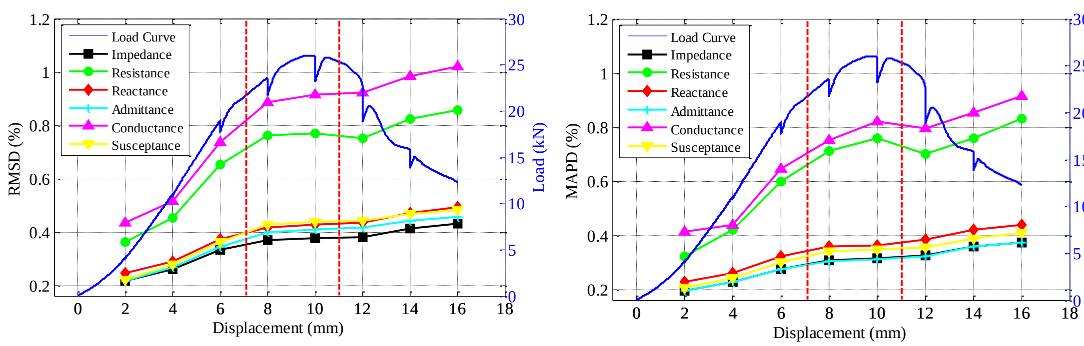

Figure 7-9 The RMSD (left) and MAPD (right) damage metrics of the impedance and admittance signatures for PZT-F at different displacement levels together with load-displacement curve

7.4.4 Discussion

One issue related to the application of the EMI-based structural health monitoring is the expensive impedance measurement device. In our laboratory based investigation, the adopted measuring equipment is the Agilent 4294A impedance analyzer, which is bulky, costly and not suitable for in-situ structural health monitoring. However, the low cost (about $150) and practical application of EMI-based structural health monitoring is achievable using the commercially available impedance measuring device AD5933 by Analog Device. This impedance evaluation board allows one to measure impedance up to 100 kHz. The efficacy of this device in EMI-based SHM of various structures and damage types has been extensively investigated [137, 138, 151]. And the wireless capability of such device was also examined [152, 153]. With this impedance measuring chip, the low cost EMI-based structural health monitoring is achievable.

Regarding the practical issues of the application of EMI method in SHM of real world structures. One of the practical issues would be how to differentiate the variation of EMI signatures from CFRP debonding damage and from other types of damage. To date, most of the research initiatives of EMI technique are still focused on lab-based monitoring. Admittedly, the real application of the EMI technique has frequently been questioned. Several researchers have discussed the practical issues of EMI in real applications in depth [154-156]. The issue regarding whether the variation of EMI signatures caused by one specify damage or other damage has also been investigated.

One method is to take the advantage of the frequency dependent properties of each damage types. Different types of damage may induce the variation in the EMI signatures at different frequency range. For example, some damage types may vary the EMI signatures at high frequency range while other damage types may induce changes in the EMI signatures at low frequency range. Thus, some of the damage types can be isolated if either the low frequency range is scanned for EMI signatures or high frequency range is scanned for EMI signatures. Yang et al. utilized the high frequency range to differentiate between temperature induced and damage induced signature variations [154]. For our case, in order to identify whether the debonding of CFRP or other damage induce the EMI signature variations, more experimental investigations should be performed to study the response of the EMI signatures corresponding to each damage type, especially to identify the frequency range to that damage type. Based on the frequency dependent response of the EMI signatures to damage types, a selection of specify frequency range is able to isolate the influence of some other damage types on the EMI signatures.

Another method is to incorporate other measuring techniques, such as load measurement using fiber optic sensors, guided ultrasonic waves testing, acoustic emission technique, etc. These methods are also widely used in structural health monitoring of reinforced concrete structures. With the rich information obtained from these measuring techniques, it is possible to characterize the characteristics of debonding damage or damages coming from other sources.

7.5 Conclusions

The applicability of EMI-based SHM technique for debonding damage detection in CFRP rebar reinforced concrete structure was investigated in this chapter. From the experimental results, it is found that the low cost PZT patches have good capability for detecting the debonding damage of the CFRP rebar reinforced concrete. The PZT patch should be closely located at the place where debonding damage occurred to achieve adequate sensitivity. So long as the sensitivity was guaranteed, the variations in the impedance and admittance spectra at different pullout displacement levels were shown to be an indicator of the debonding damage. Statistical damage metrics, such as RMSD and MAPD were adopted to quantify the changes in the spectra of impedance and admittance. These damage metrics can clearly indicate the debonding damage evolution and classify the three stages of the CFRP pullout experiment. From the results, these damage metrics can serve as reliable indicators for the debonding evolution at the interface between the CFRP rebar and the concrete. It is interesting to note that the real parts of impedance and admittance, namely resistance and conductance, have the best sensitivity. The research outlined in this work would possibly serve as a valuable reference for practical engineering in terms of debonding damage monitoring of FRP rebar reinforced concrete.

8 General Conclusions and Future Work

Smart sensors have been widely used in the field of structural health monitoring. This dissertation has presented five innovative designs and applications of smart sensors to solve some of the newest engineering problems in the field of structural health monitoring.

In chapter three, the development of the combined carbon fiber/FBG active thermal probe for corrosion detection of steel reinforced concrete structures was presented. Results suggested that there is a strong correlation between corrosion degree and temperature response. Increased degrees of corrosion lead to higher temperature on the thermal probe when a short duration of heat pulse is applied. Further work should focus on the in-depth study of the correlation between the corrosion degree and the temperature response measured by the thermal probe.

Chapter four presented the newly developed fiber optic macro-bend metal loss sensor that can be used to detect and characterize the corrosion pits of metallic structures. The sensor is able to measure the rough geometry of the corrosion pit of various shapes. The sensor has the advantages of simple structure, low cost, non-contact and remote sensing, which will be a promising technique in detecting undesired metal loss, such as in the field of corrosion detection and assessment. Recommendations for further study will be the modeling and calibration of hysteresis compensation.

Chapter five presented the feasibility study of using smart aggregates as embedded acoustic emission sensors for damage characterization of concrete structures. Results showed that the embedded smart aggregates are able to detect acoustic emission events generated from damage evolution of concrete structures. The presented embedded acoustic emission sensor has the advantages of low cost, simple structure, and well-suited for embedding in large-scale concrete structures. Future development in this topic includes the effects of environmental impacts especially temperature variation, and the application in real world large-scale concrete structures.

In chapter six, the experimental investigation of the debonding behavior between concrete and carbon fiber reinforce polymer rebar using acoustic emission technique was conducted. The changes in acoustic emission parameters are closely related to damage evolution in the reinforced concrete. The sudden change in acoustic emission hits rate indicates the occurrence of new types of microstructural damage. From amplitude perspective, three clusters of strong signals can be observed at the transition phase of the bond mechanism. The peak frequency plot clearly shows the occurrence of different damage mechanism. It can be concluded that the acoustic emission response is able to characterize the damage evolution during the debonding failure of carbon fiber reinforce polymer rebar reinforced concrete. A continuation of this work will involve the application of the embedded acoustic emission sensors, as described in chapter five, in measuring the debonding behavior between concrete and carbon fiber reinforce polymer rebar.

In chapter seven, however, debonding behavior between concrete and carbon fiber reinforce polymer rebar was characterized using electro-mechanical impedance technique. From the experimental results, it is found that the low cost piezoelectric patches have good capability for detecting the debonding damage of the carbon fiber reinforce polymer rebar reinforced concrete. The damage metrics, which are root mean square deviation and mean absolute percentage deviation, can clearly indicate the debonding damage evolution and classify the three stages of the carbon fiber reinforce polymer pullout experiment. Further investigation in this topic will aim towards the issues of how to differentiate the impedance changes induced by debonding and other types of damage.

References

[1] D. Balageas, C.-P. Fritzen, and A. Güemes, *Structural Health Monitoring* vol. 90: John Wiley & Sons, 2010.

[2] A. Maier, L. Benassi, and C. Stolz, "Structural Health Monitoring of Repairs," DTIC Document2010.

[3] H. Speckmann and R. Henrich, "Structural Health Monitoring (SHM)–Overview on Technologies under Development," in *Proc. of the World Conference on NDT, Montreal-Canada*, 2004.

[4] C. R. Farrar, S. W. Doebling, and D. A. Nix, "Vibration–based Structural Damage Identification," *Philosophical Transactions of the Royal Society of London A: Mathematical, Physical and Engineering Sciences*, vol. 359, pp. 131-149, 2001.

[5] K. Fukunaga, *Introduction to Statistical Pattern Recognition*: Academic press, 2013.

[6] T. H. Ooijevaar, *Vibration based Structural Health Monitoring of Composite Skin-Stiffener Structures*: Universiteit Twente, 2014.

[7] C. R. Farrar, H. Sohn, F. M. Hemez, M. C. Anderson, M. T. Bement, P. J. Cornwell, S. W. Doebling, J. F. Schultze, N. Lieven, and A. N. Robertson, "Damage Prognosis: Current Status and Future Needs," *Report. Los Alamos, NM, USA: Los Alamos National Laboratory*, 2003.

[8] C. R. Farrar and K. Worden, "An Introduction to Structural Health Monitoring," *Philosophical Transactions of the Royal Society of London A: Mathematical, Physical and Engineering Sciences*, vol. 365, pp. 303-315, 2007.

[9] S. W. Doebling, C. R. Farrar, M. B. Prime, and D. W. Shevitz, "Damage Identification and Health Monitoring of Structural and Mechanical Systems from Changes in Their Vibration Characteristics: A Literature Review," 1996.

[10] A. Rytter, "Vibrational based Inspection of Civil Engineering Structures," 1993.

[11] J. M. López-Higuera, L. R. Cobo, A. Q. Incera, and A. Cobo, "Fiber Optic Sensors in Structural Health Monitoring," *Journal of lightwave technology*, vol. 29, pp. 587-608, 2011.

[12] W. R. Habel and K. Krebber, "Fiber-Optic Sensor Applications in Civil and Geotechnical Engineering," *Photonic sensors*, vol. 1, pp. 268-280, 2011.

[13] C. K. Leung, K. T. Wan, D. Inaudi, X. Bao, W. Habel, Z. Zhou, J. Ou, M. Ghandehari, H. C. Wu, and M. Imai, "Review: Optical Fiber Sensors for Civil Engineering Applications," *Materials and Structures*, vol. 48, pp. 871-906, 2015.

[14] N. Sabri, S. Aljunid, M. Salim, R. Ahmad, and R. Kamaruddin, "Toward Optical Sensors: Review and Applications," in *Journal of Physics: Conference Series*, 2013, p. 012064.

[15] J. Castrellon-Uribe, *Optical Fiber Sensors: An Overview*: INTECH Open Access Publisher, 2012.

[16] D. Marcuse, "Curvature Loss Formula for Optical Fibers," *JOSA*, vol. 66, pp. 216-220, 1976.

[17] G. Meltz, W. W. Morey, and W. Glenn, "Formation of Bragg Gratings in Optical Fibers by a Transverse Holographic Method," *Optics letters*, vol. 14, pp. 823-825, 1989.

[18] K.-t. Lau, L. Yuan, L.-m. Zhou, J. Wu, and C.-h. Woo, "Strain Monitoring in FRP Laminates and Concrete Beams using FBG Sensors," *Composite Structures,* vol. 51, pp. 9-20, 2001.

[19] Z. Wu, B. Xu, K. Hayashi, and A. Machida, "Distributed Optic Fiber Sensing for a Full-Scale PC Girder Strengthened with Prestressed PBO Sheets," *Engineering Structures,* vol. 28, pp. 1049-1059, 2006.

[20] D. Zhang, B. Shi, H. Cui, and H. Xu, "Improvement of Spatial Resolution of Brillouin Optical Time Domain Reflectometer using Spectral Decomposition," *Optica Applicata,* vol. 34, pp. 291-302, 2004.

[21] A. Barrias, J. R. Casas, and S. Villalba, "A Review of Distributed Optical Fiber Sensors for Civil Engineering Applications," *Sensors,* vol. 16, p. 748, 2016.

[22] J. F. Tressler, S. Alkoy, and R. E. Newnham, "Piezoelectric Sensors and Sensor Materials," *Journal of electroceramics,* vol. 2, pp. 257-272, 1998.

[23] W. H. Duan, Q. Wang, and S. T. Quek, "Applications of Piezoelectric Materials in Structural Health Monitoring and Repair: Selected Research Examples," *Materials,* vol. 3, pp. 5169-5194, 2010.

[24] V. Giurgiutiu, *Structural Health Monitoring: with Piezoelectric Wafer Active Sensors*: Academic Press, 2007.

[25] X. Lin and F. Yuan, "Diagnostic Lamb Waves in an Integrated Piezoelectric Sensor/Actuator Plate: Analytical and Experimental Studies," *Smart Materials and Structures,* vol. 10, p. 907, 2001.

[26] K. Ohno and M. Ohtsu, "Crack Classification in Concrete based on Acoustic Emission," *Construction and Building Materials*, vol. 24, pp. 2339-2346, 2010.

[27] L. Djeddi, R. Khelif, S. Benmedakhene, and J. Favergeon, "Reliability of Acoustic Emission as a Technique to Detect Corrosion and Stress Corrosion Cracking on Prestressing Steel Strands," *Int. J. Electrochem. Sci*, vol. 8, pp. 8356-8370, 2013.

[28] C. Liang, F. Sun, and C. Rogers, "Coupled Electro-Mechanical Analysis of Adaptive Material Systems—Determination of the Actuator Power Consumption and System Energy Transfer," *Journal of Intelligent Material Systems and Structures*, vol. 5, pp. 12-20, 1994.

[29] Z. A. Chaudhry, T. Joseph, F. P. Sun, and C. A. Rogers, "Local-Area Health Monitoring of Aircraft via Piezoelectric Actuator/Sensor Patches," in *Smart Structures & Materials' 95*, 1995, pp. 268-276.

[30] F. P. Sun, Z. Chaudhry, C. Liang, and C. Rogers, "Truss Structure Integrity Identification using PZT Sensor-Actuator," *Journal of Intelligent material systems and structures*, vol. 6, pp. 134-139, 1995.

[31] G. Park, H. H. Cudney, and D. J. Inman, "An Integrated Health Monitoring Technique using Structural Impedance Sensors," *Journal of Intelligent Material Systems and Structures*, vol. 11, pp. 448-455, 2000.

[32] V. Giurgiutiu and A. N. Zagrai, "Embedded Self-Sensing Piezoelectric Active Sensors for On-Line Structural Identification," *Journal of Vibration and Acoustics*, vol. 124, pp. 116-125, 2002.

[33] S. Bhalla, A. S. Naidu, and C. K. Soh, "Influence of Structure-Actuator Interactions and Temperature on Piezoelectric Mechatronic Signatures for NDE," in *Smart Materials, Structures, and Systems*, 2003, pp. 263-269.

[34] J. P. Broomfield, *Corrosion of Steel in Concrete: Understanding, Investigation and Repair*: CRC Press, 2002.

[35] G. H. Koch, M. P. Brongers, N. G. Thompson, Y. P. Virmani, and J. H. Payer, "Corrosion Cost and Preventive Strategies in the United States," 2002.

[36] L. Lemoine, F. Wenger, and J. Galland, "Study of the Corrosion of Concrete Reinforcement by Electrochemical Impedance Measurement," *Corrosion Rates of Steel in Concrete, ASTM STP,* vol. 1065, pp. 118-133, 1990.

[37] P. Lambert, C. Page, and P. Vassie, "Investigations of Reinforcement Corrosion. 2. Electrochemical Monitoring of Steel in Chloride-Contaminated Concrete," *Materials and Structures,* vol. 24, pp. 351-358, 1991.

[38] C. Andrade and C. Alonso, "Test Methods for On-Site Corrosion Rate Measurement of Steel Reinforcement in Concrete by Means of the Polarization Resistance Method," *Materials and Structures,* vol. 37, pp. 623-643, 2004.

[39] W. Yeih and R. Huang, "Detection of the Corrosion Damage in Reinforced Concrete Members by Ultrasonic Testing," *Cement and concrete research,* vol. 28, pp. 1071-1083, 1998.

[40] H.-W. Song and V. Saraswathy, "Corrosion Monitoring of Reinforced Concrete Structures-A," *Int. J. Electrochem. Sci,* vol. 2, pp. 1-28, 2007.

[41] D. Aggelis, E. Kordatos, D. Soulioti, and T. Matikas, "Combined Use of Thermography and Ultrasound for the Characterization of Subsurface Cracks in Concrete," *Construction and Building Materials,* vol. 24, pp. 1888-1897, 2010.

[42] K. Kobayashi and N. Banthia, "Corrosion Detection in Reinforced Concrete using Induction Heating and Infrared Thermography," *Journal of Civil Structural Health Monitoring,* vol. 1, pp. 25-35, 2011.

[43] S. Grattan, P. Basheer, S. Taylor, W. Zhao, T. Sun, and K. Grattan, "Fibre Bragg Grating Sensors for Reinforcement Corrosion Monitoring in Civil Engineering Structures," in *Journal of Physics: Conference Series*, 2007, p. 012018.

[44] X. Zhao, P. Gong, G. Qiao, J. Lu, X. Lv, and J. Ou, "Brillouin Corrosion Expansion Sensors for Steel Reinforced Concrete Structures using a Fiber Optic Coil Winding Method," *Sensors,* vol. 11, pp. 10798-10819, 2011.

[45] M. M. Andringa, D. P. Neikirk, N. P. Dickerson, and S. L. Wood, "Unpowered Wireless Corrosion Sensor for Steel Reinforced Concrete," in *Sensors, 2005 IEEE*, 2005, p. 4 pp.

[46] N. P. Dickerson, J. T. Simonen, M. M. Ardringa, S. L. Wood, and D. P. Neikirk, "Wireless Low-Cost Corrosion Sensors for Reinforced Concrete Structures," in *Smart Structures and Materials*, 2005, pp. 493-503.

[47] K. L. Bristow, "Measurement of Thermal Properties and Water Content of Unsaturated Sandy Soil using Dual-Probe Heat-Pulse Probes," *Agricultural and forest meteorology,* vol. 89, pp. 75-84, 1998.

[48] S. Krishnaiah, D. Singh, and G. Jadhav, "A Methodology for Determining Thermal Properties of Rocks," *International journal of rock mechanics and mining sciences,* vol. 41, pp. 877-882, 2004.

[49] G. Liu and B. C. Si, "Single-and Dual-Probe Heat Pulse Probe for Determining Thermal Properties of Dry Soils," *Soil Science Society of America Journal,* vol. 75, pp. 787-794, 2011.

[50] C. Chang, M. Ho, G. Song, Y.-L. Mo, and H. Li, "A Feasibility Study of Self-Heating Concrete Utilizing Carbon Nanofiber Heating Elements," *Smart Materials and Structures,* vol. 18, p. 127001, 2009.

[51] H.-M. Zhao, S.-G. Wang, Z.-M. Wu, and G.-J. Che, "Concrete Slab Installed with Carbon Fiber Heating Wire for Bridge Deck Deicing," *Journal of Transportation Engineering,* 2009.

[52] H. Zhao, Z. Wu, S. Wang, J. Zheng, and G. Che, "Concrete Pavement Deicing with Carbon Fiber Heating Wires," *Cold Regions Science and Technology,* vol. 65, pp. 413-420, 2011.

[53] Y.-J. Rao, "Recent Progress in Applications of In-Fibre Bragg Grating Sensors," *Optics and lasers in Engineering,* vol. 31, pp. 297-324, 1999.

[54] X. Zhao, W. Li, G. Song, Z. Zhu, and J. Du, "Scour Monitoring System for Subsea Pipeline based on Active Thermometry: Numerical and Experimental Studies," *Sensors*, vol. 13, pp. 1490-1509, 2013.

[55] X. Zhao, W. Li, L. Zhou, G. Song, Q. Ba, S. C. M. Ho, and J. Ou, "Application of Support Vector Machine for Pattern Classification of Active Thermometry -

based Pipeline Scour Monitoring," *Structural Control and Health Monitoring,* vol. 22, pp. 903-918, 2015.

[56] H. S. Carslaw and J. C. Jaeger, "Conduction of Heat in Solids," *Oxford: Clarendon Press, 1959, 2nd ed.,* vol. 1, 1959.

[57] D. De Vries, "A Nonstationary Method for Determining Thermal Conductivity of Soil In Situ," *Soil Science,* vol. 73, pp. 83-90, 1952.

[58] G. Kluitenberg, J. Ham, and K. L. Bristow, "Error Analysis of the Heat Pulse Method for Measuring Soil Volumetric Heat Capacity," *Soil Science Society of America Journal,* vol. 57, pp. 1444-1451, 1993.

[59] V. Leelalerkiet, J.-W. Kyung, M. Ohtsu, and M. Yokota, "Analysis of Half-Cell Potential Measurement for Corrosion of Reinforced Concrete," *Construction and Building Materials,* vol. 18, pp. 155-162, 2004.

[60] J. L. Dawson, "Electrochemical Noise Measurement: the Definitive In-Situ Technique for Corrosion Applications," *ASTM Special Technical Publication,* vol. 1277, pp. 3-35, 1996.

[61] R. Pidaparti, E. Neblett, S. Miller, and J. Alvarez, "Monitoring the Corrosion Process of Al Alloys Through Ph Induced Fluorescence," *Smart Materials and Structures,* vol. 17, p. 015001, 2008.

[62] H. Reis, B. L. Ervin, D. A. Kuchma, and J. T. Bernhard, "Estimation of Corrosion Damage in Steel Reinforced Mortar using Guided Waves," *Journal of Pressure Vessel Technology,* vol. 127, pp. 255-261, 2005.

[63] Y. Okabe, S. Yashiro, T. Kosaka, and N. Takeda, "Detection of Transverse Cracks in CFRP Composites using Embedded Fiber Bragg Grating Sensors," *Smart Materials and Structures,* vol. 9, p. 832, 2000.

[64] H. Tsutsui, A. Kawamata, T. Sanda, and N. Takeda, "Detection of Impact Damage of Stiffened Composite Panels using Embedded Small-Diameter Optical Fibers," *Smart Materials and structures,* vol. 13, p. 1284, 2004.

[65] K. Peters, "Polymer Optical Fiber Sensors—A Review," *Smart materials and structures*, vol. 20, p. 013002, 2010.

[66] M. Prabhugoud and K. Peters, "Efficient Simulation of Bragg Grating Sensors for Implementation to Damage Identification in Composites," *Smart materials and structures*, vol. 12, p. 914, 2003.

[67] C. Wang, "Fiber Loop Ringdown—A Time-Domain Sensing Technique for Multi-Function Fiber Optic Sensor Platforms: Current Status and Design Perspectives," *Sensors,* vol. 9, pp. 7595-7621, 2009.

[68] T. Wei, Y. Han, Y. Li, H.-L. Tsai, and H. Xiao, "Temperature-Insensitive Miniaturized Fiber Inline Fabry-Perot Interferometer for Highly Sensitive Refractive Index Measurement," *Optics Express,* vol. 16, pp. 5764-5769, 2008.

[69] B B. Qi, G. R. Pickrell, P. Zhang, Y. Duan, W. Peng, J. Xu, Z. Huang, J. Deng, H. Xiao, Z. Wang, and W. Huo, "Fiber Optic Pressure and Temperature Sensors for Oil Down Hole Application," in *Environmental and Industrial Sensing*, 2002, pp. 182-190.

[70] C. Wang and C. Herath, "High-Sensitivity Fiber-Loop Ringdown Evanescent-Field Index Sensors using Single-Mode Fiber," *Optics letters*, vol. 35, pp. 1629-1631, 2010.

[71] P. S. Rutherford, R. Ikegami, J. E. Shrader, D. Sherrer, N. Zabaronick, J. S. Zeakes, K. A. Murphy, and R. O. Claus, "Novel NDE Fiber Optic Corrosion Sensor," in *1996 Symposium on Smart Structures and Materials*, 1996, pp. 158-169.

[72] W. Hu, H. Cai, M. Yang, X. Tong, C. Zhou, and W. Chen, "Fe–C-Coated Fibre Bragg Grating Sensor for Steel Corrosion Monitoring," *Corrosion Science*, vol. 53, pp. 1933-1938, 2011.

[73] Y. Chen, F. Tang, Y. Bao, Y. Tang, and G. Chen, "A Fe-C Coated Long-Period Fiber Grating Sensor for Corrosion-Induced Mass Loss Measurement," *Optics letters*, vol. 41, pp. 2306-2309, 2016.

[74] J. R. Epstein and D. R. Walt, "Fluorescence-based Fibre Optic Arrays: A Universal Platform for Sensing," *Chemical Society Reviews*, vol. 32, pp. 203-214, 2003.

[75] A. A. Panova, P. Pantano, and D. R. Walt, "In Situ Fluorescence Imaging of Localized Corrosion with a Ph-Sensitive Imaging Fiber," *Analytical chemistry*, vol. 69, pp. 1635-1641, 1997.

[76] R. Kostecki, H. Ebendorff-Heidepriem, C. Davis, G. McAdam, T. Wang, and T. M. Monro, "Fiber Optic Approach for Detecting Corrosion," in *SPIE Smart*

Structures and Materials+ Nondestructive Evaluation and Health Monitoring, 2016, pp. 98031I-98031I-14.

[77] K. Habib and F. Al-Sabti, "Monitoring Pitting Corrosion by Holographic Interferometry," *Corrosion*, vol. 53, pp. 688-692, 1997.

[78] D. Mayorga-Cruz, P. Márquez-Aguilar, O. Sarmiento-Martinez, and J. Uruchurtu-Chavarín, "Evaluation of Corrosion in Electrochemical Systems using Michelson Interferometry," *Optics and lasers in engineering*, vol. 45, pp. 140-144, 2007.

[79] M. E. Jones, J. A. Greene, V. Bhatia, T. D'Alberto, G. A. Ten Eyck, P. M. Schindler, K. A. Murphy, and R. O. Claus, "Optical Fiber Grating-based Strain and Corrosion Sensors," in *Nondestructive Evaluation Techniques for Aging Infrastructure and Manufacturing*, 1996, pp. 94-100.

[80] Z. Zheng, X. Sun, and Y. Lei, "Monitoring Corrosion of Reinforcement in Concrete Structures via Fiber Bragg Grating Sensors," *Frontiers of Mechanical Engineering in China*, vol. 4, pp. 316-319, 2009.

[81] M. R. A. Hassan, M. H. A. Bakar, K. Dambul, and F. R. M. Adikan, "Optical-based Sensors for Monitoring Corrosion of Reinforcement Rebar via an Etched Cladding Bragg Grating," *Sensors*, vol. 12, pp. 15820-15826, 2012.

[82] C. J. Pacheco and A. C. Bruno, "A Noncontact Force Sensor based on a Fiber Bragg Grating and Its Application For Corrosion Measurement," *Sensors*, vol. 13, pp. 11476-11489, 2013.

[83] C. Tan, Y. Shee, B. Yap, and F. M. Adikan, "Fiber Bragg Grating based Sensing System: Early Corrosion Detection for Structural Health Monitoring," *Sensors and Actuators A: Physical*, vol. 246, pp. 123-128, 2016.

[84] Y. Sun, B. Shi, S. Chen, H. Zhu, D. Zhang, and Y. Lu, "Feasibility Study on Corrosion Monitoring of a Concrete Column with Central Rebar using BOTDR," *Smart Struct. Syst*, vol. 13, pp. 41-53, 2014.

[85] Y. Chunhe, J. Xiaobo, Y. Xin, and Z. Chao, "A New Type Optical Fiber Sensor for Measuring Liquid Level," in *Measurement, Information and Control (MIC), 2012 International Conference on*, 2012, pp. 55-58.

[86] T. Poczęsny, K. Prokopczuk, P. Makowski, and A. Domański, "Optical Fiber Macro-Bend Seismic Sensor for Real-Time Vibration Monitoring in Harsh Industrial Environment," in *SPIE Optical Metrology*, 2011, pp. 80823L-80823L-6.

[87] A. T. Moraleda, C. V. García, J. Z. Zaballa, and J. Arrue, "A Temperature Sensor based on a Polymer Optical Fiber Macro-Bend," *Sensors*, vol. 13, pp. 13076-13089, 2013.

[88] K. V. Madhav, Y. Semenova, and G. Farrell, "Macro-Bend Optical Fiber Linear Displacement Sensor," in *SPIE Photonics Europe*, 2010, pp. 772608-772608-6.

[89] I. S. Colombo, I. Main, and M. Forde, "Assessing Damage of Reinforced Concrete Beam using "B-Value" Analysis of Acoustic Emission Signals," *Journal of materials in civil engineering*, vol. 15, pp. 280-286, 2003.

[90] M. E. Zitto, R. Piotrkowski, A. Gallego, F. Sagasta, and A. Benavent-Climent, "Damage Assessed by Wavelet Scale Bands and B-Value in Dynamical Tests of a

Reinforced Concrete Slab Monitored with Acoustic Emission," *Mechanical Systems and Signal Processing,* vol. 60, pp. 75-89, 2015.

[91] L. Qin, Y. Lu, and Z. Li, "Embedded Cement-based Piezoelectric Sensors for Acoustic Emission Detection in Concrete," *Journal of Materials in Civil Engineering,* vol. 22, pp. 1323-1327, 2010.

[92] Y. Lu, Z. Li, and W.-I. Liao, "Damage Monitoring of Reinforced Concrete Frames under Seismic Loading using Cement-based Piezoelectric Sensor," *Materials and structures,* vol. 44, pp. 1273-1285, 2011.

[93] L. Qin, H.-W. Ren, B.-Q. Dong, and F. Xing, "Acoustic Emission Behavior of Early Age Concrete Monitored by Embedded Sensors," *Materials,* vol. 7, pp. 6908-6918, 2014.

[94] H. Gu, G. Song, H. Dhonde, Y. Mo, and S. Yan, "Concrete Early-Age Strength Monitoring using Embedded Piezoelectric Transducers," *Smart materials and structures,* vol. 15, p. 1837, 2006.

[95] G. Song, H. Gu, and Y.-L. Mo, "Smart Aggregates: Multi-Functional Sensors for Concrete Structures—A Tutorial and a Review," *Smart Materials and Structures,* vol. 17, p. 033001, 2008.

[96] Q. Kong, S. Hou, Q. Ji, Y. Mo, and G. Song, "Very Early Age Concrete Hydration Characterization Monitoring using Piezoceramic based Smart Aggregates," *Smart Materials and Structures,* vol. 22, p. 085025, 2013.

[97] Y. Moslehy, H. Gu, A. Belarbi, Y. Mo, and G. Song, "Smart Aggregate based Damage Detection of Circular RC Columns under Cyclic Combined Loading," *Smart Materials and Structures,* vol. 19, p. 065021, 2010.

[98] C. Dumoulin, G. Karaiskos, and A. Deraemaeker, "Monitoring of Crack Propagation in Reinforced Concrete Beams using Embedded Piezoelectric Transducers," *Acoustic Emission and Related Non-destructive Evaluation Techniques in the Fracture Mechanics of Concrete: Fundamentals and Applications,* p. 161, 2015.

[99] A. E976, "Standard Guide for Determining the Reproducibility of Acoustic Emission Sensor Response," 2005.

[100] A. Farhidzadeh, S. Salamone, B. Luna, and A. Whittaker, "Acoustic Emission Monitoring of a Reinforced Concrete Shear Wall by B-Value based Outlier Analysis," *Structural Health Monitoring,* p. 1475921712461162, 2012.

[101] L. Golaski, P. Gebski, and K. Ono, "Diagnostics of Reinforced Concrete Bridges by Acoustic Emission," *Journal of acoustic emission,* vol. 20, pp. 83-89, 2002.

[102] P. Ziehl and A. Pollock, *Acoustic Emission for Civil Structures*: INTECH Open Access Publisher, 2012.

[103] J. Geng, Q. Sun, W. Zhang, and C. Lü, "Effect of High Temperature on Mechanical and Acoustic Emission Properties of Calcareous-Aggregate Concrete," *Applied Thermal Engineering,* vol. 106, pp. 1200-1208, 2016.

[104] W. H. Soong, J. Raghavan, and S. H. Rizkalla, "Fundamental Mechanisms of Bonding of Glass Fiber Reinforced Polymer Reinforcement to Concrete," *Construction and building Materials,* vol. 25, pp. 2813-2821, 2011.

[105] J. F. Davalos, P. Qiao, X. F. Xu, J. Robinson, and K. E. Barth, "Modeling and Characterization of Fiber-Reinforced Plastic Honeycomb Sandwich Panels for Highway Bridge Applications," *Composite structures,* vol. 52, pp. 441-452, 2001.

[106] X. Qing, Z. Wu, F.-K. Chang, K. Ghosh, V. Karbhari, and C. Sikorsky, "Monitoring the Disbond of Externally Bonded CFRP Composite Strips for Rehabilitation of Bridges," in *Proceedings of the Third European Workshop on SHM, Structural Health Monitoring,* 2006, pp. 463-470.

[107] H. Li, G. Xian, Q. Lin, and H. Zhang, "Freeze – Thaw Resistance of Unidirectional - Fiber - Reinforced Epoxy Composites," *Journal of Applied Polymer Science,* vol. 123, pp. 3781-3788, 2012.

[108] T. Kanakubo, K. Yonemaru, H. Fukuyama, M. Fujisawa, and Y. Sonobe, "Bond Performance of Concrete Members Reinforced with FRP Bars," *ACI Special Publications,* vol. 138, pp. 767-767, 1993.

[109] D. G. Aggelis, "Classification of Cracking Mode in Concrete by Acoustic Emission Parameters," *Mechanics Research Communications,* vol. 38, pp. 153-157, 2011.

[110] L. Calabrese, G. Campanella, and E. Proverbio, "Identification of Corrosion Mechanisms by Univariate and Multivariate Statistical Analysis during Long

Term Acoustic Emission Monitoring on a Pre-Stressed Concrete Beam," *Corrosion Science*, vol. 73, pp. 161-171, 2013.

[111] A. Mpalaskas, I. Vasilakos, T. Matikas, H. Chai, and D. Aggelis, "Monitoring of the Fracture Mechanisms Induced by Pull-Out and Compression in Concrete," *Engineering Fracture Mechanics*, vol. 128, pp. 219-230, 2014.

[112] J. P. McCrory, S. K. Al-Jumaili, D. Crivelli, M. R. Pearson, M. J. Eaton, C. A. Featherston, M. Guagliano, K. M. Holford, and R. Pullin, "Damage Classification in Carbon Fibre Composites using Acoustic Emission: A Comparison of Three Techniques," *Composites Part B: Engineering*, vol. 68, pp. 424-430, 2015.

[113] S. K. Al-Jumaili, K. M. Holford, M. J. Eaton, J. P. McCrory, M. R. Pearson, and R. Pullin, "Classification of Acoustic Emission Data from Buckling Test of Carbon Fibre Panel using Unsupervised Clustering Techniques," *Structural Health Monitoring,* vol. 14, pp. 241-251, 2015.

[114] A. Behnia, H. K. Chai, and T. Shiotani, "Advanced Structural Health Monitoring of Concrete Structures with the Aid of Acoustic Emission," *Construction and building materials*, vol. 65, pp. 282-302, 2014.

[115] Y. Kawasaki, S. Wasada, T. Okamoto, and K. Izuno, "Evaluation for RC Specimen Damaged from Rebar Corrosion by Acoustic Emission Technique," *Construction and Building Materials,* vol. 67, pp. 157-164, 2014.

[116] A. Gallego, A. Benavent-Climent, and E. Suarez, "Concrete-Galvanized Steel Pull-Out Bond Assessed by Acoustic Emission," *Journal of Materials in Civil Engineering,* vol. 28, p. 04015109, 2015.

[117] M. Baena, L. Torres, A. Turon, and C. Barris, "Experimental Study of Bond Behaviour between Concrete and FRP Bars using a Pull-Out Test," *Composites Part B: Engineering,* vol. 40, pp. 784-797, 2009.

[118] E. N. Landis, "Micro–Macro Fracture Relationships and Acoustic Emissions in Concrete," *Construction and Building Materials,* vol. 13, pp. 65-72, 1999.

[119] P. J. De Groot, P. A. Wijnen, and R. B. Janssen, "Real-Time Frequency Determination of Acoustic Emission for Different Fracture Mechanisms in Carbon/Epoxy Composites," *Composites Science and Technology,* vol. 55, pp. 405-412, 1995.

[120] R. Gutkin, C. Green, S. Vangrattanachai, S. Pinho, P. Robinson, and P. Curtis, "On Acoustic Emission for Failure Investigation in CFRP: Pattern Recognition and Peak Frequency Analyses," *Mechanical Systems and Signal Processing,* vol. 25, pp. 1393-1407, 2011.

[121] C. Ramirez-Jimenez, N. Papadakis, N. Reynolds, T. Gan, P. Purnell, and M. Pharaoh, "Identification of Failure Modes in Glass/Polypropylene Composites by Means of the Primary Frequency Content of the Acoustic Emission Event," *Composites Science and Technology,* vol. 64, pp. 1819-1827, 2004.

[122] L. Dahmani, A. Khennane, and S. Kaci, "Crack Identification in Reinforced Concrete Beams using ANSYS Software," *Strength of materials,* vol. 42, pp. 232-240, 2010.

[123] X. Chang, G. Yue, H. Lin, and C. Tang, "Modeling the Pullout Behavior of Fiber Reinforced Polymer Bars from Concrete," *Construction and Building Materials,* vol. 24, pp. 431-437, 2010.

[124] E. Hognestad, "Study of Combined Bending and Axial Load in Reinforced Concrete Members," *University of Illinois. Engineering Experiment Station. Bulletin; no. 399,* 1951.

[125] J. Larralde and R. Silva-Rodriguez, "Bond and Slip of FRP Rebars in Concrete," *Journal of Materials in Civil Engineering,* vol. 5, pp. 30-40, 1993.

[126] H. Wang, "An Analytical Study of Bond Strength Associated with Splitting of Concrete Cover," *Engineering Structures,* vol. 31, pp. 968-975, 2009.

[127] B. Ghiassi, E. Verstrynge, P. B. Lourenço, and D. V. Oliveira, "Characterization of Debonding in FRP-Strengthened Masonry using the Acoustic Emission Technique," *Engineering Structures,* vol. 66, pp. 24-34, 2014.

[128] S. D. Kim, C. W. In, K. E. Cronin, H. Sohn, and K. Harries, "Reference-Free NDT Technique for Debonding Detection in CFRP-Strengthened RC Structures," *Journal of Structural Engineering,* vol. 133, pp. 1080-1091, 2007.

[129] K. K. Ghosh and V. M. Karbhari, "Use of Infrared Thermography for Quantitative Non-Destructive Evaluation in FRP Strengthened Bridge Systems," *Materials and structures,* vol. 44, pp. 169-185, 2011.

[130] G. Jiang, M. Dawood, K. Peters, and S. Rizkalla, "Global and Local Fiber Optic Sensors for Health Monitoring of Civil Engineering Infrastructure Retrofit with FRP Materials," *Structural Health Monitoring,* vol. 9, pp. 309-322, 2010.

[131] R. Perera, E. Sevillano, A. Arteaga, and A. De Diego, "Identification of Intermediate Debonding Damage in FRP-Plated RC Beams based on Multi-Objective Particle Swarm Optimization without Updated Baseline Model," *Composites Part B: Engineering*, vol. 62, pp. 205-217, 2014.

[132] J. Ou and H. Li, "Structural Health Monitoring in Mainland China: Review and Future Trends," *Structural Health Monitoring*, vol. 9, pp. 219-231, 2010.

[133] Z. Wu, X. P. Qing, K. Ghosh, V. Karbhar, and F.-K. Chang, "Health Monitoring of Bonded Composite Repair in Bridge Rehabilitation," *Smart Materials and Structures*, vol. 17, p. 045014, 2008.

[134] G. Park, H. H. Cudney, and D. J. Inman, "Feasibility of using Impedance‐based Damage Assessment for Pipeline Structures," *Earthquake engineering & structural dynamics*, vol. 30, pp. 1463-1474, 2001.

[135] G. Park, H. Sohn, C. R. Farrar, and D. J. Inman, "Overview of Piezoelectric Impedance-based Health Monitoring and Path Forward," 2003.

[136] S. Park, S. Ahmad, C.-B. Yun, and Y. Roh, "Multiple Crack Detection of Concrete Structures using Impedance-based Structural Health Monitoring Techniques," *Experimental Mechanics*, vol. 46, pp. 609-618, 2006.

[137] S. Park, J.-J. Lee, C.-B. Yun, and D. J. Inman, "Electro-Mechanical Impedance-based Wireless Structural Health Monitoring using PCA-Data Compression and K-Means Clustering Algorithms," *Journal of intelligent material systems and structures*, 2007.

[138] S. Na and H. Lee, "Resonant Frequency Range Utilized Electro-Mechanical Impedance Method for Damage Detection Performance Enhancement on Composite Structures," *Composite Structures,* vol. 94, pp. 2383-2389, 2012.

[139] Y. Y. Lim and C. K. Soh, "Electro-Mechanical Impedance (EMI)-based Incipient Crack Monitoring and Critical Crack Identification of Beam Structures," *Research in Nondestructive Evaluation,* vol. 25, pp. 82-98, 2014.

[140] A. Narayanan and K. V. Subramaniam, "Experimental Evaluation of Load-Induced Damage in Concrete from Distributed Microcracks to Localized Cracking on Electro-Mechanical Impedance Response of Bonded PZT," *Construction and Building Materials,* vol. 105, pp. 536-544, 2016.

[141] S. W. Shin and T. K. Oh, "Application of Electro-Mechanical Impedance Sensing Technique for Online Monitoring of Strength Development in Concrete using Smart PZT Patches," *Construction and Building Materials,* vol. 23, pp. 1185-1188, 2009.

[142] R. Tawie and H. Lee, "Monitoring the Strength Development in Concrete by EMI Sensing Technique," *Construction and Building Materials,* vol. 24, pp. 1746-1753, 2010.

[143] D. Wang and H. Zhu, "Monitoring of the Strength Gain of Concrete using Embedded PZT Impedance Transducer," *Construction and Building Materials,* vol. 25, pp. 3703-3708, 2011.

[144] G. Boemio, P. Rizzo, and L. De Nardo, "Assessment of Dental Implant Stability by Means of the Electromechanical Impedance Method," *Smart Materials and Structures,* vol. 20, p. 045008, 2011.

[145] A. Tabrizi, P. Rizzo, and M. W. Ochs, "Electromechanical Impedance Method to Assess Dental Implant Stability," *Smart Materials and Structures,* vol. 21, p. 115022, 2012.

[146] V. Talakokula, S. Bhalla, and A. Gupta, "Corrosion Assessment of Reinforced Concrete Structures based on Equivalent Structural Parameters using Electro-Mechanical Impedance Technique," *Journal of Intelligent Material Systems and Structures,* p. 1045389X13498317, 2013.

[147] R. Dugnani, Y. Zhuang, F. Kopsaftopoulos, and F.-K. Chang, "Adhesive Bond-Line Degradation Detection via a Cross-Correlation Electromechanical Impedance–based Approach," *Structural Health Monitoring,* p. 1475921716655498, 2016.

[148] S. Park, J.-W. Kim, C. Lee, and S.-K. Park, "Impedance-based Wireless Debonding Condition Monitoring of CFRP Laminated Concrete Structures," *NDT & E International,* vol. 44, pp. 232-238, 2011.

[149] Y. Liang, D. Li, S. M. Parvasi, Q. Kong, and G. Song, "Bond-Slip Detection of Concrete-Encased Composite Structure using Electro-Mechanical Impedance Technique," *Smart Materials and Structures,* vol. 25, p. 095003, 2016.

[150] C. Liang, F. Sun, and C. Rogers, "An Impedance Method for Dynamic Analysis of Active Material Systems," *Journal of Vibration and Acoustics*, vol. 116, pp. 120-128, 1994.

[151] W. S. Na and K.-T. Park, "A Cost-Effective Impedance-based Structural Health Monitoring Technique for Steel Structures by Monitoring Multiple Areas," *Journal of Intelligent Material Systems and Structures,* p. 1045389X16645866, 2016.

[152] S. Park, C. B. YUN, and D. Inman, "Structural Health Monitoring using Electro‐Mechanical Impedance Sensors," *Fatigue & Fracture of Engineering Materials & Structures,* vol. 31, pp. 714-724, 2008.

[153] J.-T. Kim, K.-D. Nguyen, and J.-H. Park, "Wireless Impedance Sensor Node and Interface Washer for Damage Monitoring in Structural Connections," *Advances in Structural Engineering,* vol. 15, pp. 871-885, 2012.

[154] Y. Yang, Y. Y. Lim, and C. K. Soh, "Practical Issues Related to the Application of the Electromechanical Impedance Technique in the Structural Health Monitoring of Civil Structures: I. Experiment," *Smart Materials and Structures,* vol. 17, p. 035008, 2008.

[155] V. G. M. Annamdas and Y. Yang, "Practical Implementation of Piezo‐Impedance Sensors in Monitoring of Excavation Support Structures," *Structural Control and Health Monitoring,* vol. 19, pp. 231-245, 2012.

[156] F. Guo, Z. Yu, P. Liu, and Z. Shan, "Practical Issues Related to the Application of Electromechanical Impedance-based Method in Concrete Structural Health Monitoring," *Research in Nondestructive Evaluation,* vol. 27, pp. 26-33, 2016.